

**SCANNING MECHANISMS FOR
INTRAVASCULAR ULTRASOUND IMAGING:
a flexible approach**

Harm ten Hoff



Printing and binding: Universiteitsdrukkerij Erasmus Universiteit Rotterdam

CIP-DATA KONINKLIJKE BIBLIOTHEEK, DEN HAAG

Hoff, Harm ten

Scanning mechanisms for intravascular ultrasound imaging:
a flexible approach / H. ten Hoff. - [S.l. : s.n.]. - Ill.

Thesis Rotterdam. - With ref.

ISBN 90-9006072-3

NUGI 743

Subject headings: intravascular ultrasound imaging /
catheters.

Copyright © 1993 by H. ten Hoff, Rotterdam, The Netherlands

**SCANNING MECHANISMS FOR INTRAVASCULAR
ULTRASOUND IMAGING:
a flexible approach**

Scanning mechanismen voor intravasculaire afbeeldingstechnieken:
een flexibele benadering

PROEFSCHRIFT

TER VERKRIJGING VAN DE GRAAD VAN DOCTOR

AAN DE ERASMUS UNIVERSITEIT ROTTERDAM

OP GEZAG VAN DE RECTOR MAGNIFICUS
PROF. DR. C.J. RIJNVOS

EN VOLGENS BESLUIT VAN HET COLLEGE VAN DEKANEN.

DE OPENBARE VERDEDIGING ZAL PLAATSVINDEN
OP DINSDAG 22 JUNI 1993 om 13.45 UUR

DOOR

HARM TEN HOFF

GEBOREN TE BORGER

PROMOTIECOMMISSIE

Promotor: Prof. Dr. Ir. N. Bom (Erasmus Universiteit Rotterdam)

Promotor: Prof. Dr. Ir. C.J. Snijders (Erasmus Universiteit Rotterdam)

Overige leden:

Prof. Dr. Ir. P. Meijers (Delft University of Technology)

Prof. Dr. Ir. H.F. van Beek (Delft University of Technology)

Financial support by the Netherlands Heart Foundation (NHS) and the Technology Foundation of the Netherlands (STW) for the publication of this thesis is gratefully acknowledged.

Contents

	page
Preface	VII
Introduction	IX
CHAPTER 1. Intravascular ultrasound imaging; a medical introduction	1
- Introduction	1
- Atherosclerosis	2
- Diagnosis of atherosclerosis	4
- Treatment of obstructive vascular disease	5
- New diagnostic tools	8
CHAPTER 2. Intravascular ultrasound imaging; a technological introduction	15
§ 2.1 Basic theory of ultrasound imaging	15
§ 2.2 Ultrasonics in intravascular imaging	21
§ 2.3 Catheter technology	28
§ 2.4 The intravascular US-imaging system	32
CHAPTER 3. Mechanical scanning in intravascular ultrasound imaging	37
§ 3.1 Image artifacts due to non-ideal catheter-tip motion	37
§ 3.2 Principles of catheter-tip rotation	44
§ 3.2.1 Basic principles	44
§ 3.2.2 Working methods of catheter-tip rotation	46
CHAPTER 4. Flexible drive-shaft rotation transmission	61
- Symbols	62
§ 4.1 Analytical modelling	65
§ 4.2 Finite element modelling	89
§ 4.3 Experimental results	105
§ 4.4 Conclusions; flex-shaft specifications	114
CHAPTER 5. Correction for non-uniform catheter-tip rotation	117
§ 5.1 Indications for application	117
§ 5.2 Methods	118
§ 5.2.1 Reduction of rotary speed in the catheter-tip	118
§ 5.2.2 Angle detection systems	119
§ 5.3 High resolution optical angle detection system;	
a first design approach	122
§ 5.3.1 System requirements	122
§ 5.3.2 Design structure	124
§ 5.3.3 System design and development	125
§ 5.3.4 Discussion, conclusions and recommendations	141

CHAPTER 6. Conclusions and recommendations	147
--------------------------------------------	-----

APPENDICES

A. String pulley driving mechanism	151
B. Effect of $EI_y \neq EI_z$ and pre-curvature on the rotation transmission characteristics of a flexible drive-shaft; analytical modelling	155
C. Effect of friction on the rotation transmission characteristics of a flexible drive-shaft; analytical modelling	165
D. Effect of $EI_y \neq EI_z$ and pre-curvature, combined with friction, on the rotation transmission characteristics of a flexible drive-shaft; analytical modelling	171
E. Finite element model description.	175
F. Measurement methods for determination of flexible drive-shaft properties	183
G. Basic theory on optical fibers as dielectric waveguides	191
H. Production methods of code-disks	195
I. Calculation of electrical signal transmission lines.	199
Summary	207
Samenvatting	213
Acknowledgements	219
Curriculum Vitae	223
Publications of the author	225

Preface

Since the early seventies, the research-group of Experimental Echocardiography of the Thoraxcentre in Rotterdam has developed various types of ultrasound (US) transducers and imaging systems, involving the clinic, where they should find their application, as well as industries, where they should be produced in order to eventually find their way to common clinical use.

It was in the same manner that in 1987 the development of an intravascular US-imaging catheter started, partly based on previous work, performed in the early seventies on the development of an intracardiac probe. The official work started beginning 1988 as a project funded by the Technology Foundation of the Netherlands (STW). However, several research groups, especially in the US, also started developing comparable systems. Soon it became clear that intravascular ultrasound would become "a hot issue" and that if we wanted to compete in developing an eventually commercial system, we would need more technological and financial support.

As a solution to enable us to accept this challenge a unique construction was found. A project-plan was drawn-up, with the goal to develop an intravascular US-imaging system, to be commercially available in four years. For the commercialization of the system the company Du-MED B.V. was founded. In this partnership, Du-MED participated financially and the university got contributions from the university hospital (AZR), the Technology Foundation of the Netherlands (STW) and the Interuniversity Cardiology Institute of the Netherlands (ICIN).

On top of this, the Ministry of Economic Affairs (EZ) granted us a large subsidy, so that it became possible to involve several institutions and companies, to contribute their specialized knowledge.

Not without pride we can say that an intravascular US-imaging system is now available commercially, suitable for coronary as well as peripheral application. The clinical validation of this new diagnostic method is now getting well under way.

In the course of the project, beginning 1991, when the company Du-MED B.V. had started to take over large parts of the product development and engineering, I found more time for the basic research accounted for in this thesis.

Introduction

This thesis deals with the technology of intravascular ultrasound (US) imaging systems, and in particular with systems applying mechanical scanning. In these systems an ultrasonic beam, originating from a catheter-tip, is rotated by mechanical means, in order to produce an ultrasonic scan of the surrounding of the catheter-tip. Being positioned in a blood-vessel, a cross-sectional echo-image of the vessel can be displayed, showing e.g. an obstruction.

The realization and successful application of an intravascular US imaging system is an outstanding example of a multi-disciplinary development, involving basic physical and technological knowledge on e.g. acoustics, mechanics, electronics and image-processing as well as understanding of the medical background and clinical application. Practical skills and experience on micro-mechanic prototyping are mandatory, as is knowledge on specific properties of medical disposables, concerning blood-compatibility of materials, cleaning and sterilization methods.

The multidisciplinary character of the project called for a joint effort of a large number of research institutions and companies, supervised by the research and development group of Experimental Echocardiography of the Erasmus University Rotterdam.

The writer of this thesis has managed the development as the project-leader in the years 1988 to 1991, establishing and maintaining contacts between participating institutions and companies and reporting on progress and financial issues to subsidizing organizations.

Not all technological problems arisen and solutions found during the course of the development of the intravascular US imaging system can be described and motivated in this thesis. An overview of medical perspectives (Chapter 1) and relevant technologies (Chapter 2) is given with an emphasis on adequate mechanical intravascular scanning (Chapter 3) and in particular a study is presented of the application of flexible drive-shaft rotation transmission in order to establish mechanical ultrasonic scanning in the catheter-tip (Chapter 4). Finally the development effort of the implementation of an optical rotation angle detection system is described (Chapter 5).

Chapter 1 discusses the medical aim of intravascular US-imaging. It shows possible applications and some preliminary results of the clinical evaluation, performed at the department of Radiology and the Angio-lab of the Thoraxcentre, both at the University Hospital Dijkzigt in Rotterdam. Furthermore this chapter introduces some clinical system requirements.

Chapter 2 deals with the general technological aspects of intravascular US-imaging. Ultrasonics, scanning methods and catheter technology are briefly discussed. A global comparison between electronical and mechanical scanning is made, establishing the choice in favour of mechanical scanning. The complete system configuration is introduced, consisting of a catheter, a driving unit and a main-frame console.

The division of Acoustics of the Delft University of Technology developed and produced the miniature 30 MHz ultrasonic transducers. Catheter-tubes, either regular or specialty, were purchased from Cordis, Roden. The main-frame electronics and software control has been developed in cooperation with Bakker Electronics, Dongen.

Chapter 3 contains a description of image artifacts due to catheter-tip motion and non-ideal scan-rotation. Some requirements to the scan-rotation are defined.

Several methods of mechanical US-beam rotation are presented and briefly evaluated, based on an investigation, conducted in cooperation with the Laboratory for Precision Engineering of the Delft University of Technology, Faculty of Mechanical Engineering and Marine Technology.

A flexible drive-shaft can transmit a rotary motion from a proximal motor through the catheter-tube to the distal tip. A double-layer spiral-type flex-shaft has promising qualities and its development has been successfully pursued. Development and prototyping of these flex-shafts have been performed by the writer of this thesis in cooperation with the catheter-firm USCI at their production facilities in Billerica, MA, USA.

As a future alternative the development of an electromagnetic micro-motor, which can be built into the catheter-tip, has started and already showed promising results.

Chapter 4 contains the analytical modelling of the rotation transmission behaviour of a flexible drive-shaft, with defined over-all characteristics, running through a curved (catheter) tube. Calculation results of this model are compared with numerical simulations, based on the finite element method. This theoretical work has been supported by the Laboratory for Engineering Mechanics of the Delft University of Technology, Faculty of Mechanical Engineering and Marine Technology.

A dedicated measurement set-up to test the rotation transmission behaviour is described as it is operational at Du-MED B.V., Rotterdam. The measurement results are again compared with results, obtained from the analytical modelling.

In *Chapter 5*, an optical rotation angle detection system is proposed in order to monitor the actual rotary motion of the ultrasonic beam at the catheter-tip. This additional information can be used to adequately display a cross-sectional image of the blood-vessel. However, for the present this development has been abandoned, because of its technological complexity and therefore doubtful economic perspectives as a product for one-time-use only. Implementation of such a system may be considered in the future if the

driving mechanism, now considered to be adequate, would lose its angular fidelity, because of different operating circumstances.

Knowledge on optics and fiber-optics was brought in by the Institute of Applied Physics (TPD) of the Netherlands Organization for Applied Scientific Research (TNO), Delft and Coenecoop B.V., Waddinxveen. Micro-code-disks were produced by Applied Image, Inc., Rochester, NY, USA and the Delft University of Technology. A specially designed drive-shaft containing two electrical leads and an optical fiber could be produced at De Regt Optical Cable B.V., Capelle a/d IJssel.

Catheter and driving-unit design were made in cooperation with the Productcentre TNO, Delft. Here also the prototyping took place under "clean-room" conditions.

Finally in *Chapter 6* the conclusions of this thesis are presented, together with recommendations for further research.

The writer of this thesis was involved in all the major choices and decisions and directly conducted or supervised research on the choice of sonolucent dome-material, patient-safe fluid-filling of the catheter, mechanical safety of the catheter material and glue-joints and system design implications of bed-side ergonomics. At the time of the first series of clinical trials, the writer of this thesis acted as the liaison between the physicians, the catheter development group and the catheter prototype production. He managed the logistics, coordinating production, fluid-filling, cleaning, packaging and sterilization, prior to clinical usage.

Furthermore he was involved with the choice of micro-mechanical driving mechanisms to rotate the ultrasonic beam in the catheter-tip and the characterization of adequate rotary motion with respect to image reliability (Chapter 3).

He supervised the early development and catheter-prototyping, implementing an optical rotation angle detection system in order to monitor the actual rotation of the US-transducer in the catheter-tip, in which case reliable imaging would be achieved also (Chapter 5).

The writer of this thesis developed theory on the characterization of flexible drive-shaft rotation transmission through the curved catheter-tube, revealing the important design properties of a flexible drive-shaft for this application (Chapter 4). He also succeeded in the design and prototyping of double layer spiral-type flexible drive-shafts, suitable even for reliable imaging of coronary arteries. Finally he transferred his knowledge and experience to industry, where he helped to build production facilities for these shafts, that are now operational.

CHAPTER 1 Intravascular ultrasound imaging; a medical introduction

Introduction

The ultrasound (US) imaging technique has been known for some decades now as a patient-friendly diagnostic tool. The non-invasive character of the technique, as well as the use of harmless ultrasonic radiation, has stimulated its wide-spread application, for instance in cardiology, radiology and gynaecology.

The extracorporeal application of US diagnostics, although one of the advantages of the technique, has several fundamental limitations. The region of interest may be shielded by natural barriers for US energy, allowing for only a specific "window" to be used for imaging. Air-filled organs, ribs, bones and tissue layers with a high collagen content are such natural barriers.

Furthermore structures, located deeper in the body can only be imaged with relatively poor resolution. This is due to the fact that for higher image resolution higher US frequencies are required, exhibiting a more than proportional increase of attenuation of US energy and therefore a reduction of the penetration depth (see Chapter 2: Fig. 2.1-3).

These practical limitations have incited the development of more invasive US probes for specific medical diagnostic applications, such as the transesophageal probe for scanning the heart, the transrectal and transurethral probes for investigation of e.g. the prostate and intravascular US imaging for diagnosis of obstructions in coronary and peripheral arteries and guidance of catheter-based interventional methods [1].

This chapter deals with the purpose of intravascular ultrasound imaging. While clinical evaluation is in progress, some reasoning may show to be speculative. Nevertheless it will be made clear that the contemporary techniques, available to the clinician to deal with blood-vessel obstructive disease (atherosclerosis), are not completely satisfactory. Also it will be made plausible that intravascular ultrasound imaging can contribute to the solution of some of the problems of today's practice.

For a better understanding some elementary information is provided on the anatomy of the normal artery, the pathogenesis of atherosclerosis and the morphology of blood-vessel obstructions.

Atherosclerosis

Blood-vessel obstructions are caused by atherosclerosis and may result in the loss of vital functions. Atherosclerosis is known to be the most important cause of death in the western world.

The normal artery

A healthy artery generally consists of three distinct concentric layers, separated by two elastic membranes (Fig. 1-1) [2]. The most inner layer, the intima, consists of a monolayer of endothelium cells resting on a thin sub-endothelium layer. The endothelium provides for a blood-compatible interface with the blood-stream, so that no blood-reaction, varying from blood-platelet adhesion to coagulation will occur. The middle layer, separated from the intima by the internal elastic membrane, is called the media. The most outer layer, the adventitia forms the interface to the surrounding tissue and for larger vessels is vascularized to supply nutrients and oxygen to the vessel-wall itself.

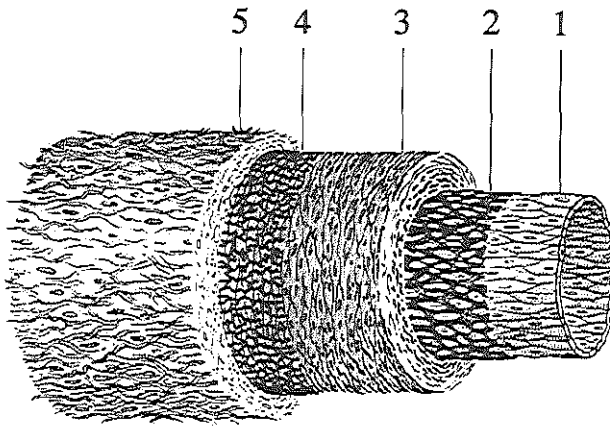


Fig. 1-1 The three layers of a normal artery [2]. Intima (1), internal elastic membrane (2), media (3), external elastic membrane (4), adventitia (5).

Based on the characteristics of the arterial media, two types of arteries can be distinguished: the elastic and muscular arteries. The media of the elastic type of artery contains many elastic fibers, suited to withstand the high blood-pressure peaks close to the heart. The aorta, carotid artery and main coronary branches are elastic arteries. The media of the muscular type of arteries consists mainly of smooth muscle cells and hardly any elastic fibers. The more distal coronaries and iliofemoral arteries belong to the muscular type.

Pathogenesis of atherosclerosis

The pathogenesis of atherosclerosis is not yet fully understood. A model of simple deposition of fatty material clearly is not adequate, regarding the different and complex morphologies of the atherosclerotic lesions, that may consist of any combination of fatty substances, collagen, calcium, different cell types and thrombi.

Many atherogenetic hypotheses have been proposed by different investigators [3]. These theories are not necessarily contradicting, but can be regarded each to describe one small part of a large puzzle. Some theories describe the biochemical reactions to some chemical agents, like nicotine and cholesterol [4]. Others emphasize the effects of hemodynamic factors, which determine the shear stress on the vessel wall, but also affect the role of blood cells in the process [5]. These theories are backed up by the fact that the atherosclerotic plaques don't usually appear diffusely divided in the whole arterial system, but are clearly localized at specific spots, where the blood-stream is "disturbed" by a side-branch, bifurcation or severe curvature (Fig. 1-2) [9]. The theoretical findings are connected with the proved risk-factors like smoking, high blood-pressure, wrong dietary habits, stress and lack of exercise [6].

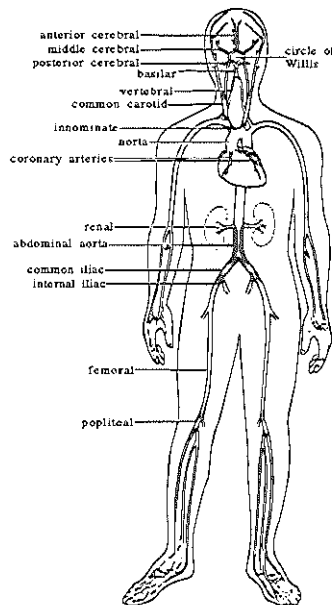


Fig. 1-2 Localized atherosclerotic plaques [9]⁽¹⁾.

⁽¹⁾From "Atherosclerosis", by David M. Spain. Copyright © (1966) by Scientific American, Inc. All rights reserved.

The most widely adapted hypothesis can briefly be characterized by: "response to injury" [7, 8]. In this view the atherosclerotic lesion is caused by a "normal" or maybe "exaggerated" repair reaction after repeated damage to the inner endothelium lining of the blood-vessel, by chemical or mechanical factors.

Morphology of the atherosclerotic plaque

The single "classical" atherosclerotic plaque is a process mostly involving the intima and gradually, when it is growing, it can extend into the media (Fig. 1-3: left). The atheroma, a fatty substance of cholesterol and cell debris, is encapsulated by a fibrous collagen layer on which the monolayer of endothelium has been restored [10]. Migration of smooth muscle cells from the media towards the intima and the presence of calcium crystals can be observed. The ongoing process of damage and repair over many years may lead to a complex lesion, which will eventually close off (most of) the vessel lumen (Fig. 1-3: right).

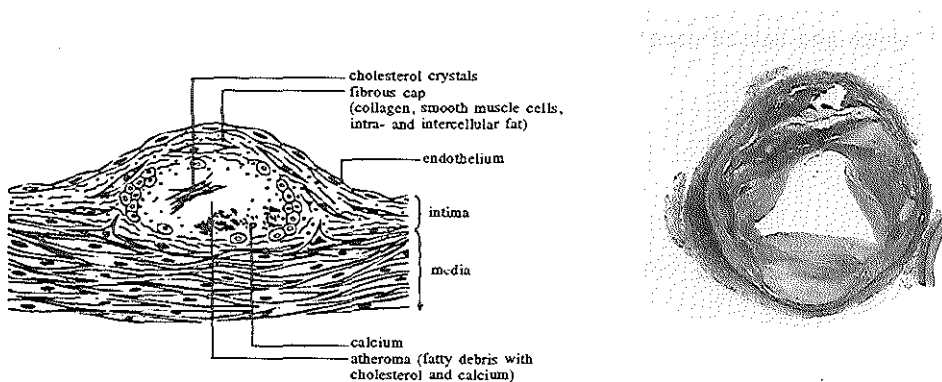


Fig. 1-3 "Classical" atherosclerotic plaque (left) [10] and complex lesion (right)(photo: by courtesy of E.J. Gussenhoven).

Diagnosis of atherosclerosis

Currently diagnosis of vessel obstructions is performed by angiography, which is X-ray imaging of the vessels after injection of a contrast agent through a catheter (Fig. 1-4 and Fig. 1-12). The angiogram provides a silhouette of the lumen of the blood-vessel of interest and its branchings from the position of contrast injection towards down-stream. A stenosis usually can be seen as a restriction of the lumen. Angiography is a powerful and efficient technique to localize blood-vessel obstructions and also allows for an estimation of the degree of narrowing (rate of stenosis), where densitometry (analysis of the image blackening) can help to obtain some information about the third (hidden) dimension [11].

However, the projection information of the angiogram is dependent on the choice of direction of the X-ray beam, which plays an important roll in revealing a clear sight of the blood-vessel narrowing (Fig. 1-4).

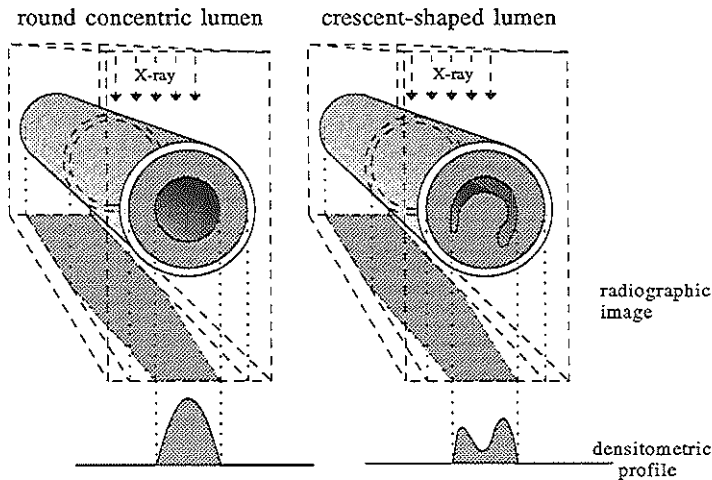


Fig. 1-4 Angiography is a projection technique, which may not reveal the (true rate of) stenosis.

Even by bi-plane angiography not enough information can be obtained to exactly reconstruct the 3-dimensional geometry of the blood-vessel lumen. And apparently, by the nature of the technique, hardly any information can be obtained about the state of the blood-vessel wall and the type of the obstructing substances.

Treatment of obstructive vascular disease

The classical recanalization therapy is the quite radical by-pass operation, still being performed as a final solution. A shunt is placed over the obstructed site, for which preferably an artery from the patient's own body is used, or if needed an artificial polymer based blood vessel prosthesis can be applied (Fig. 1-5).

Nowadays, however, less invasive deobstruction methods are applied, based on catheter technology often referred to as interventional techniques. On a large scale balloon dilatation (Dotter) procedures are performed to open up obstructed coronary arteries as well as peripheral vessels. Inflation of a balloon at the tip of a catheter, positioned in the narrowed area, will stretch the vessel-wall, resulting in a larger lumen (Fig. 1-6) [12].

Evidently this method can only be used when a small free lumen still exists to let the balloon catheter pass through the lesion. In case of a total occlusion other techniques are required.

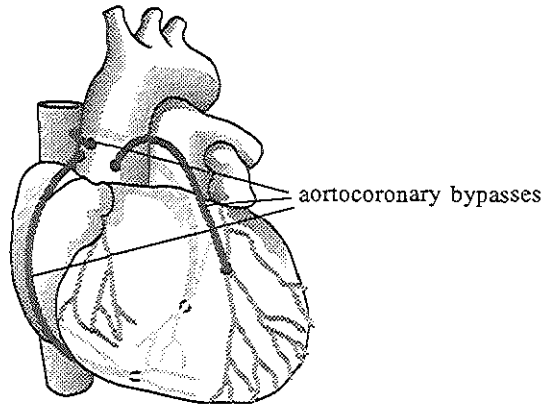


Fig. 1-5 Aortocoronary by-pass.

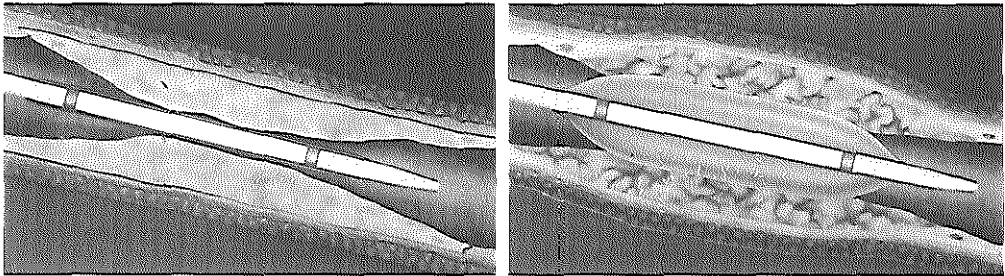


Fig. 1-6 Balloon dilation [13].

For the long term, balloon dilation has a limited success-rate. In 30 to 40% of the cases re-stenosis will occur within 6 months [14]. This may be due to the damage done to the obstructing structures as well as the vessel wall and the fact that the obstructing materials are not removed by this procedure, only remodelled.

For this reason other catheter-based techniques are under investigation, some of which already are used in a clinical setting:

- Laser-ablation is a method delivering laser-light at the stenotic site through an optical fiber, to evaporate the obstructing material, either by directly shining onto it (Fig. 1-7a) or by heating up a metal tip as an intermediate (hot tip) (Fig. 1-7b) [15].
- Atherectomy is a technique that cuts away pieces of the stenosis. The stenotic material is kept in the catheter and that way removed (Fig. 1-7c) [16].
- The Kensey catheter is equipped with a fast rotating (100.000 rpm) abrasive tip, which grinds away the stenosis, aiming to produce only very small particles to get into the blood-stream (Fig. 1-7d) [17].
- Ultrasound angioplasty aims to ablate blood-vessel obstructions by high energy, low frequency (20 kHz) ultrasound, delivered by catheter technology (Fig. 1-7e) [18].
- The spark-erosion technique aims to evaporate the obstruction by small electrical sparks, generated between an electrode on a catheter-tip and the obstructive material (Fig. 1-7f) [19].

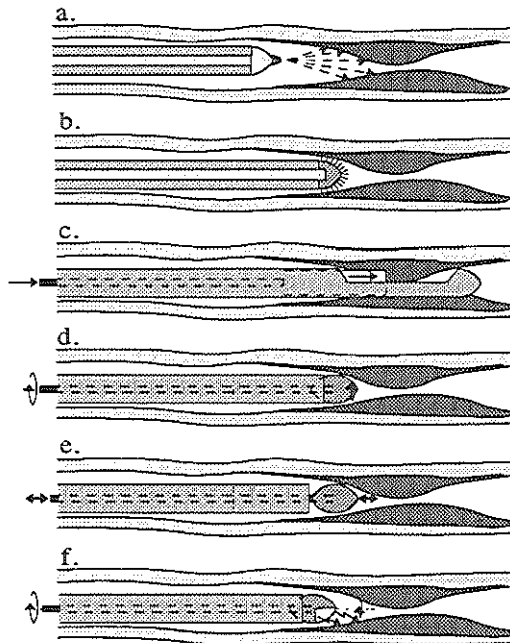


Fig. 1-7 New interventional techniques under (clinical) investigation.

Laser-ablation, direct light (a), Hot-tip (b), Atherectomy (c), Kensey (d), Ultrasound angioplasty (e), Spark-erosion (f).

These methods, however, have not (yet) shown a significant reduction of the occurrence of re-stenosis. This may again be due to the damage they do, the degree of which cannot be determined adequately, using only angiography [20].

The physician also needs specific information about the geometry of the stenosis and its containing substances. This information can reveal counter-indications for some of the interventional methods to choose from. E.g. balloon dilatation of an eccentric lesion may lead to arterial wall rupture, due to overstretching. The presence of calcium in the obstruction can diminish the effectiveness of laser ablation. Again angiography will not give this information.

The new interventional techniques bear the risk of perforating the blood-vessel wall, because of non-selective cutting or evaporation of the stenotic material as well as the blood-vessel wall. Especially in curved vessels an adequate catheter-tip guiding system is needed to keep the catheter close to the centre of the blood-vessel. At the moment only angiography is used for that, but as has been explained earlier, this method does not reliably show the actual three-dimensional situation and perforation cannot be ruled out [21].

New diagnostic tools

The successful clinical application of the interventional techniques as described above would greatly be served by a new high-resolution imaging technique, which supplies the necessary 3-dimensional geometrical information of the stenotic site and if possible also determines its containing material components.

Two new diagnostic techniques, also catheter-based, have been developed for this purpose in the past few years: angioscopy and intravascular ultrasound imaging. The first is a forward-viewing device, imaging the inside of blood-vessels, based on optical fiber technology [22]. Drawbacks of this system are the necessity for extensive flushing with a transparent medium to clear the viewing field and the fact that information is obtained only from the inside surface and not from underlying tissue structures (Fig. 1-8).

The second, intravascular US imaging, yields two-dimensional cross-sectional images of the blood vessel surrounding the catheter-tip [23]. By the nature of ultrasonic imaging these images show, besides the cross-sectional geometry of the vessel-lumen, also tissue structures under the surface of the vessel inner wall to a certain penetration depth. This opens possibilities to tissue differentiation and determination of the obstructing materials.

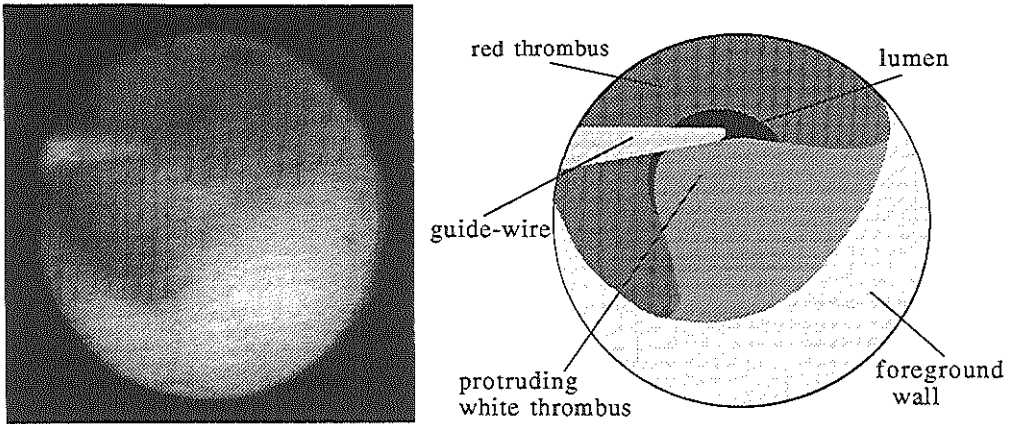


Fig. 1-8 Angioscopic image of a stenotic coronary artery showing thrombi (left), with explanation (right) (by courtesy of P.J. de Feyter).

Interesting is the fact that for muscular arteries the three-layer anatomy of the artery can be visualized by this technique (Fig. 1-9). The lack of US-reflecting fibres in the media causes it to appear as a less echo-dense layer in the image. The internal elastic membrane, however, appears very clearly with high echo-density, so that the intima in which the process of atherosclerosis mainly is situated, is sharply defined by the image. This allows for accurate determination of the extent of the atherosclerotic plaque with respect to the open lumen [24, 25, 26]. Unfortunately this analysis is more difficult for elastic arteries, where the media predominantly exists of elastin fibers and appears as bright as its surrounding tissue (Fig. 1-10) [23].

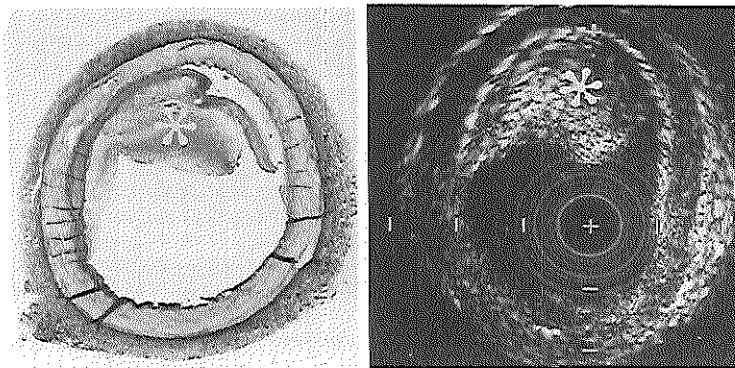


Fig. 1-9 Cross-sectional ultrasound image (right) and corresponding anatomy (left) of a muscular femoral artery, obtained in vitro, showing an eccentric obstructive atherosclerotic lesion () [23].*

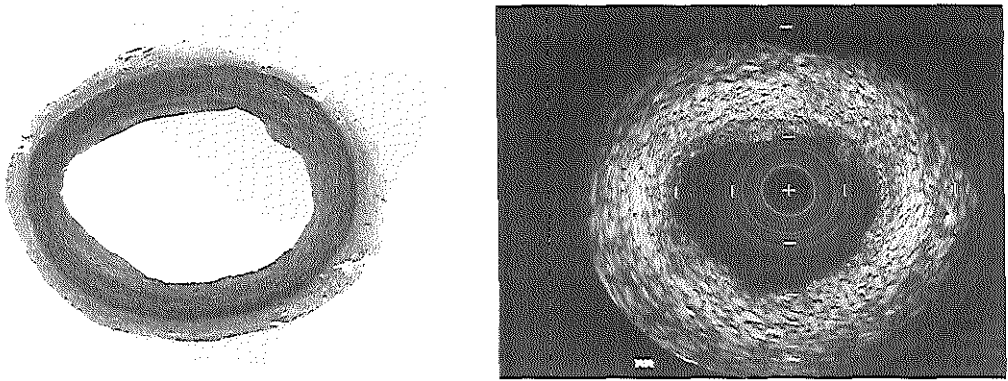


Fig. 1-10 Cross-sectional ultrasound image of an elastic carotid artery, obtained in vitro (right), and corresponding histology (left)(photo: by courtesy of E.J. Gussenhoven).

Fig. 1-11 shows a cross-section of an obstructed femoral artery in which different material components of the stenosis can be recognized. The most obvious is calcium, because it blocks the ultrasound energy entirely, causing shadowing.

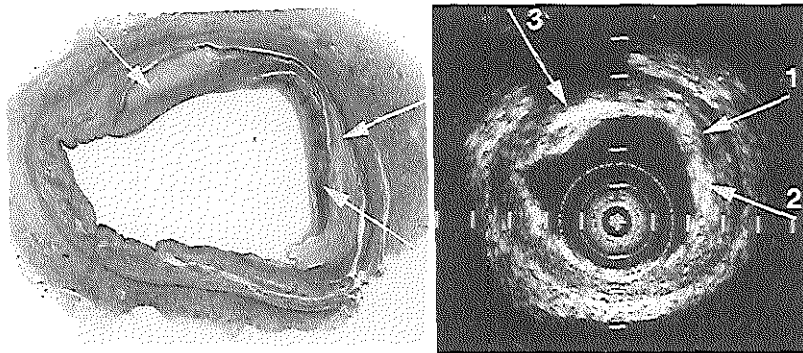


Fig. 1-11 Cross-sectional ultrasound image of a femoral artery, obtained in vitro (right), showing a classical obstructive atherosclerotic lesion, with corresponding histology (left). Fatty debris appearing as hypoechoic (arrow 1), collagen as bright echoes (arrow 2) and calcium as bright echoes with shadowing (arrow 3), are the major plaque constituents. Magnification 8× [23].

The monitoring and evaluation of a therapeutic intervention procedure by a combination of angiography and intravascular US-imaging renders interesting results [27, 28]. Fig. 1-12 shows a superficial femoral artery, seen before and after balloon dilation, in an angiographic image as well as by cross-sectional echography at two levels of the artery. The angiographic recording shows no sign of obstructive disease at the proximal level (24), whereas intravascular echography shows the presence of diffuse intima thickening. The remaining lumen, however, is large enough. At the stenotic site (level 27), angiography shows an obstructed lumen. At this level the echographic image shows that the lumen is just large enough to accommodate the catheter.

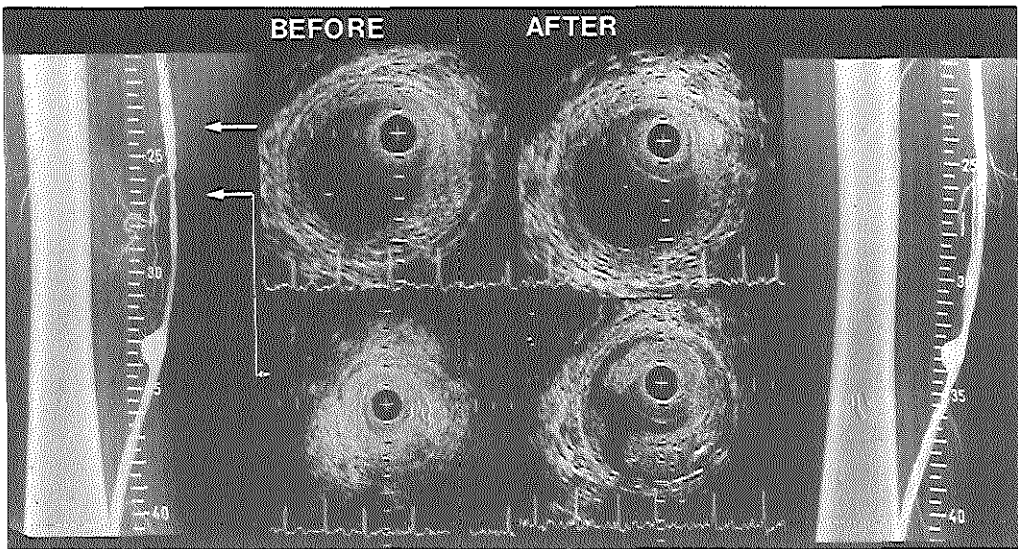


Fig. 1-12 Cross-sectional echo-images of the femoral artery in vivo in combination with angiography, at different levels in the artery, before and after balloon dilation (photo: by courtesy of E.J. Gussenhoven).

After balloon dilation not much has changed at level 24. At the obstructed site, angiography shows widening of the lumen. In addition a dissection is evident. Similar observations can be made from the ultrasound image. It shows an irregular lumen cross-section and the lesion has been partially dissected from the vessel-wall. The increase of the lumen cross-section is mostly due to overstretching of the vessel-wall and is not so much caused by reduction of the volume of the obstructive material [28, 29].

Generally, a more optimistic estimation of the rate of stenosis is made based on angiography, than is derived from ultrasonic cross-sectional images.

In order to make interactive use of the imaging information during an interventional procedure, hybrid systems have been developed, incorporating US imaging and a therapeutic method in one catheter. Experimental catheters already have been built and tested, combining US imaging with balloon dilatation, laser ablation or atherectomy [21].

Three-dimensional computer reconstruction of a blood vessel is possible by processing a sequence of two-dimensional cross-sectional images, recorded along the central axis of the blood-vessel [30] (Fig 1-13).

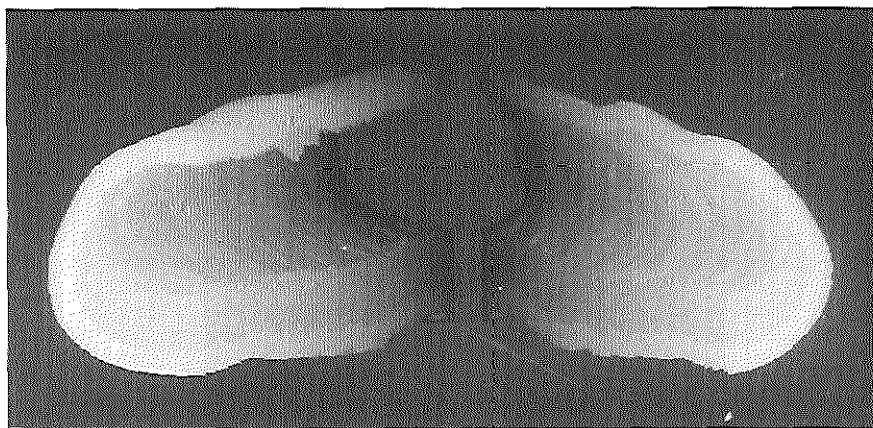


Fig. 1-13 A cut-open display of a coronary artery, using 3D reconstruction [31].

References

1. Bom N., Hoff H. ten, Lancée C.T., Gussenhoven W.J., Bosch J.G., Early and recent intraluminal ultrasound devices, *Int. J. Cardiac Imag.* 4: 79-88, 1989.
2. Kahle W., Leonhardt H., Platzer W., eds., *Atlas der anatomie*, Dutch edition: *Sesam atlas van de anatomie*, Bosch en Keuning NV, Baarn, p. 33, 1986.
3. Reitsma K., Hoff H. ten, Heethaar R.M., Aken W.G. van, *Ontstaanshypothesen van atherosclerose, pathofysiologische en hemodynamische invloeden*, Literature research, University Twente, The Netherlands in cooperation with Deps. of Medical Physics and Hematology, State University of Utrecht, The Netherlands, June 18, 1987.
4. Benditt E.P., The origin of atherosclerosis, *Scientific American*, 236: 74-85, 1977.
5. Nerem R.M., Arterial fluid and interactions with the vessel wall, In: *Structure and Function of the Circulation*, 2: 719-835, 1981.
6. Grundy S.M., *Atherosclerosis: Pathology, Pathogenesis and role of Risk Factors*, D.M. 29: 1-58, 1983.

7. Ross R., Glomset J.A., The Pathogenesis of Atherosclerosis (first), *The New England J. of Medicine*, 295: 369-377, 1976.
8. Ross R., The Pathogenesis of Atherosclerosis - an Update, *The New England J. of Medicine*, 314: 488-500, 1986.
9. Spain D.M., Atherosclerosis, *Scientific American*, 215: 48-56, 1966.
10. Becker A.E., Atherosclerose - een dynamisch morfologische beschouwing, In: *Atherosclerose en Hypertensie*, pp. 1-26, 1985.
11. Whiting J.S., Pfaff J.M., Eigler N.L., Advantages and limitations of videodensitometry in quantitative coronary angiography, In: *Quantitative coronary arteriography*, Reiber J.H.C., Serruys P.W., eds., Kluwer Academic Publishers, Dordrecht, Boston, London, pp. 43-54, 1991.
12. Dotter C.T., Judkins M.P., Transluminal treatment of arteriosclerotic obstruction: description of a new technique and a preliminary report of its application. *Circulation* 30: 654-670, 1964.
13. Bayer, Coronary stenosis and occlusions - therapeutic alternatives, 1986.
14. Liu M.W., Roubin G.S., King S.B.III, Restenosis after coronary angioplasty, *Circulation* 79: 1374-1387, 1989.
15. Verdaasdonk R.M., Laser angioplasty with modified fiber tips, Ph.D thesis of the State University of Utrecht, The Netherlands, 1990.
16. Simpson J.B., Selmon M.R., Robertson G.C., Cipriano P.R., Hayden W.G., Johnson D.E., Fogarty T.J., Transluminal atherectomy for occlusive peripheral vascular disease, *Am. J. Cardiol.* 61: 96G-101G, 1988.
17. Kensey K., Nash J.E., Abrahams C., Zarins C.K., Recanalization of obstructed arteries with a flexible, rotating tip catheter. *Radiology* 165: 387-389, 1987.
18. Siegel R.J., Crew J.R., Dean M., Ariani M., Cumberland D.C., Tissue ablation with catheter-delivered ultrasound, In: *Intravascular ultrasound imaging*, Tobis J.M., Yock P.G., eds., Churchill Livingstone, New York, pp. 123-131, 1992.
19. Slager C.J., Bom N., Serruys P.W., Schuurbiers J.C.H., Vandenbroucke W.V.A., Lancée C.T., Spark erosion and its combination with sensing devices for ablation of vascular lesions, In: *Interventional cardiology: future directions*, Vogel J.H.K., King S.B., eds., The C.V. Mosby Company, St. Louis, pp. 157-169, 1989.
20. Tobis J.M., Mahon D.J., Moriuchi M., Honye J., McRae M., Intravascular ultrasound imaging following balloon angioplasty, *Int. J. Cardiac Imag.* 6: 191-205, 1991.
21. Crowley R.J., Hamm M.A., Joshi S.H., Lennox C.D., Roberts G.T., Ultrasound guided therapeutic catheters: recent developments and clinical results, *Int. J. Cardiac Imag.* 6: 145-156, 1991.
22. White C.J., Ramee S.R., Percutaneous coronary angioscopy, In: *Intravascular ultrasound imaging*, Tobis J.M., Yock P.G., eds., Churchill Livingstone, New York, Edinburgh, London, Melbourne, Tokyo, pp. 113-121, 1992.
23. Gussenhoven W.J., Essed C.E., Frietman P., Mastik F., Lancée C.T., Slager C., Serruys P., Gerritsen P., Pieterman H., Bom N., Intravascular echographic assessment of vessel wall characteristics: a correlation with histology, *Int. J. Cardiac Imag.* 4: 105-116, 1989.

24. Li W., Gussenhoven W.J., Zhong Y., The S.H.K., Di Mario C., Madretsma S., Egmond F. van, Feyter P. de, Urk H. van, Rijsterborgh H., Bom N., Validation of quantitative analysis of intravascular ultrasound images, *Int. J. Cardiac Imag.* 6: 247-253, 1991.
25. Gussenhoven E.J., Essed C.E., Lancée C.T., Mastik F., Frietman P., Egmond F.C. van, Reiber J., Bosch H., Urk H. van, Roelandt J., Bom N., Arterial wall characteristics determined by intravascular imaging: an in vitro study, *J. Am. Coll. Cardiol.* 14: 947-952, 1989.
26. Gussenhoven W.J., Frietman P.A.V., The S.H.K., Suylen R.J. van, Egmond F.C. van, Lancée C.T., Urk H. van, Roelandt J.R.T.C., Stijnen T., Bom N., Assessment of medial thinning in atherosclerosis by intravascular ultrasound, *Am. J. Cardiol.* 68: 1625-1632, 1991.
27. Gussenhoven W.J., The S.H.K., Gerritsen P., Urk H. van., Li W., Egmond F.C. van, Roelandt J.R.T.C., Lancée C.T., Bom N., Real-time intravascular ultrasonic imaging before and after balloon angioplasty, *J. Clin. Ultrasound* 19: 294-297, 1991.
28. The S.H.K., Gussenhoven E.J., Zong Y., Li W., Egmond F. van, Pieterman H., Urk H. van, Gerritsen G.P., Borst C., Wilson R.A., Bom N., Effect of balloon angioplasty on femoral artery evaluated with intravascular ultrasound imaging, *Circulation* 86: 483-493, 1992.
29. Urk H. van, Gussenhoven W.J., Gerritsen G.P., Pieterman H., The S.H.K., Egmond F. van, Lancée C.T., Bom N., Assessment of arterial disease and arterial reconstructions by intravascular ultrasound, *Int. J. Cardiac Imag.* 6: 157-164, 1991.
30. Kitney R.I., Moura L., Straughan K., 3-D visualization of arterial structures using ultrasound and Voxel modelling, *Int. J. Cardiac Imag.* 4: 135-143, 1989.
31. Li W., Bosch J.G., Zhong Y., The S.H.K., Gussenhoven W.J., Mastik F., Egmond F. van, Rijsterborgh H., Reiber J.H.C., Bom N., Image segmentation and 3D reconstruction of intravascular ultrasound images, *Abstracts of 20th International Symposium on Acoustical Imaging*, Nanjing, China, September 12-14, 1992, p. 85.

CHAPTER 2 Intravascular ultrasound imaging; a technological introduction

Introduction

In this chapter an introduction to the technology of intravascular US imaging is presented. The system comprises high frequency US imaging technology, partly built into a small diameter catheter, allowing US-probe delivery to the region of interest. Paragraph 2.1 deals with some basic theory of US imaging in general, after which in § 2.2 the ultrasonics of specifically the intravascular application will be discussed, showing two different concepts of system design (circular phased array and mechanical scanning). In § 2.3 general aspects of vascular catheterization and catheter technology will be introduced to set specifications for the US-probe. And in § 2.4 an introduction is given to a complete intravascular US imaging system, as it is used in the clinical setting.

§ 2.1 Basic theory of ultrasound imaging

The theory of ultrasonic imaging in medical applications is documented in [1], [2] and [3]. A short summary is presented here.

US-wave generation and principles of scanning

Excitation of a piezo-electric transducer by an electronic pulse creates an ultrasonic wave, the wavelength of which is determined by the fundamental frequency of the transducer and the velocity of sound in the present medium. The pulse-wave can be as short as several wave-lengths if the transducer has adequate damping. While travelling through the adjacent tissue, the US wave scatters or reflects on small particles and boundaries, where a change of the acoustic impedance of the material occurs (Fig. 2.1-1a). Part of the scattered and reflected acoustic energy comes back onto the transducer and forms the echo-signal. The distance between the transducer and the reflecting structure is known from the sound velocity in the present medium and the time-interval between emission of the pulse-wave and reception of the echo. The echo-signal can be visualized as a function of time on an oscilloscope, representing the so-called A-mode signal [4]. Either the echo amplitude or the echo intensity, translated into a grey-scale level, can be displayed this way. In the latter case the vertical dimension on the oscilloscope screen can be used for a time registration of the A-mode signal, by adding a slow vertical sweep of the electron beam. The motion

of US-reflecting structures can be monitored this way. It is called the Time-Motion display or M-mode signal. The A-mode and M-mode signals represent information obtained along a single sound beam.

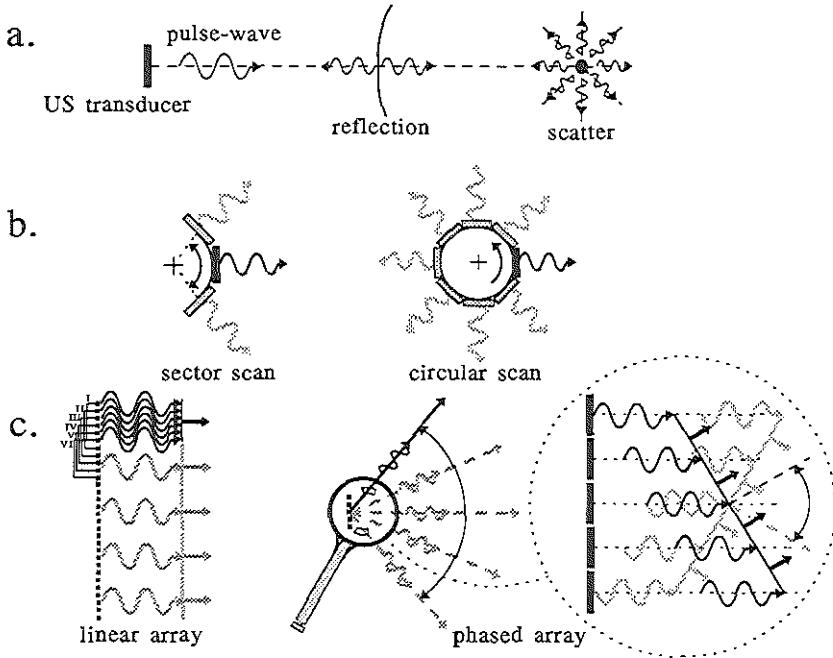


Fig. 2.1-1 The basics of ultrasonic imaging. Pulse-wave generation, reflection and scattering (a); Two-dimensional image by mechanical scanning: sector and circular scan (b); Two-dimensional image by linear array or the electronic scan of phased array (c).

A two dimensional image can be obtained by moving the US transducer and thus the sound beam, while pulse-waves are being emitted and their echoes received. By rotating the transducer, echo information from different directions in a cross-sectional plane can be obtained and displayed as a polar image. The transducer can be rotated backward and forward over a certain rotation angle, resulting in a sector scan (Fig. 2.1-1b) or continuously rotated in one direction, which renders a 360° polar image.

A second way to create a two-dimensional image is by positioning more transducers in line and establishing electronically, sequential adjacent excitation of subgroups of transducer elements (linear array) (Fig. 2.1-1c). The resulting wave-front of the array of transducers can be manipulated by differentially delaying (phase shifting) the excitation pulses to the

elements. An electronical sweep of the over-all beam can be performed this way, covering a sectorial area (phased array).

Transducer frequency, resolution and penetration depth

The resolution of an ultrasound imaging system can be defined as the minimum distance between two objects, at which they are identified separately. For a US transducer three components of the resolution can be recognized: the axial resolution in the US beam direction and two lateral resolutions perpendicular to the US beam. The axial resolution AR [m] is related to the length of the pressure pulse-wave, which equals a minimum of two or three wave-lengths for a well-damped transducer, and therefore depends on the US frequency and velocity according to:

$$AR \approx 3 \frac{c}{2f} = \frac{3\lambda}{2} \quad (2-1)$$

where

c [m/s] = velocity of US waves in present medium (around 1500 m/s in blood or water),

λ [m] = wave-length.

f [Hz] = frequency

The factor 2 appears in the denominator because of the round-trip nature of the reflected wave.

The two lateral resolutions $LR_{1,2}$ [m] are given by the beam-width w , defined by the -3 dB beam contour at a specific location in two perpendicular planes, both containing the sound beam length-axis. The shape of the US beam of a single transducer depends on the shape and dimensions of the transducer, the US frequency and the presence of a focusing lens. For a round, disk-shaped transducer without a lens, functioning in pulse-mode with 3 to 4 periods per pulse, $LR_1 = LR_2 = LR$ and the -3 dB beam contour is sketched in Fig. 2.1-2 [3]. Close to the transducer ($z < z_R$) a near field can be distinguished in which an irregular US intensity pattern occurs, due to interference of US waves originating from different parts of the transducer. For $z > z_R$ the far field conditions have developed, resulting in a diverging beam with half-angle ϕ_d . A focal point can be observed at a distance z_f with a minimum beam-width of w_f .

The transition from near field to far field conditions is located around $z = z_R$, with:

$$z_R = \frac{D^2}{4\lambda} \quad (2-2)$$

The focal point is located at $z_f \approx 0.8 z_R$ and the minimum beam-width there is $w_f \approx 0.5 D$.

The diverging half-angle ϕ_d is:

$$\phi_d = \arcsin\left(\frac{0.52 \lambda}{D}\right) \quad (2-3)$$

In the far field ($z > z_R$) we can define LR as:

$$LR = w_f + 2(z - z_f)\tan\phi_d \approx w_f + \frac{1.04 (z - z_f)\lambda}{D} \quad (2-4)$$

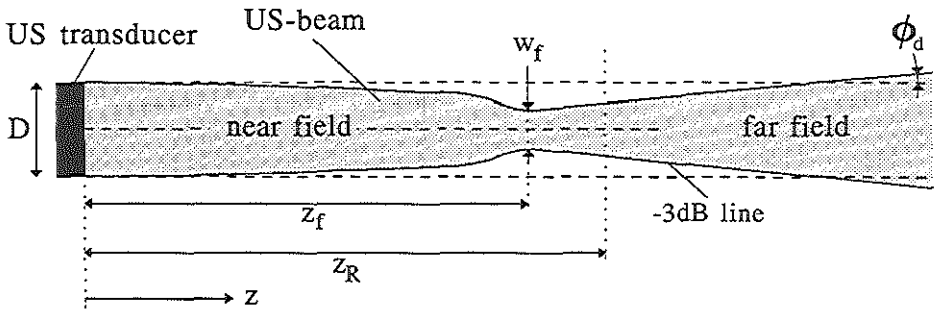


Fig. 2.1-2 US beam-shape, defined by -3 dB beam contour, of a round, disk-shaped transducer with diameter D and stimulated in pulse-mode, emitting 3 to 4 periods [3].

From eq. 2-1 it can be seen that the axial resolution improves with increasing frequency. A higher frequency also extends the near field at constant transducer diameter D or allows for a smaller diameter D at constant z_R (eq. 2-2). It also causes a decrease of the angle ϕ_d (eq. 2-3). This way also the lateral resolution is enhanced by increasing frequency.

A higher frequency, however, reduces the penetration depth of the US energy and consequently the depth of view. The absorption of acoustic energy for soft tissues is approximately proportional to the frequency and the absorption coefficient α usually lies in the range 0.5 to 3.5 dB.MHz⁻¹.cm⁻¹ (one way) [5]. A typical value of α for soft tissues is 2 dB.MHz⁻¹.cm⁻¹ (two ways) [6]. Using this figure a theoretical penetration depth of an acoustic imaging system can be calculated as a function of the acoustic frequency and the dynamic range of the system (Fig. 2.1-3). This reasoning disregards, among other things, the effects of the US beam-shape on the penetration depth.

The optimal acoustic frequency for each imaging application is found from the compromise between resolution and penetration depth.

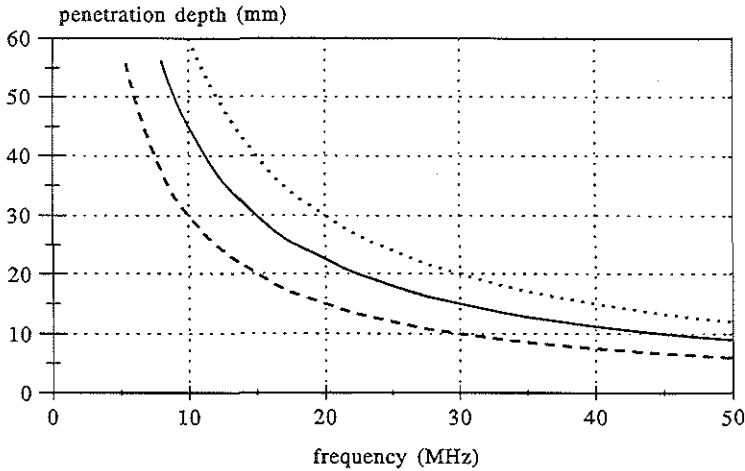


Fig. 2.1-3 Penetration depth as a function of frequency for several dynamic ranges of the imaging system: $S/N = 60$ dB (---), $S/N = 90$ dB (—) and $S/N = 120$ dB (···). Absorption coefficient α is $2 \text{ dB.MHz}^{-1}.\text{cm}^{-1}$ (two ways).

Scan speed and frame rate

The proper scan speed depends on the relative motion of the object to be imaged with respect to the transducer and the information to be obtained. In medical imaging the objects of interest are often moving and changing shape, even when the patient is at rest. Uncontrolled muscle activity, breathing and the patient's heart-beat (transmitted through all arteries) cause this motion. The motion of the objects of interest during US imaging gives rise to artifacts in the image, if the scan speed is too low. The scan speed should be chosen such that the displacement of the object is small during the time needed for one scan.

The mechanical or electronical scanning can be performed periodically, so that the image is "refreshed" with a certain frame rate. In case of continuous sector or circular scanning, the scan speed and frame rate are closely related.

Pulse rate and image resolution

The axial transducer resolution corresponds with the radial image resolution, if the image pixel-resolution is not the limiting factor. The tangential image resolution is determined by the lateral transducer resolution if, for a uniformly rotating transducer with radial

frequency ω [rad/s], the pulse rate of the transducer excitation is high enough not to skip areas of the image plane. The minimum pulse rate PR_{\min} is determined by the minimum numerical aperture NA_{\min} of the transducer as a function of the distance z . The numerical aperture NA is defined here as the sine of the maximum angle of US-wave propagation with respect to the beam axis, within the -3dB beam contour.

Considering Fig. 2.1-2, NA_{\min} is the minimum of two values: NA_1 in the focal point, which is:

$$NA_1 = \sin\{\arctan(\frac{w_f}{2z_f})\} \approx \frac{w_f}{2z_f} \quad (2-5)$$

and NA_2 in the far field, which is for small ϕ_d :

$$NA_2 = \sin\phi_d \approx \phi_d \quad (2-6)$$

PR_{\min} [Hz] is the maximum of the two values:

$$PR_1 = \frac{\omega}{2NA_1} = \frac{\omega z_f}{w_f} \quad (2-7)$$

and considering eqs. 2-6 and 2-3:

$$PR_2 = \frac{\omega}{2NA_2} = \frac{\omega}{2\phi_d} = \frac{\omega D}{1.04\lambda} \quad (2-8)$$

It seems redundant to apply a higher pulse rate, because a better image resolution than the resolution of the transducer itself cannot be obtained. This is true for echography based on US reflection, but US imaging of living tissue makes use mostly of omnidirectional US scattering by cells and small structures. The echo-signal received from a distance z is the summation of all scatter signals from particles, present in the US-beam cross-section with diameter w . This summation signal does change if, by rotation of the transducer, the cross-section is moved over a distance smaller than w , assuming that particles with other scattering characteristics will enter the US-beam. This is why there is more information to be obtained when $PR > PR_{\min}$.

§ 2.2 Ultrasonics in intravascular imaging

Scanning methods

Electronical scanning: circular phased array

A circular echo-scan of the surrounding of a catheter-tip can be made by sequential excitation of the small rectangular transducers, positioned cylindrically around a catheter-tip (Fig. 2.2-1) [4,6]. If the diameter of the catheter-tip is not too small (e.g. 3 mm, for intracardiac use) and the number of elements not too large (e.g. 32 or 64), the intensity of the US beam can be increased and the beam can be focused by activation of a subgroup of neighbouring transducers with appropriate time delay, so that it acts as one single larger US transducer (Fig. 2.2-2) [7]. A 360° circular scan is made by sequential electrical switching of adjacent subgroups.

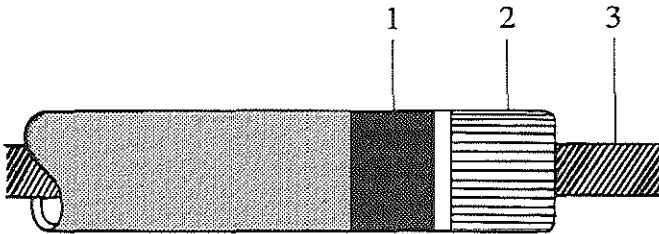


Fig. 2.2-1 Catheter-tip with circular phased array of US transducers [6].

Integrated circuitry for multiplexing (1), US-elements (2), guide-wire (3).

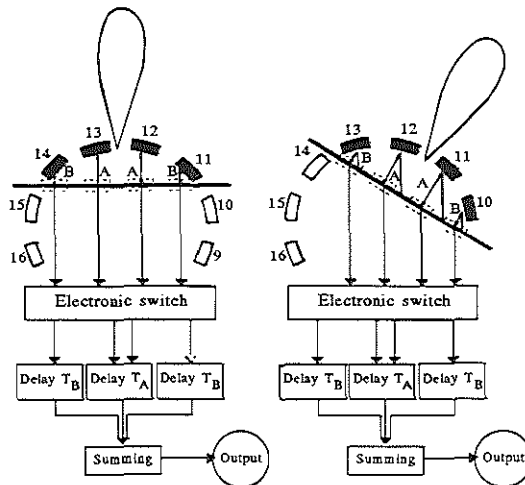


Fig. 2.2-2 The principle of phased array beam deflection by a circular array of US transducers [7].

In order to avoid image artifacts due to grating lobes, under all conditions of beam steering, theoretically the element spacing (pitch) of the array should be $< \frac{1}{4}\lambda$ [8, 9]. Practically an acceptable image quality is obtained when the pitch is chosen between $\frac{1}{4}\lambda$ and $\frac{1}{2}\lambda$. For a catheter-tip diameter of 1 mm and an acoustic frequency of 30 MHz, e.g. for coronary use, that means the application of 128 to 256 circumferential elements. The large number of elements requires built-in multiplexing electronics in the catheter-tip to avoid a bundle of conducting leads running through the catheter to the elements. The small dimensions of this catheter-tip does not allow for additional built-in electronics for phase-shifted excitation of subgroups of elements. Therefore every very small element will be activated separately, showing low sensitivity. Averaging over numerous scans will suppress the noise and enhance the image, which is reconstructed after the echo information of all elements has been collected. Especially the averaging is time-consuming, so that the frame-rate will be only several frames per second.

The large number of acoustic elements increases the complexity of the (disposable) catheter and the supporting electronics.

The echo-receiving circuitry is not sensitive to echo-signals during the pulse emission by the transducer. The amplifier will be saturated by the high energy excitation pulse and it will take some time until this pulse has been damped down below the low energy level of echo-signals. The difference is about -80 dB. This time of insensitivity represents a distance from the transducer in which reflecting structures cannot be registered. It is called the "dead zone". In case of the circular array the transducers are mounted on the surface of the cylindrical catheter-tip. The "dead zone" therefore is situated in the blood of the blood-vessel or the vessel-wall, when the catheter-tip lies against the wall (Fig. 2.2-4). In the latter case, part of the field of interest of the image is not being revealed. The "dead zone" extends a few tens of a millimetre into the adjacent medium.

The separate excitation of the high number of elements calls for either a large number of wires running through the catheter or the development of a multiplexing IC to be placed in the catheter-tip. This IC will have to be custom-made, due to the small dimensions. The circular array at the catheter-tip allows for a central lumen through the whole catheter to be kept free for guide-wire introduction purposes.

Mechanical scanning; single element US-beam rotation

A cross-sectional echo-scan of the surrounding of a catheter-tip can also be made by mechanically rotating an ultrasonic beam, generated by a single US-element. This can be achieved either by rotating a radially emitting element (Fig. 2.2-3a) or a deflecting mirror, in which case the US-transducer emits axially and is mounted statically in the catheter-tip

(Fig. 2.2-3b) or rotates together with the mirror (Fig. 2.2-3c). Transducer rotation requires rotation of its electrical leads, since slip-rings of these small catheter-tip dimensions, transmitting a pulse peak-current of several amperes, pose a problem.

The US-transducer can be optimized to allow for maximum sensitivity and image resolution. Given the available space in the catheter-tip the transducer will be designed generally as a disk-shaped round or oval, flat or slightly concave (to accomplish a focusing effect) "sandwich". A thin layer of piezo-active material (thickness = λ) is situated between an about 10λ thick backing layer, with high acoustic damping and a $\frac{1}{4}\lambda$ matching layer at the other side, to allow for efficient coupling of US energy into the adjacent medium.

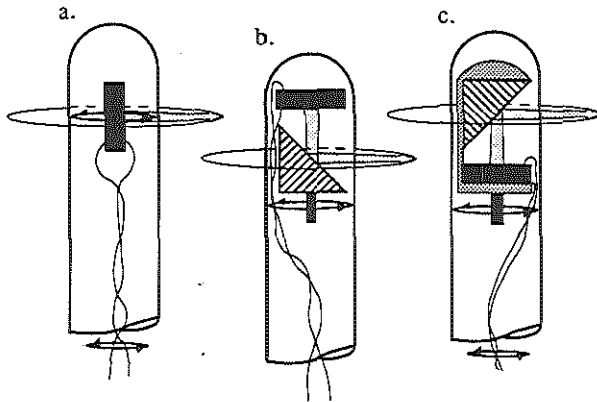


Fig. 2.2-3 Catheter-tip configurations for mechanical US-scanning: rotating transducer and leads (a), rotating deflecting mirror (b) and rotating transducer, deflecting mirror and electrical leads (c).

Mechanically rotating parts should be shielded from the patient's arterial wall, so that a sonolucent enclosing dome is required, consequently calling for the presence of a coupling fluid in the dome to transmit the US energy to and from the transducer.

The transducer supporting electronics is relatively simple and the echo-acoustic "dead-zone" can be situated in the catheter itself, so that the imaging field can start at the outer surface of the sonolucent dome (Fig. 2.2-4) [6]. The principal drawback of this system is the development of an adequate rotation mechanism to drive the catheter-tip. The requirements of this subsystem will be described in § 3.1.

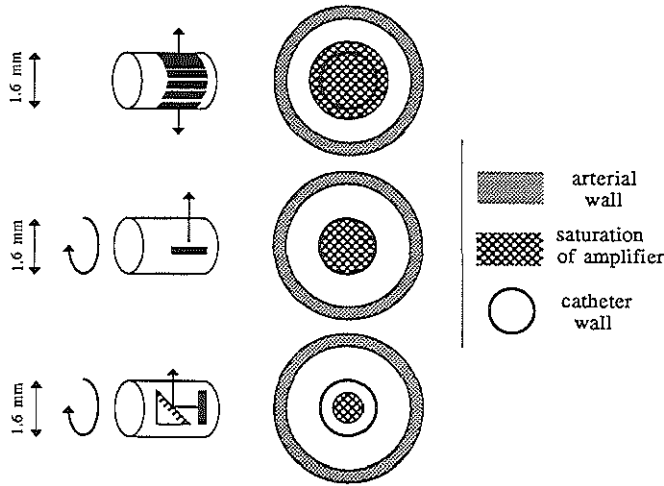


Fig. 2.2-4 Illustration of the "dead zone" as present in various systems [6].

Evaluation of scanning methods

The merits and drawbacks of both scanning systems have been summarized in Table 2.2-1. The importance of the advantages and disadvantages of both scanning systems depends on the clinical demands on the system performance. Unfortunately these demands will only be known fully, when a clinical protocol for the use of intravascular US imaging has been established and application proved to be effective. This can only be done by extensive clinical testing of the system. Prior to this stage, the choices have to be made on a somewhat speculative basis.

It is believed that the image quality is the most important system characteristic and that the mechanically scanning system is potentially better in image resolution and sensitivity. However, mechanical scanning may give rise to catheter-tip motion relative to the vessel wall and especially a non-uniform scan-motion will introduce image distortions, influencing the image reliability (see § 3.1). It is believed that by good system design these image artifacts can be limited to an acceptable, low level. Therefore in our laboratory the mechanically scanning system has been pursued.

Table 2.2-1 Comparison between electronical and mechanical intravascular US scanning.

Item	Electronical scanning	Mechanical scanning
<u>Transducer characteristics:</u>		
resolution	+/-	+
sensitivity	-	+
cross talk	-	0
simplicity	-	+
"dead zone" in field of view	-	+
<u>Scanning characteristics:</u>		
scan speed	+/-	+/-
image distortion due to non-uniform scanning	0	+/-
<u>Catheter handling:</u>		
fluid filling before use	0	-
introduction method	+	+/-
<u>Development hurdles:</u>		
sonolucent dome	0	-
catheter-tip electronics or bonding technology	-	+
main-frame electronics	-	+/-
driving mechanism	0	-
fluid filling facilities	0	-
Marking:		
- poor or negative system characteristic		
+/- moderate system characteristic		
+ good system characteristic		
0 does not apply: in all cases a positive system characteristic		

Transducer frequency, resolution and penetration depth

For the analysis of cross-sectional blood-vessel images it is important to clearly determine the lumen contour of the vessel and to distinguish between the more or less concentric anatomical layers. This requires a high radial resolution of 0.1 mm, while the tangential resolution is less critical (0.5 mm). The dimensions of the coronary and peripheral arteries of interest require a penetration depth of about 10 mm.

This resolution and penetration depth can be obtained by a well damped, disk-shaped, round transducer with a diameter of 0.7 to 1 mm and an US frequency of 30 MHz (see § 2.1).

From the US theory of § 2.1 it can be seen that for these choices the near field extends over about 5 mm, of which a part is situated in the catheter depending on the scanning configuration (Fig. 2.2-3). The lateral resolution improves from about 1 mm very close to the transducer to 0.5 mm at $z = 4$ mm. The angle of divergence ϕ_d is small (1.5°) and the lateral resolution at 10 mm from the transducer is 0.8 mm.

This shows also that the most homogeneous lateral resolution in the image is obtained, if the scanning configuration of Fig. 2.2-3a is applied. For options b and c the distance between the transducer and the mirror should be small, to avoid decrease of resolution further away from the catheter-tip.

The actual lateral image detail, when imaging a blood-vessel may be better, i.e. differences of the summation of scatter signals can be detected at very small US-beam rotations (see § 2.1).

Considerable reduction of the transducer diameter below 1 mm, at a frequency of 30 MHz, will shorten the near field and increase the diverging angle, so that the lateral resolution will become strongly dependent on the distance to the transducer.

Focusing of the transducer will improve the resolution in the near field, with a smaller beam-width w_f in the focal point. For $z > z_f$, however, the beam will diverge considerably, causing rapid decrease of lateral resolution.

The more homogeneous resolution of the simple (non-focused) 30 MHz transducer with a diameter of 0.7 to 1 mm is preferred. This determines the outer diameter of the catheter to a value > 1 mm, which is an acceptable restriction (see § 2.3).

For larger vessels like the aorta (inner diameter 20-30 mm) a lower frequency should be chosen to be able to image the whole cross-section at once. 15-20 MHz may be a convenient frequency for this application. Because of the lower resolution, the pathological objects of interest should also be larger in this case.

Application of higher frequencies (40-50 MHz) suffers from higher attenuation. Fig. 2.1-3 shows that the penetration depth at these frequencies is not sufficient to cover the whole region of interest around a vessel lumen, except for very small vessels. However, Fig 2.1-3 is a general representation of the frequency dependent attenuation at present, not considering specific properties of piezo-electric transducers at certain frequencies or techniques to improve signal to noise ratio's, to be developed in future.

A side problem is the change of position of the focal point. In case the scanning configuration of Fig. 2.2-3a is applied, the diameter of the transducer should be reduced with about 20 % to keep the focal point of the US beam in the middle of the radial distance of interest ($z_f \approx 4$ mm), in order to ensure optimal lateral resolution (see eq. 2-2). This will cause a reduction of the sensitivity of the transducer to about 60 %. Application of scan-configuration b or c of Fig. 2.2-3 may be a better solution.

Scan speed and frame rate

Arteries in vivo pulsate with a frequency of about 1 Hz, transmitting the pressure pulse-wave of the heart. This results in periodic vessel deformations. Some arteries perform (periodic) translations, due to the motion of the structures or organs in which they are imbedded or to which they are attached and by doing so, changing the position of the catheter-tip in the vessel. The coronary arteries for instance move vigorously with the heart muscle (again with a periodicity of about 1 Hz). Both motion mechanisms will cause image artifacts, if the scan speed is too low. If the amplitude of the relative motion between catheter-tip and vessel-wall is small enough, image artifacts will be acceptably small, when a scan is produced in less than 1/10 of a motion period.

Dynamic analysis of images is only possible if the frame rate is sufficiently high. The most obvious way to meet both requirements is the application of fast continuous scanning, resulting in a frame rate of more than 10 frames/s. Real-time imaging, showing vessel-wall motion smoothly to the eye, can be performed at 25 frames/s. Practical system limitations may determine other frame rates. The slip-rings for signal transfer, as built into the current motor-unit (Fig. 2.4-2), for instance, are specified for a maximum of 1000 rpm, i.e. 16.7 frames/s.

Pulse rate and image resolution

According to eqs. 2-5 to 2-8 the minimum pulse rate PR_{\min} is 19.2ω . At 1000 rpm $PR_{\min} = 2000$ pulses/s, i.e. 120 pulses per revolution or one image-line every 3° . A higher pulse rate may be applied to improve the tangential image detail, possible because of summation of scatter echoes (see § 2.1). A pulse rate of 8.33 kHz, i.e. 500 pulses per revolution or one image-line every 0.7° has been chosen.

Sonolucent window and fluid filling

Rotating parts should not be in contact with the vessel-wall (see further: "Patient safety"), so that the rotating transducer has to be enclosed in the catheter-tip. This requires a sonolucent window in the tip-segment of the catheter-tube. At 30 MHz we found thin-

walled high density polyethylene (HDPE) as well as polymethylpentene (PMP, TPX) to be suitable.

Furthermore US-energy of 30 MHz is not transmitted by air. Therefore at least the tip-compartment should be filled with a fluid, with good US-transmission characteristics. Small air bubbles, left behind, destroy the imaging capabilities of the catheter. Taking into account the possibility that some of the fluid may leak into the blood-stream, choices of the fluid are limited to blood compatible water-based solutions.

§ 2.3 Catheter technology

Catheters in general are tube-like delivery devices for fluids, micro-instruments, sensors, etc. to any part of the body and they are in wide-spread use in clinical practice. Catheters are preferably introduced through natural passageways like the gastro-intestinal track, the urethra or blood-vessels, to minimize surgical traumas.

A scala of different catheter types is used for cardiovascular applications. E.g. electrode-catheters are used for cardiac stimulation or diagnostics of cardiac electro-physiological diseases. Sensor-catheters register blood-flow or blood-pressure, pH, pO_2 or pCO_2 . Angio-catheters deliver an X-ray contrast medium to the sight of interest in order to record Röntgen angiograms. And a variety of catheter-based interventional techniques has already been discussed in the first chapter.

It may be clear from this that the development of a new catheter on the one hand will make use of all the available technological knowledge on e.g. blood-compatible materials, production methods, sterilization and packaging, but on the other hand will have to fit into the common practice of clinical catheter use in order to benefit from available supporting devices and methods. This already determines the possible catheter introduction methods and standardized connections to the supporting devices. Some specifications for the catheter design are set by this.

Target and introduction method

The blood-vessels mostly affected by atherosclerotic lumen obstructions, with potentially hazardous consequences, are the femoral artery (leg artery, Fig. 1-2) and the coronary arteries. The first one is also referred to as a peripheral artery. These blood-vessels are chosen to be the first targets for catheter-investigation by intravascular US imaging. The

conditions and catheter specifications for peripheral and coronary catheterization differ greatly, so they will be discussed separately.

Coronary catheterization

The most commonly used place to introduce a catheter into the vascular system is in the groin, where the femoral artery runs close to the body surface. First a thin-walled plastic sheath is placed into this artery. The proximal side of the sheath contains a diaphragm valve. The valve closes around any catheter to be advanced, preventing the loss of blood. The sheath is directed towards the iliac artery (Fig. 1-2).

A catheter is advanced through the small part of the femoral artery, the iliac artery into the descending aorta (Fig. 2.3-1). Further advancement leads the catheter-tip through the aortic arch, into the aortic root, where the two main coronary arteries can be entered. Especially this last sharp curve into the coronaries will hardly be possible without means of catheter guidance.

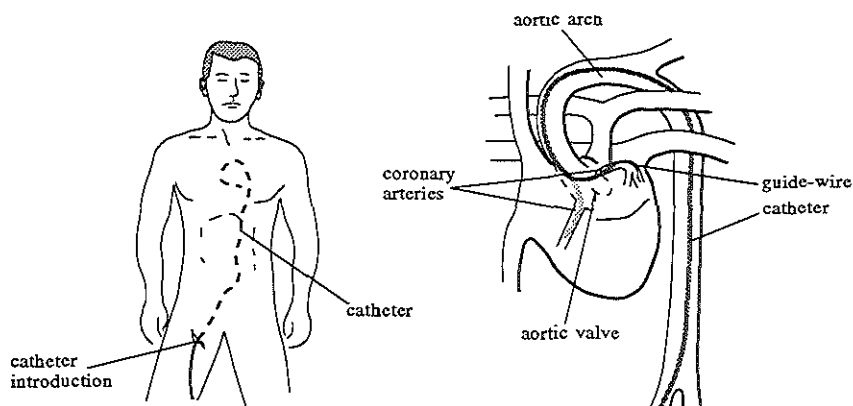


Fig. 2.3-1 Most common site of catheter introduction and advancement to the coronary arteries.

Two procedures are commonly used. Before introduction of the catheter a guide-wire is manipulated in place, even further advanced than the target sight.

A guide-wire is a thin ultra-flexible wire construction, mostly helically wound. Its tip can be steered well from outside the body, by translation and rotation of the wire. This way all the right side-branches can be entered and passed with the help of angiographic view. If the catheter is flexible enough and has a free lumen, it can be advanced "over-the-wire" and will therefore closely follow its track. In case of absence of this lumen, the catheter should have a construction at the tip to be hooked onto the guide-wire before advancement (mono-rail, side-saddle).

If the catheter is too stiff to be directed by the ultra-flexible guide-wire, a less rigid

guiding catheter, a larger diameter hollow tube, may be advanced prior to the catheter in question, which then will be advanced through its lumen.

The diameter of the coronary arteries varies from 3 mm proximally to less than 1 mm more distally. Unlike peripheral catheterization, total obstruction of a coronary vessel by the catheter itself is not allowed, but for a very short period of time. The catheter diameter therefore is a more critical design specification. The catheter diameter should be smaller than 1.5 mm (4.5 French⁽¹⁾) and one should strive for a diameter of 1 mm or less (3 French). For the coronary application a catheter-length of 1.5 m is suitable.

The tortuous pathway of the coronary catheter requires high flexibility, at least for the distal part, which is contained in the aortic arch and the coronary artery.

Peripheral catheterization

For peripheral catheterization the same place of introduction is used. The introduction sheath now is directed towards the knee. From this location of introduction a catheter can easily be advanced into the leg artery, following an almost straight track.

The diameter of a normal leg artery varies from about 4 mm at the height of the femoral artery, down to less than 2 mm in the popliteal artery (Fig. 1-2). Depending on the target location in the femoral artery the catheter diameter can be 1.5 to 2.5 mm (4.5 to 7.5 French size).

A catheter length of 1 m is suitable for this application.

Except for the introduction angle, the catheter follows a fairly straight path, so a high flexibility is not required.

However, the peripheral catheter should be flexible enough to make use of guide-wire facilities, in order to prevent the catheter-tip from advancing into a dissection or a false lumen of the vessel, causing considerable damage.

Patient safety

Blood-/bio-compatible materials

The effects of the short- or long-term contact between man-made materials and the living body, as a part of medical practice, are studied in the development of bio-materials [10]. Materials or their surfaces are modified or new materials are being developed to minimize the negative effects of their presence inside the body.

⁽¹⁾The French is a commonly used circumferential catheter size, where 1 French corresponds with a diameter of 1/3 mm.

Evidently the outside of a catheter should be made of a non-toxic material, but apart from that the materials should be blood-compatible in a broader sense. The presence of the catheter in the blood-stream should not lead to excessive blood-reaction, i.e. haemolysis, the falling apart of red blood cells or adhesion of proteins and blood-platelets to the catheter surface eventually leading to the forming of thrombi. The nature of the material as well as the surface finish determine its blood-compatibility [11]. Polymer materials with sufficient blood-compatibility are known from current catheter technology. Catheter-tubing of several sizes, with the right surface finish specifications, is readily available on the market.

Materials like poly-urethane (PUR), poly-ethylene (PE), teflon (PTFE) and others are used for intravascular catheter applications. For materials used inside the catheter, it is more difficult to consistently use only compatible materials. The functionality sometimes demands the use of copper, silver and other potentially hazardous substances. A pragmatic solution to the use of these materials is to prevent exposure to the blood-stream and to take measures to prevent leakage of toxic components, by diffusion or extraction, into the blood-stream. Specific testing can give clarity on this point.

A diagnostic catheter of this kind is meant to be used during a maximum period of about one hour. For catheters that are used for long-term monitoring more severe requirements with respect to bio-compatibility will be applied.

Non-traumatic design

Sharp edges should be avoided not to damage the delicate inner lining of the blood-vessel. Only smooth surfaces may be applied.

The inner wall of the blood-vessel has to be shielded from mechanically rotating parts, which should be confined to the inside of the catheter; the blood-vessel should only be in contact with a static catheter-tubing.

The catheter has to be able to follow the tortuous pathway of the blood-vessel, without deforming the vessel too much. The catheter should therefore be flexible enough. All electrical and mechanical failure-modes have to be analyzed and, where necessary, safety measures should be taken.

Disposable

Intravascular catheters are generally only for one-time-use. This reduces the risk for infectious reactions due to the presence of bacteria, viruses or body-alien substances like proteins from earlier use. Only very scarce or expensive catheters may be cleaned, sterilized and used several times [12].

Definition of the product as a disposable solves the problem of reliability in functionality and safety after many cycles of use, cleaning and sterilization. Instead the product should be inexpensive enough to be accepted as a one-time-use catheter.

One may consider the possibility of a modular catheter-system, with a disposable catheter-sheath, which is in contact with the patient's blood, and a re-usable interior, consisting of the US-transducer and the driving mechanism of the catheter-tip [13]. The catheter-sheath should not allow the blood to enter, despite the presence of an opening in the tip of the sheath to facilitate fluid filling prior to use. One-way openings like membranes or valves are not easily produced reliably in this small size. A completely disposable catheter, therefore, seems to be the safest solution.

Sterilization

Several methods of sterilization are available for medical products, some of which cannot be applied to polymers, because of the high temperatures of the process. For catheters and other medical disposables gamma-radiation and ethylene-oxide (ETO) gas-sterilization are most commonly used [14].

Many polymers deteriorate under the influence of a high dose of gamma-radiation, so that the functionality and safety of the product may be affected. ETO-sterilization should not be applied to any product containing water, where the gas can be in contact with the water, because of the forming of the toxic product ethylene glycol.

§ 2.4 The intravascular US-imaging system

At this point the whole intravascular US-imaging system will be discussed briefly. In the next chapters, Chapter 3 and Chapter 4, the choice for mechanical scanning by flexible drive-shaft rotation transmission will be accounted for.

A schematic drawing of the system is presented in Fig. 2.4-1. It is based on mechanical rotational scanning, where a single transducer (1) in the catheter-tip is driven by an external motor through a flexible drive-shaft (3). A sonolucent dome (2) covers the rotating element. By processing the signal the scan image can be displayed in video format on a monitor.

The system consists of three basic parts: the disposable catheter, the driving unit and the main-frame console. In the clinical setting the first two will be situated at the bed-side. The main-frame console is standing on wheels and can be positioned anywhere in the vicinity, as far away as the electro-optical cable allows. The structure of the catheter has been outlined here and especially mechanical aspects of the catheter-tip rotation will be described in detail in the next chapters. The basic concepts of the driving unit and the main-frame will be described in this paragraph.

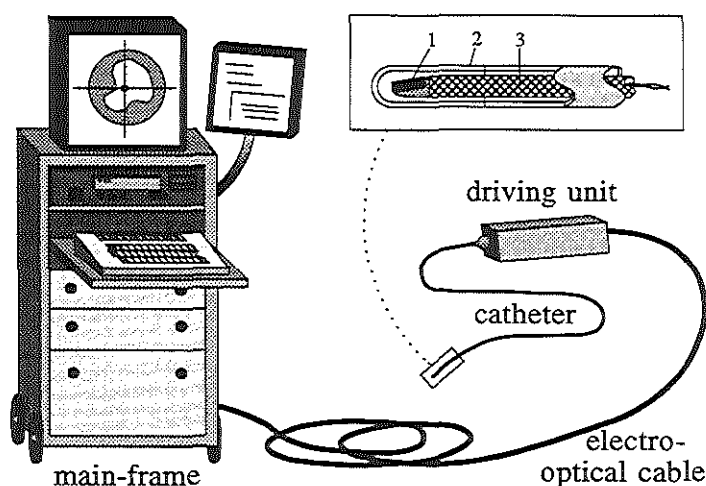


Fig. 2.4-1 Schematic of the intravascular echo-imaging system, based on mechanical rotational scanning. US-transducer (1), sonolucent dome (2), flexible drive-shaft (3).

Driving unit

The disposable catheter is connected to a non-disposable driving unit, which contains a driving motor and echo-signal processing electronics (Fig. 2.4-2).

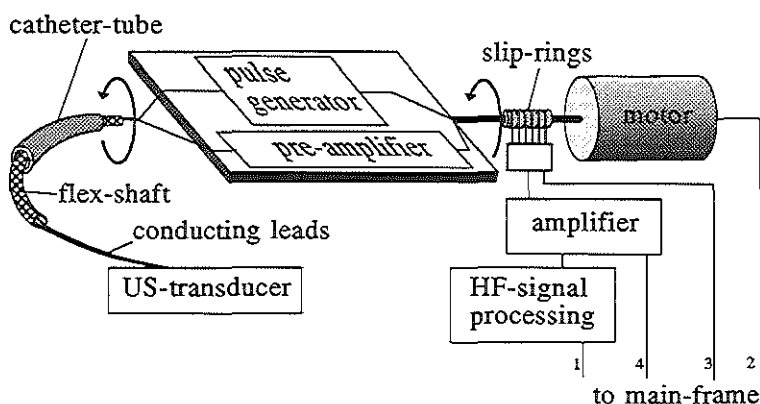


Fig. 2.4-2 Schematic drawing of the driving unit (see also Fig. 2.4-3).

The rotating transducer in the catheter-tip implies rotating electrical leads, which can be achieved by leading them through the hollow flexible drive-shaft. Slip-rings in the driving

unit establish contact between these rotating leads and the static electronics.

The high peak-current of the transducer excitation pulse cannot be transmitted over small slip-rings, because the high current density will cause erosion of the contact surfaces. Therefore it is necessary to define the electronics for excitation pulse generation on a rotating PC-board, so that only the much lower supply current has to be sent over the slip-rings.

On the same board a pre-amplifier is mounted to amplify the echo-signals. This reduces the effect of contact noise, introduced by the slip-rings.

Communication with the main-frame is established through a long cable, in which some communication lines make use of fiber-optics instead of galvanic connections (see also Fig. 2.4-3). This is done to reduce interference from main-frame signals and other EM field noise sources in the catheterization lab.

Main-frame console

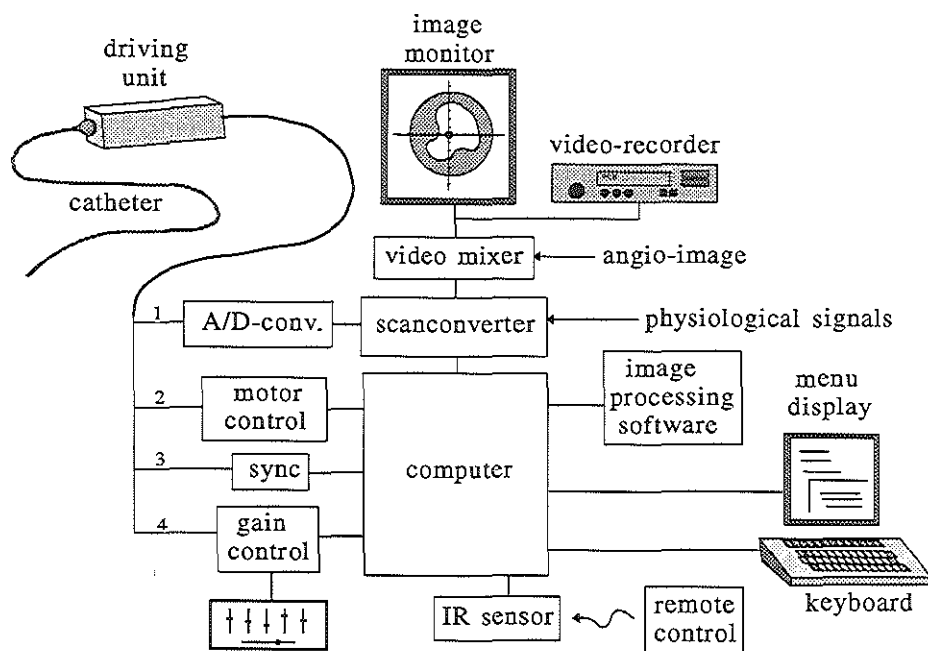


Fig. 2.4-3 Schematic drawing of the main-frame (see also Fig. 2.4-2).

A schematic drawing of the main-frame console is presented in Fig. 2.4-3.

The incoming echo-signals are first digitized. The signals originate from circular echo-scanning and therefore represent a real-time polar image. In the scan-converter this image

is processed on-line into video format, after which it can be displayed and/or recorded. A computer controls the system components according to parameters, set by an operator through keyboard and menu-display. The computer can also perform on-line or off-line image-processing for analysing and quantization purposes.

References

1. Hill C.R., Kratochwil A., (eds.), *Medical Ultrasonic Images*, papers presented at a European Symposium by the European Federation of Societies for Ultrasound in Medicine and Biology in association with Polaroid Corporation, Brussels, January 31-February 1, 1981, Excerpta Medica, Amsterdam-Oxford-Princeton, 1981.
2. Christensen D.A., *Ultrasonic Bioinstrumentation*, John Wiley & Sons, New York-Chichester, 1988.
3. Weyns A., *Studie en optimalisatie van elementaire diagnostische ultrasoonzenders en ultrasoonontvangers*, Ph.D Thesis of Catholic University Leuven, Faculty of Applied Sciences, Department of Electronics, 1982.
4. Bom N., *New concepts in echocardiography*, Ph.D. Thesis, Department of Medicine, Rotterdam, The Netherlands, 1972.
5. Wells P.N.T., *Physical principles of ultrasonic diagnosis*, Academic Press, London, p. 23, 1969.
6. Bom N., Lancée C.T., Gussenhoven E.J., Li W., Hoff H. ten, *Basic principles of intravascular ultrasound imaging*, In: *Intravascular ultrasound imaging*, Tobis J.M., Yock P.G., eds., Churchill Livingstone, New York, p. 8, 1992.
7. Bom N., Lancée C.T., Van Egmond F.C., *An ultrasonic intracardiac scanner*, *Ultrasonics* 10: 72-76, 1972.
8. Lancée C.T., *A transesophageal phased array transducer for ultrasonic imaging of the heart*, Ph.D. Thesis, Erasmus University Rotterdam, The Netherlands, p. 46, 1987.
9. Steinberg B.D., *Principles of aperture and array system design: including random and adaptive arrays*, John Wiley & Sons, New York, p. 74, 1976.
10. *Society for Biomaterials in the Netherlands, Research & Business in Biomaterials, Conference proceedings, Lunteren the Netherlands, November 14th, 1990.*
11. Olijslager J., *The development of test devices for the study of blood material interactions*, Ph.D Thesis, Technical University Twente, 1982.
12. Herten J.H.S. van, *Juridische aspecten van hergebruik van medische hulpmiddelen bestemd voor eenmalig gebruik*, *Pharmaceutisch Weekblad* 122: 618-625, 1987.
13. Crowley R.J., Couvillon L.A.Jr., Abele J.E., *Acoustic imaging catheter and the like*, United States Patent 4,951,677, March 21, 1988.
14. Gopal N.G.S., *Radiation sterilization of pharmaceuticals and polymers*, *Radiol. Phys. Chem.* 12: 35-50, 1978.

CHAPTER 3 Mechanical scanning in intravascular ultrasound imaging

§ 3.1 Image artifacts due to non-ideal catheter-tip motion

The echoes of an emitted US-pulse, sent in a certain direction, are displayed in grey-scale value and represent one radial image-line on the screen. The image-line is defined by the echo-signal of the pulse, its location of origin and the direction in the cross-sectional plane. In general the latter two are not being monitored and instead the imaging process is based on a few assumptions. The location of origin, which coincides with the catheter-tip position is assumed not to change within one 360° scan, which means that no radial or tangential tip-motion will occur with respect to the blood vessel. Furthermore uniform catheter-tip scan-rotation, with a well-known angular velocity, will ensure correct angular correlation of the image-lines on the display. A reference direction (e.g. the direction at time $t = 0$) ensures correlation of the absolute orientation of images. However, these assumptions are not generally valid and the effects of unpredictable catheter-tip motion on the reliability of the image will be studied in this paragraph.

Image artifacts due to radial and tangential catheter-tip motion

Radial and tangential catheter-tip motion with respect to the blood-vessel originate either from motion of the blood-vessel or from the catheter-tip itself, in which case the motion is related to the driving motion. The first is already dealt with in the previous chapter and is no real problem, if the scan-speed is high enough.

In practice the catheter is supported on many points by the tortuous blood-vessel, through which it has been advanced. This more or less immobilizes the catheter. The free length of the catheter-tip, where it is hardly supported by the vessel-wall, is a factor in the possible occurrence of radial tip-motion. The catheter-tip may also be stabilized by the guide-wire, which runs through its free lumen or to which it is attached by a "side-saddle" construction.

Naturally the elimination of the causes of radial and tangential catheter-tip motion is preferred. Therefore it is important to apply small well-balanced rotating masses, realize well-aligned supports of rotating elements and avoid a rotating frequency close to the fundamental frequency of the bending-mode motion of the free tip-length.

Image distortion due to periodic radial catheter-tip motion, with the same frequency as the driving frequency is shown by Fig. 3.1-1.

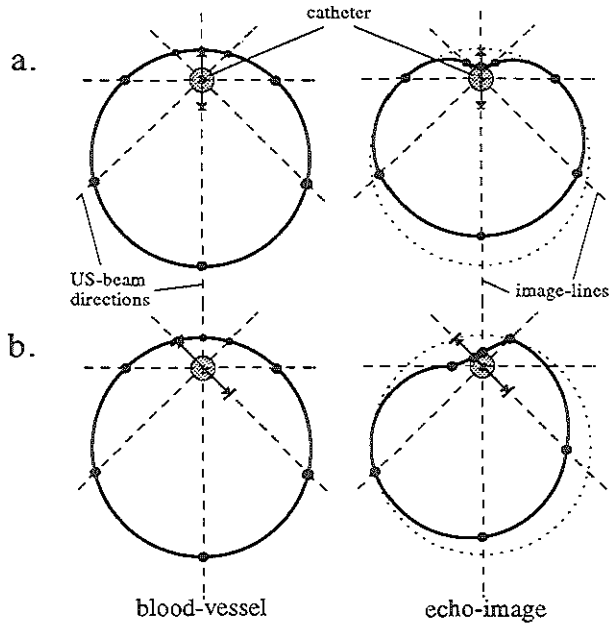


Fig. 3.1-1 Image distortion caused by periodic radial catheter-tip motion (arrows), in case the periodicity of this motion corresponds with the scan-rotation. Radial catheter-tip motion perpendicular to the vessel wall (a) and not perpendicular to the wall (b).

Tangential catheter-tip motion occurs when the catheter-tip describes circles around the supposed static location of the catheter in the blood-vessel. If the cause can be found in the catheter itself, the periodicity of the motion will be related to the scan-rotation in the catheter-tip. The effect is an unreal representation of the radial measures of the lumen of the blood-vessel: the lumen will be shown either too small or too large.

Image artifacts due to non-uniform catheter-tip scan-rotation

In general the polar image on the display is built up, with the assumption of a uniform catheter-tip scan-rotation. It turns out to be difficult to guarantee uniform angular velocity at the catheter-tip, although the average angular velocity, determined over a sufficient number of rotations, is kept constant. A rotation error angle θ [rad] can be defined as:

$$\theta = \psi_{act} - \psi_{exp} \quad (3-1)$$

where

ψ_{act} [rad] = the actual tip-rotation angle, traversed since time $t = 0$ and

ψ_{exp} [rad] = ωt = the expected rotation angle, assuming uniform catheter-tip scan-rotation with a given angular velocity ω [rad/s].

The unpredictable rotation error angle θ causes misplacement of image-lines on the display, because an image-line, recorded at a rotation angle ψ_{act} , is displayed at an angle ψ_{exp} . This causes image artifacts of several kinds, depending on the nature of the course of the error angle in time [1].

The error angle can have a constant (θ_c), a periodic (θ_p) and a stochastic (θ_s) component. The first causes a rotation of the whole displayed image over an angle θ_c , so that without the help of an anatomic "land-mark" the absolute orientation of the image with respect to the patient's anatomy will be lost. For some applications this may not be of great importance.

The stochastic error causes sequential images of the real-time imaging system not to match, so that the real-time aspect will be unstable, i.e. restless or even blurred to the eye. This error should be kept very small.

The periodic error angle repeats itself in time. Depending on the driving mechanism this error may repeat itself with the driving frequency ω . If other frequency components than the driving frequency or its higher harmonics are present, the effect on the image is similar to that of the stochastic error.

The periodic error angle, which repeats itself every revolution with high precision, represents a periodic function $\theta_p(\omega)$.

In this case the succeeding images will match, so that a sharp real-time image can be obtained. But image-lines do not appear on screen in accordance with the real cross-sectional geometry of the blood-vessel. The effect of the periodic error angle on the image reliability can be studied by simulation, using a sine function to describe the course of the periodic error angle in time. According to the mechanism causing this error, it will either be a sine function of the theoretical rotation angle ψ_{exp} , so that:

$$\theta_p = \theta_0 \sin \psi_{exp} = \theta_0 \sin \omega t \quad (3-2)$$

or of the actual rotation angle ψ_{act} , so that:

$$\theta_p = \theta_0 \sin \psi_{act} = \theta_0 \sin(\psi_{exp} + \theta_p) = \theta_0 \sin(\omega t + \theta_p) \quad (3-3)$$

This renders a recursive definition of the angle error function.

For the latter the results of the simulation can be seen in Fig. 3.1-2, for different values of the peak-to-peak error angle ($= 2\theta_0$), showing misplacement of imaged objects and expansion or compression of these objects more distinctly for larger periodic error angles.

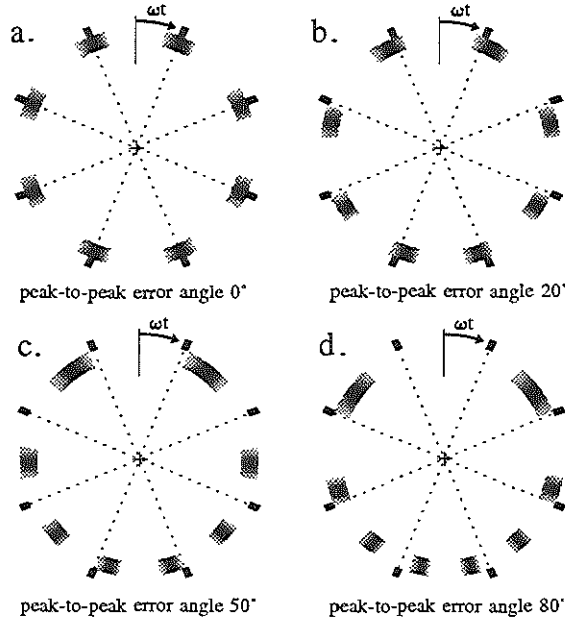


Fig. 3.1-2 Simulation of the image distortion in case of a sine-shaped rotation error angle as a function of the actual rotation angle ψ_{act} . The ideal image of eight US-reflectors equally distributed around the catheter-tip, peak-to-peak error angle is 0° (a). Distorted images of the same reflector configuration when peak-to-peak error angle is 20° (b), 50° (c) and 80° (d). Note regions of expansion and compression of the image.

The misplacement of an object in the image is given by the error angle θ_p itself and expansion or compression of the object is determined by the local expansion rate, which can be defined as:

$$\text{Expansion rate} = \frac{d\psi_{exp}}{d\psi_{act}} = \frac{d\psi_{exp}}{d(\psi_{exp} + \theta)} = \frac{\omega dt}{\omega dt + d\theta} = \frac{\omega}{\omega + \frac{d\theta}{dt}} \quad (3-4)$$

An expansion rate < 1 indicates local image compression.

The periodic error angle represents a danger to the correct clinical interpretation of the image. Over- or underestimation of the blood-vessel occlusion may occur, resulting in the choice of incorrect therapeutic measures. The degree of misinterpretation is, except from the peak-to-peak value of the periodic error angle, also dependent on the blood-vessel geometry and the position of the scanning catheter-tip in it. A concentric stenosis imaged by a catheter-tip positioned in the centre, is not sensitive to this problem, but in an asymmetrical situation, illustrated in Fig. 3.1-3, quantification of the rate of stenosis may suffer from errors of tens of percents. Fig. 3.1-3 shows a slightly distorted and a severely distorted US-image of an iliac artery, recorded in vitro, with an intravascular US-imaging system, where the catheter-tip rotation is established by flexible drive-shaft transmission.

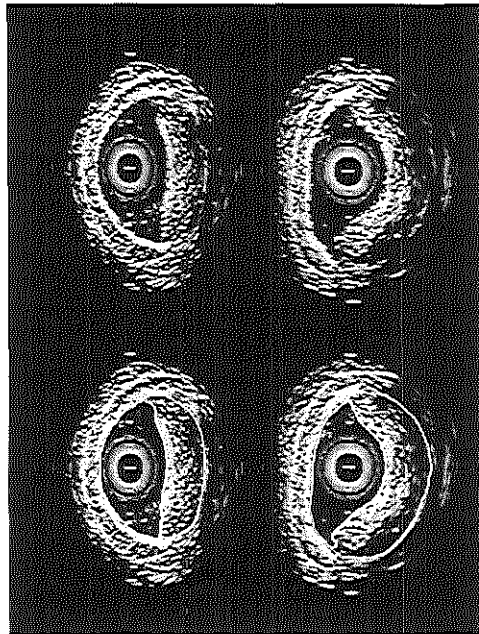


Fig. 3.1-3 Distortion of the US-image of an iliac artery, in vitro, with apparent obstructive disease. The slightly distorted image of the vessel cross-section (left) suffers from a small periodic scan-rotation error of 9° peak-to-peak. The rate of stenosis is 41 % of the original lumen area of 26.1 mm^2 . The more distorted image of the same vessel cross-section (right) is recorded at a periodic scan-rotation error angle of about 55° peak-to-peak. It shows a rate of stenosis of 55 % of a supposedly original lumen area of 32.1 mm^2 . These figures have been determined with contour tracing software (bottom) [2].

Note: these images do not represent the imaging performance of flex-shaft driven catheters in general, functioning in the clinical setting. The image quality in terms of image distortion depends on the correct choice and realization of many practical and constructive parameters (see Chapter 4). Here only the effects of non-uniform catheter-tip scan-rotation are illustrated.

Specifications for adequate catheter-tip scan-rotation

A lower limit to the scan speed of 1000 rpm is given by the need for real-time imaging and to avoid image artifacts due to relative motion of the imaged objects (§ 2.2). Very high scan speeds may cause other problems, so that a maximum limit has to be defined also.

Fire-hose effect

High constant or momentary rotation speeds may cause problems for the acoustical system. In the time interval between emission of the acoustical interrogating pulse and reception of the echo, the transducer will rotate over a certain angle dependent on the momentary rotation speed. At high speeds the line of sight in reception will be swept away from the original emission position so much, that it effects the image quality. This phenomenon is known as the fire-hose effect (Fig. 3.1-4). The sensitivity for echoes from further away structures will diminish, resulting in a smaller depth of imaging. And the image lines (lines of highest echo amplitude) will become slightly curved, causing yet another type of image deformation if not corrected for [1].

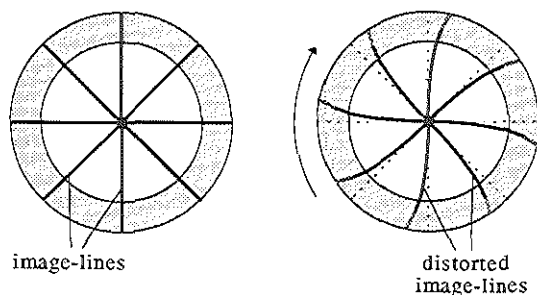


Fig. 3.1-4 The fire-hose effect [1].

The velocity of ultrasound in soft biologic tissue is comparable to the velocity in water (≈ 1500 m/s). The intravascular application of these catheters, using 30 MHz ultrasound, is focused on the smaller arteries. The typical maximum penetration depth needed for imaging of these arteries is 10 mm. The time interval between emission of the US-pulse and reception of the echoes from the furthest away structures is therefore about 13 μ s. At 1000 rpm this corresponds with a traversed angle of about 0.1° , which is negligible. But at 10,000 rpm or more this angle increases to 1° or more, which is in the same order of magnitude as the divergence of the US-beam and the angular resolution (see Chapter 2). It may be concluded that the constant or momentary rotation speed of the US-beam should not exceed 10,000 rpm.

Data-acquisition

The signal processing, specially designed and built for the echo-catheter imaging system (Fig. 2.4-3), is based on the generation of 500 image-lines per revolution and a maximum of 3600 frames per minute. Data-acquisition therefore has a maximum speed of 30,000 image-lines per second. At nominal rotation speeds > 3600 rpm, maintaining real-time display, the tangential resolution has to be reduced. If these high speeds only occur momentarily and the nominal rotation speed is ≤ 3600 rpm, the data-acquisition should be redesigned or buffers for temporary data-storage should be provided.

Constant error angle θ_c

As explained earlier, the three components of the scan-rotation error angle are not equally important for the image reliability. The constant error, causing the whole image to rotate, may not be that significant, as long as the loss of the absolute orientation of the image with respect to the patient's anatomy is not so important.

Stochastic error angle θ_s

The stochastic error angle always disturbs the real-time aspect of the image and should be minimized by ensuring a high degree of reproducibility of succeeding images. Imaging is performed with 500 radial image lines per revolution, which determines the tangential resolution in the visualization of biological tissue (see Chapter 2). A misfit of two succeeding images in the order of one degree can therefore already disturb the real-time aspect of the image. The average angular velocity over one revolution $\bar{\omega}$ should be close to constant. The stochastic error angle is caused by small stochastic changes in the load, i.e. the total driving torque. From $\psi = \bar{\omega}t$ it can be derived that:

$$\frac{\Delta\psi}{\psi} = \frac{\Delta\bar{\omega}}{\bar{\omega}} + \frac{\Delta t}{t} \quad (3-5)$$

where

ψ [rad] is the scan-rotation angle

$\Delta\psi$ [rad] is the scan-rotation error angle ($= \theta_s$)

$\Delta\bar{\omega}$ [rad/s] is the deviation of the average angular velocity over one revolution from the nominal angular velocity $\bar{\omega}$ ($\bar{\omega}$ = the average angular velocity over many revolutions)

Δt [s] is the error in time measurement

Note: $\Delta\psi$ may be dependent on the rotation phase-angle.

Because time measurement can be performed very accurately, the last term in eq. 3-5 can be neglected. The error angle of one degree per revolution therefore determines the stability of the angular velocity according to:

$$\frac{\Delta\bar{\omega}}{\bar{\omega}} = \pm \frac{1}{360} = \pm 0.003 \quad (3-6)$$

Analysis of the stiffness of a driving mechanism, which determines the sensitivity of the angular velocity to changes in the torque and an estimation of occurring disturbances of this torque will show whether this specification can be met.

Periodic error angle θ_p

Periodic errors with a frequency one order of magnitude lower than the scan-rotation frequency cause the entire image to rotate forwards and backwards over a certain angle. Sensitivity of quantities determining the constant error to slightly varying catheter geometry (with the heart beat) can cause this phenomenon. It can be annoying and its effect should be minimized.

Periodic errors with higher frequencies, other than the driving frequency or its higher harmonics should be treated the same way as stochastic errors.

Without knowledge concerning the clinical protocol utilizing intravascular US imaging, it is hard to define a maximum degree of acceptable image distortion due to the periodic error, which repeats itself related to the driving frequency. A qualitative judgement of Fig. 3.1-2 may show justification of the acceptance of a maximum peak-to-peak periodic error angle of 20° .

§ 3.2 Principles of catheter-tip rotation

In this paragraph several possibilities are discussed to establish catheter-tip rotation. It is not meant to give a complete overview. It will, however, indicate the problems to be solved for each principle and clarify the pragmatic reasoning on which the conclusions are founded.

§ 3.2.1 Basic principles

In search of possible ways to realize catheter-tip rotation it is helpful to split up the overall function in the energy-flow scheme, into partial functions:

energy source → transformer → transmission → transformer → catheter-tip
rotation

The possibilities of energy transmission other than through the catheter-body will be disregarded, because they will lead to large costly equipment, for instance to create

powerful rotating magnetic fields, etc.

The key-function of the general scheme, determining most of the choices, is the energy transmission through the catheter. Depending on this choice one of the two energy transformers may be left out. A fundamental choice is to design a small motor into the catheter-tip (schemes A1 and A2) or to keep the motion generating motor at the proximal end of the transmission line (catheter), so that it can be much larger (schemes B1 and B2). The most plausible energy-flow schemes can now be given in a more concrete form.

Scheme A1.

electrical energy source	→	electrical leads through catheter	→	motor	→	motion transformation	→	catheter-tip rotation
-----------------------------	---	--------------------------------------	---	-------	---	-----------------------	---	--------------------------

Scheme A2.

electrical energy source	→	electrical leads through catheter	→	motor	→	catheter-tip rotation
-----------------------------	---	--------------------------------------	---	-------	---	--------------------------

Scheme B1.

electrical energy source	→	motor	→	motion transmission	→	motion transformation	→	catheter-tip rotation
-----------------------------	---	-------	---	---------------------	---	-----------------------	---	--------------------------

Scheme B2.

electrical energy source	→	motor	→	rotation transmission	→	catheter-tip rotation
-----------------------------	---	-------	---	-----------------------	---	-----------------------

In the next paragraph several working-methods for catheter-tip rotation, derived from these energy-flow schemes will be proposed and discussed, partly as a summary of the alternatives given by [3].

§ 3.2.2 Working methods of catheter-tip rotation

Based on energy flow scheme A1:

Linear electro-magnetic motor with translation-rotation transformation

An example of a linear electro-magnetic motor, realizing an axial reciprocating motion in the catheter-tip is depicted in Fig. 3.2-1 [3, p. 59]. By leading an electrical current through the coils, the iron core is magnetised and drawn into the spool. The spring will be compressed, generating a force in opposite direction, which will drive the iron core back to its original position, after disconnecting the current.

The iron core is connected to a translating screw. The screw has a square or triangular cross-section, with a twist around its central axis. The translation is performed in both directions and is transformed into a rotational motion by a form-plate, through which the screw is sliding. The form-plate has a corresponding square or triangular hole and will rotate as the screw is sliding through it.

The screw and form-plate should have well-defined dimensions to ensure a well-known, reproducible translation-rotation transformation, which is necessary in order to accurately derive the rotation angle from the motor-control. A test model of the translation-rotation transformation on a larger scale showed a well-reproducing hysteresis curve, with a high degree of linearity. However, down-scaling to the catheter-tip dimensions would demand an extreme accuracy of the production method of the screw and the whole catheter-tip construction.

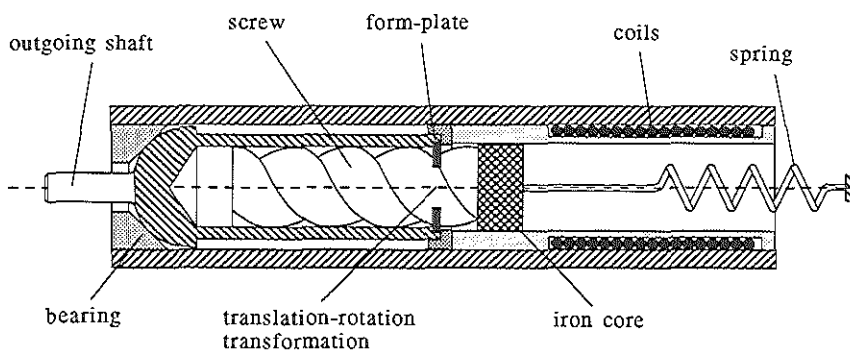


Fig. 3.2-1 Linear electro-magnetic motor with translation-rotation transformation [3, p. 60].

Another disadvantage of this concept is the stiff length of the catheter-tip structure, which is at least twice the travel of the screw with respect to the form plate. This length will be between 5 and 10 mm, dependent on the pitch-angle of the screw, which cannot be chosen too small, because of increasing friction. Consequently the development of this concept has not been pursued any further.

Based on energy flow scheme A2:

Electrostatic micro-motor

The principle of the electrostatic motor is the attracting force between two charged, parallel capacitor plates. If the plates only partly overlap, this force also has a component parallel to the plate surfaces, which by placing the plates around a centre of rotation causes a driving torque [4, 5].

In conventional technology the electrostatic motor hardly finds any application, because the maximum torque of the motor is more than four orders of magnitude lower than the torque of an electro-magnetic motor of the same dimensions [6]. This is due to the relatively weak electric field E_{\max} and therefore low energy density in the air gap between rotor and stator, because of the limited break-down voltage in the gap. In case of an air gap of 1 mm, at atmospheric pressure, $E_{\max} \approx 3 \cdot 10^6$ V/m [4].

For very small motors, with very small air gaps, down to 2 μm , this situation changes, due to the Paschen effect [7]. The maximum electric field can reach values 50-100 times higher than in the first situation, approaching the value for vacuum: $E_{\max} = 3 \cdot 10^8$ V/m, probably because of the scarce presence of ions in this small gap to support break-down. In this case the theoretical torque produced by the electrostatic concept is competitive with the torque of the electromagnetic motor and at these small dimensions, motor diameters of tenths of millimetres, the electrostatic concept may even show to be more efficient [6].

The electrostatic micro-motor has to be produced with high accuracy to guarantee a constant small air gap size. In the last years micro-mechanical structures, based on silicon technology have been developed (Fig. 3.2-2). This way much smaller mechanical components and whole mechanisms can be built with an accuracy, that is superior over conventional precision engineering technology. Silicon based electrostatic micro-motors have been built and they have shown the ability to rotate a micro-structure, with a rotor size of 0.1 mm [8, 9].

However, many basic and practical problems are to be solved before utilization of this concept. The theoretical torque generated between rotor and stator may be large enough

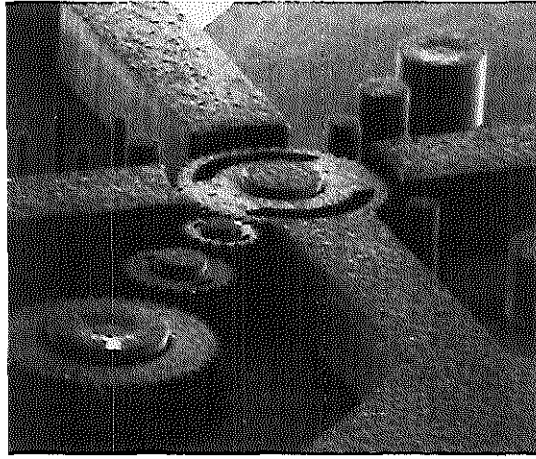


Fig. 3.2-2 Electron microscope picture of an electrostatic micro-motor with a rotary speed reducing gearing, produced by silicon technology. The diameter of the rotor is 100 μm (photo: by courtesy of the Centrum voor Micro-elektronica (CME), Enschede, The Netherlands).

to drive an acoustic mirror in water, but the friction losses in a motor assembly are unknown. The planar silicon technology does not provide means of harnessing the mechanical output torque, i.e. provide an outgoing drive-shaft [6]. The motor would be very sensitive to lateral forces applied to such a shaft. Life expectancy is only a few minutes, while about one hour is required [3, p. 24]. If the angular speed of the motor is too high, a toothed gearing, produced by the same technology, will reduce the speed and increase the available torque. But this is an elaborate and costly development.

In several years from now this technology may mature into practical applications.

Electro-magnetic micro-motor

A micro-motor based on conventional precision engineering technology is in closer reach [10]. As a joint effort of the Erasmus University Rotterdam and Dutch industry an electro-magnetic synchronous micro-motor has been developed. Prototypes of a motor with a diameter of 1 mm have been produced successfully and have shown to be able to drive a small acoustic mirror in water. A rotor of permanent magnetic material, with a diameter of 0.7 mm, rotates in two bearings, driven by a stator with current-conducting leads. Testing for uniform rotational behaviour at a convenient current and rpm, has led to several design changes in stator, shaft and bearings.

In a first prototype the stator conductors consisted of four sevenfold coils of thin copper wire. The production of these coils, the positioning in the stator and the connection to the motor-leads turned out to be critical. Also, the resulting distribution of conductors around the rotor was sub-optimal. Therefore we developed a flex-print based stator with a more optimal configuration of conductor leads. This concept is easier to reproduce and provides better perspectives for economical manufacturing and further miniaturization (Fig. 3.2-3) [11].

A periodic error angle of less than 10° peak-to-peak can be achieved at a rotational speed of 3600 rpm. Catheter-tip prototyping, utilizing this motor to drive an acoustic mirror is now in process.

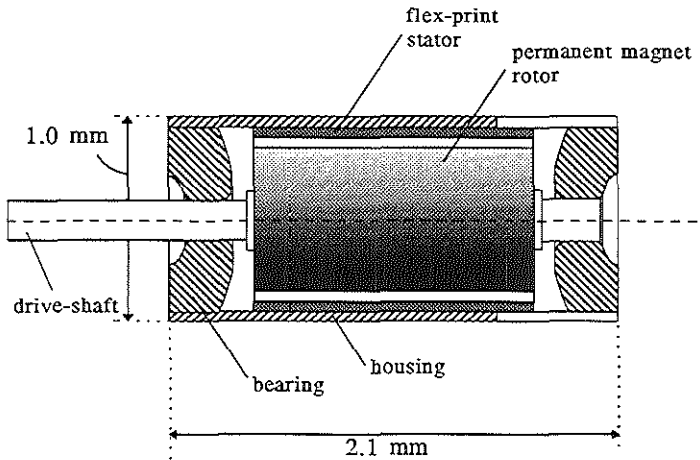


Fig. 3.2-3 Electro-magnetic synchronous micro-motor of 1 mm OD and 2.1 mm length, with flex-print stator [11].

Based on energy flow scheme B1:

String pulley

A linear motion can be transmitted through the catheter in the form of the translation of a thin string. This motion is transformed in the catheter-tip by leading the string over a friction wheel, which drives a shaft with the acoustic mirror (Fig. 3.2-4).

A fixed relationship between linear string travel and tip-rotation angle is required in order to derive the angular position of the US-beam accurately from the string translation. Slip over the friction wheel is therefore intolerable. Variations in strain of the string, as well

as small changes in length of the catheter-tube cause catheter-tip scan-rotation errors. The sensitivity to these problems depends on choices of dimensions and materials. In Appendix A it is shown that this approach is not as obvious as it may seem. A calculation example illustrates the problems to be solved when pursuing this concept.

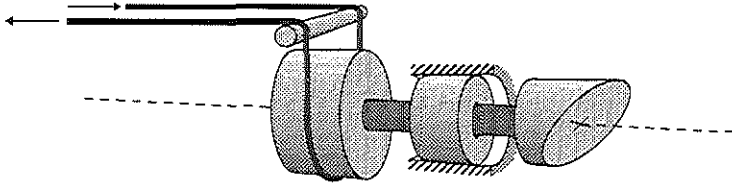


Fig. 3.2-4 Concept of string pulley for catheter-tip rotation.

Hydraulic linear motor with translation-rotation transformation

A cylinder-piston configuration in the catheter-tip establishes a linear motion which can be transformed into rotation using a screw, similar to the electro-magnetic linear motor, described earlier [3, p. 60]. The same arguments apply to the screw-form-plate construction in this case. The catheter acts as hydraulic tube, through which a fluid flow is transmitted from the proximal catheter side to the tip. The motion of the fluid column requires a buffer function of fluid, distal to the cylinder-piston configuration in the tip, or the presence of a return lumen.

Also for acoustic reasons a fluid has to be present in the tip of the catheter.

Hydraulic spiral-groove motor and micro-turbine

In these concepts a fluid flow through the catheter generates the rotation of a spiral-groove motor [3, p. 34] or a micro-turbine [3, p. 39], which drives the acoustic mirror. The rotation of the spiral-groove motor is based on shear stress between the fluid-flow and the spiral-groove rotor. The turbine obtains rotational energy by a transfer of impulse from the fluid-flow to the turbine rotor-blades.

Proximal pressure and fluid flow can be monitored and should accurately determine the rotation angle of the motor or turbine.

For a larger scale application in an ultrasonic endoscope, a similar driving system is proposed by Yoshimoto [12].

Calculations performed by Korbijn [3, p. 31-39], based on realistic catheter dimensions and applying water as the driving fluid show for the spiral-groove motor, that the maximum torque $T_{\max} = 2.8 \mu\text{Nm}$ may achieve rotation at the catheter-tip, if very low axial friction in the motor can be established. But the stiffness of the motor determining the sensitivity of the angular velocity $\Delta\omega$ to changes in torque ΔT is very low: $\Delta\omega/\Delta T = 3300 \text{ rad/s} \cdot \mu\text{Nm}$. In order to meet the specification of eq. 3-6, the torque should be constant within 0.003 % of its maximum value. This does not seem to be realistic. Furthermore the relatively low tip-rotary speed of 1000-3000 rpm and the relatively high required torque will make the motor perform at 1 to 3 % of its maximum rotation speed and close to its maximum torque. In this situation, small disturbances in the torque will cause the motor to stop. A reduction of the rotation speed by means of a gearing, will improve the performance, but will also complicate the catheter-tip construction.

For the turbine Korbijn [3, p. 39-43] derives a stiffness $\Delta\omega/\Delta T = 9300 \text{ rad/s} \cdot \mu\text{Nm}$. So that the load torque should be kept constant within 0.03 % of its maximum value $T_{\max} = 0.12 \mu\text{Nm}$. The practical rotary speed of 1000-3000 rpm is 5-15 % of the maximum speed of the turbine. The maximum torque is probably not enough to overcome friction forces in the process of driving an acoustic mirror.

Both systems should preferably have a return-flow lumen. An alternative, though unattractive, is an outlet into the blood-stream. In the latter case the fluid should not be contaminated with material extracts or particles. The total quantity of fluid released is for the spiral-groove motor about $30 \text{ cm}^3/\text{h}$ and for the micro-turbine more than $500 \text{ cm}^3/\text{h}$.

Because of their inherent characteristics, these concepts do not look promising and therefore have not been pursued.

Based on energy flow scheme B2:

Flexible drive-shaft rotation transmission

The direct transmission of a rotational motion from a driving motor through the catheter to the catheter-tip is possible using a flexible drive-shaft. This way an energy- or motion transformation in the tip of the catheter can be avoided, but the flex-shaft has to meet some seemingly contradicting specifications.

The shaft runs through the whole length of the catheter and adds to its over-all bending rigidity. Flexibility of the catheter is mandatory in order to follow the tortuous blood-vessels, so that also the drive-shaft should be flexible. For coronary use the bending rigidity of the catheter is in the order of 30 Nmm^2 . The small diameter of the catheter

limits the diameter of the drive-shaft to less than 1 mm. The need for a rotation transmission with a high degree of angular fidelity calls for low friction, rotation symmetrical properties of the drive-shaft, low bending rigidity and high torsional rigidity. Special theoretical modelling as well as practical measurements have been performed to investigate the relationships between all parameters determining the catheter-tip running behaviour in this case (see Chapter 4). From these data it can be derived which catheter and drive-shaft properties guarantee an adequate rotation transmission under certain geometrical conditions.

For drive-shafts with elastic bending and torsional behaviour it is shown that reduction of the ratio bending rigidity/torsional rigidity (EI/S_t) improves the angular fidelity.

Several flexible drive-shaft designs will now be discussed.

Solid wire or capillary

The simplest flexible drive-shaft is formed by a solid material round wire or a capillary of the same material, if conducting leads have to run through the shaft. By reducing the outer diameter D of the wire, or to some extent by increasing the inner diameter d , the shaft becomes more flexible; the bending rigidity EI diminishes according to [13, p. 135]:

$$EI = \frac{E}{64} \pi (D^4 - d^4) \quad (3-7)$$

where

E [N/mm²] = Young's modulus

I [mm⁴] = moment of inertia of drive-shaft cross-section

However, in this case also the torsional rigidity S_t becomes smaller according to [13, p. 87]:

$$S_t = GI_p = \frac{G}{32} \pi (D^4 - d^4) \quad (3-8)$$

where

G [N/mm²] = shear modulus

I_p [mm⁴] = polar moment of inertia of the round drive-shaft cross-section

The important ratio EI/S_t , which to a large extent determines the quality of the drive-shaft in terms of rotation angle transmission fidelity (see Chapter 4), is given by:

$$\frac{EI}{S_t} = \frac{E}{2G} \quad (3-9)$$

Assuming the use of an isotropic material the Young's modulus E and the shear modulus G are inter-related, with Poisson's ratio ν as independent factor [13, p. 61]:

$$G = \frac{E}{2(1+\nu)} \quad (3-10)$$

so that eqs. 3-9 and 3-10 give:

$$\frac{EI}{S_t} = 1 + \nu \quad (3-11)$$

Because for all possible isotropic materials the value of ν is restricted to $0.25 < \nu < 0.5$, the ratio EI/S_t has a value between 1.25 and 1.5. For stainless steel, where $\nu = 0.32$, $EI/S_t = 1.32$.

According to § 4.1 this value of EI/S_t is very high. Therefore this shaft is sensitive to all influences determining the rotation error angle of a shaft in a curved catheter-tube. Even under moderately curved conditions solid material drive-shafts will not perform well; the catheter has to be kept as straight as possible.

Another reason to keep the catheter straight is the risk for plastic material deformation, which causes pre-curvature and subsequently bad running behaviour (see § 4.1).

Under the assumptions that:

- plastic deformation occurs when locally the effective stress σ exceeds the value of $\sigma_{0.2}^{(1)}$,
 - and for $\sigma < \sigma_{0.2}$ the material shows a linear elastic behaviour,
- the minimum radius of curvature causing no significant plastic deformation is given by:

$$\rho_{\min} = \frac{ED}{2\sigma_{0.2}} \quad (3-12)$$

For small diameter stainless steel wire, where $E = 200,000 \text{ N/mm}^2$ and $\sigma_{0.2} = 600 \text{ N/mm}^2$ ⁽²⁾ and a shaft diameter $D = 0.5 \text{ mm}$, the value for $\rho_{\min} = 83 \text{ mm}$.

Furthermore drive-shaft break-down of a too strongly curved section may occur, caused by material fatigue, when rotating the shaft (at high speed) for some time in the same

⁽¹⁾This is a material constant, representing the tensile stress which causes 0.2 % of the accompanying strain to be irreversible.

⁽²⁾This value is higher than the value for bulk-material. For small diameter cold-deformed wire these values may differ significantly from values for bulk material, because of the occurrence of texture.

position.

For stainless steel the maximum periodic tension that will not cause failure by fatigue does not differ much from $\sigma_{0.2}$; the minimum safe radius of curvature is therefore also about 83 mm.

For coronary applications, where the over-all catheter bending rigidity should not exceed 30 Nmm^2 , the diameter of the drive-shaft, being a solid stainless steel wire, should be smaller than 0.2 mm, also allowing for a catheter-tube of the same stiffness. The minimum radius of curvature of 15 mm, occurring in the coronary application, requires a shaft with a diameter of even less than 0.1 mm, to prevent plastic deformation of the shaft. According to eq. 3-11 the ratio EI/S_t does not depend on the wire diameter, so this value remains 1.32. As will be proved in the next chapter, high fidelity rotation transmission cannot be expected, using this wire.

Twisted flat wire

A round wire, with diameter d , can be made more flexible by applying many (equidistant) cuts, along the length of the wire, perpendicular to the centre-line and with a depth $< d/2$. If the wire is cut in from both sides, a "string of beads" is created, connected by short bridges of "flat wire". A constant bending rigidity "on macro-scale" in all planes can be achieved by rotating the wire after every cut, over a certain angle with respect to the cutting direction.

The aim of all this should not only be a decrease of bending stiffness of the shaft; for that a round wire with smaller diameter would apply. Also the over-all ratio EI/S_t should decrease. The "beads" of round wire do not serve any purpose in this respect, so they can be left out. What remains are sections of "flat wire", where one section is rotated over a certain angle, around the centre-line, with respect to the preceding section. The continuous analogue of this, where the section-length becomes very small, as does the angle increment, is a twisted flat wire.

A wire with rectangular cross-section, with height h and width b has bending rigidities EI_y and EI_z , when bending around its principal axes \bar{y} and \bar{z} (Fig. 3.2-5):

$$EI_{\bar{y}} = \frac{Ebh^3}{12} \quad \text{and} \quad EI_{\bar{z}} = \frac{Ehb^3}{12} \quad (3-13)$$

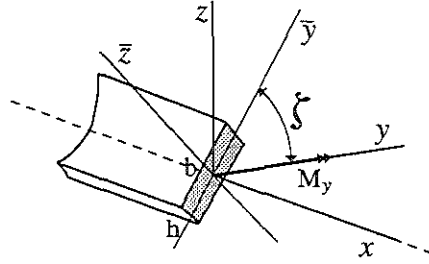


Fig. 3.2-5 Cross-section of a flat wire with principal axes \bar{y} and \bar{z} , and a bending moment M_y

Assuming that the catheter-tube is curved around the y -axis, the drive-shaft undergoes a bending moment M_y , causing the curvatures κ_y and κ_z :

$$\kappa_{\bar{y}} = -\frac{M_y \sin \zeta}{EI_{\bar{z}}} \quad \text{and} \quad \kappa_{\bar{z}} = -\frac{M_y \cos \zeta}{EI_{\bar{y}}} \quad (3-14)$$

The curvature in the xz -plane is κ_z :

$$\kappa_z = \kappa_{\bar{z}} \cos \zeta + \kappa_{\bar{y}} \sin \zeta = -M_y \left(\frac{\cos^2 \zeta}{EI_{\bar{y}}} + \frac{\sin^2 \zeta}{EI_{\bar{z}}} \right) \quad (3-15)$$

The wire is twisted into a helical shape (Fig. 3.2-6), so that ζ changes with the coordinate x . If $d\zeta/dx$ is constant and large enough, the bending rigidity on "macro-scale" is not dependent on the plane of curvature and the effective bending rigidity EI_{eff} can be found from:

$$\frac{1}{EI_{\text{eff}}} = \frac{1}{\pi} \int_0^\pi -\frac{\kappa_z}{M_y} d\zeta = \frac{EI_{\bar{y}} + EI_{\bar{z}}}{2 EI_{\bar{y}} EI_{\bar{z}}} \quad (3-16)$$

For $h \ll b$, EI_{eff} is given by:

$$EI_{\text{eff}} = \frac{2 EI_{\bar{y}} EI_{\bar{z}}}{EI_{\bar{y}} + EI_{\bar{z}}} \approx 2EI_{\bar{y}} = \frac{Ebh^3}{6} \quad (3-17)$$

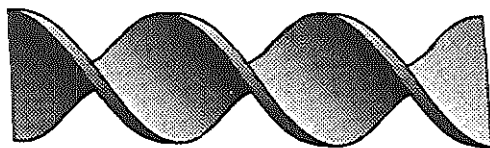


Fig. 3.2-6 Twisted flat wire.

Independent from the angular position of the cross-section, the torsional rigidity of the wire is [14]:

$$S_t = \frac{Gbh^3}{3} \quad (3-18)$$

The ratio EI_{eff}/S_t is:

$$\frac{EI_{eff}}{S_t} = \frac{E}{2G} = 1 + \nu \quad (3-19)$$

where ν = Poisson's ratio.

Intuitively this concept seems to have some potential for improvement of the ratio bending rigidity/torsional rigidity, over the simple round wire. However, analysis eradicates the option (compare eqs. 3-11 and 3-19).

String of beads

A string of beads can represent a flexible but torsionally rigid structure (Fig. 3.2-7) [15]. The difficulty of this concept lies in the need for equally easy bending in all bending planes, which calls for a special design of the joints (a simple ball-joint also permits axial rotation). A recurrent unit of a sequence of one-plane deflection joints with relatively rotated deflection planes may function properly, but these units are relatively stiff, when bent in one plane. The very small practical radii of curvature (down to 15 mm) and the small clearance of the shaft in the catheter-tube require a short length of the elements (< 6 mm). If the angle between the bending planes of two succeeding joints is 30° , then the maximum length of bead is about 1 mm.

Another drawback is the rotational play, unavoidably present in every joint and cumulatively present in the definition of the tip-rotation. Under the assumption that the driving torque always points in the same direction, the cumulative rotation play between the elements will result in a maximum constant drag of the tip, after which it will not

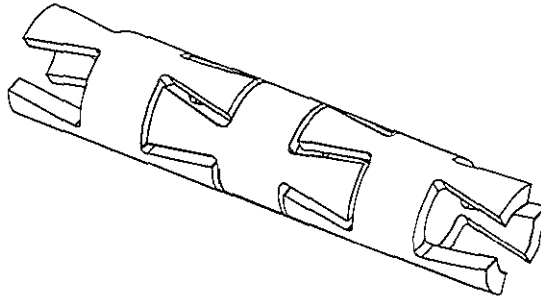


Fig. 3.2-7 String of beads as a concept of a flexible drive-shaft [15].

effect the tip-rotation any more.

The beads and joints should have rounded surfaces. Sharp edges will cause massive wear of the polymer catheter-tube.

Spiral type drive-shaft

A popular design of the flexible drive-shaft is based on the concept of several layers of alternately helically wound steel wire. This concept is known from literature [16], though mostly for applications with larger diameter (> 3 mm). These spiral-type flexible drive-shafts consist of several layers of multi-filament spirals, where two succeeding layers are wound in opposite directions (Fig. 3.2-8a). Essential to good performance of the shaft is the absence of radial space between the spiral layers. The good rotation-transmission characteristics of this shaft, expressed by a low ratio EI/S_t , can be explained by the fact that a torque applied to the shaft in one direction will tend to increase the diameter of one set of spiral layers, while the layers in between, which are counter-wound, tend to decrease their diameter. Both effects partly eliminate each other. The torque is directed largely into pure tensile and compressive stresses in the spiral filaments. This results in a small torque angle of the entire drive-shaft assembly, so that the torsional rigidity is much higher than the sum of the torsional rigidities of all spirals separately. In the bending mode the spirals act more independently, so that the bending rigidity is about equal to the sum of the bending rigidities of all spirals separately. The best result is obtained when the driving direction of the shaft induces diameter reduction in the outer layer of spiral filaments.

The small space available in the catheter application limits the construction of the drive-shaft to only two spiral layers (Fig. 3.2-8b) [17]. In case of enough interference, i.e. radial pre-tension between the two layers and low driving torque, the driving direction will not interfere with the drive-shaft characteristics and rotation transmission fidelity may be

expected to be the same for both driving directions.

The ratio EL/S_t for a spiral-type drive-shaft of small dimensions ($OD < 1 \text{ mm}$) has shown to be less than 0.015.

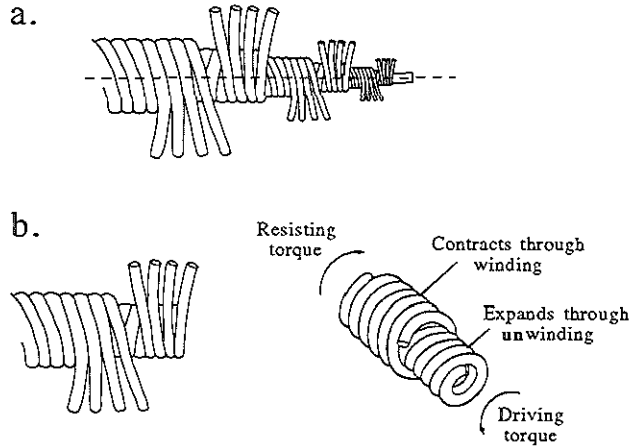


Fig. 3.2-8 Spiral type drive-shaft with counter-wound layers of multi-filament spirals. Multi-layer configuration (a), two-layer configuration (b) [17].

A constant error angle in the order of 10° has shown to be possible in normal clinical application. Also a periodic error angle $< 20^\circ$ peak-to-peak is feasible. A stochastic error angle $< 1^\circ$ implies that the stochastic variation of the torque is less than 10 % of the constant torque and also less than 10 % of the amplitude of the periodic variation of the torque. These demands seem reasonable and can be met. Consequently the requirements, set in § 3.1 can be met by this flexible drive-shaft.

In the next chapter the rotation angle transmitting properties of flexible drive-shafts in a curved enclosing tube will be further investigated.

References

1. Hoff H. ten, Korbijn A., Smit Th.H., Klinkhamer J.F.F., Bom N., Imaging artifacts in mechanically driven ultrasound catheters, *Int. J. Cardiac Imag.* 4: 195-199, 1989.
2. Li W., Gussenhoven W.J., Zhong Y., The S.H.K., Di Mario C., Madretsma S., Egmond F. van, Feyter P. de, Urk H. van, Rijsterborgh H., Bom N., Validation of quantitative analysis of intravascular ultrasound images, *Int. J. Cardiac Imag.* 6: 247-253, 1991.
3. Korbijn A., Onderzoek naar alternatieve aandrijvingen voor een echo-imaging catheter, MSc. Thesis, Technical University Delft, Department of Mechanical Engineering, Section Precision Engineering, Report # A-489/K14, October, 1989.
4. Bollée B., Elektrostatische motoren, *Philips Technisch Tijdschrift*, 6/7: 183-199, 1969.
5. Fujimoto A., Sakata M., Hirano M., Goto H., Miniature electrostatic motor, *Sensors and Actuators A*, 24: 43-46, 1990.
6. Bart S.F., Lober Th. A., Howe R.T., Lang J.H., Schlecht M.F., Design considerations for micromachined electric actuators, *Sensors and Actuators*, 14: 269-292, 1988.
7. Hippel A.R. von, Molecular science and molecular engineering, The Technology Press of M.I.T. and John Wiley & Sons, Inc., New York, pp. 44-48, 1959.
8. Leeuwis H., Woerkens E van, Voorwoord *Micromechanica*, *Micro Select* 16, September 1989.
9. Frazier B., Babb J.W., Allen M.G., Taylor D.G., Design and fabrication of electroplated micromotor structures, DSC-Vol. 32, *Micromechanical Sensors, Actuators, and Systems ASME* 1991, pp. 135-146.
10. Hadfield P., Tiny motor clears way for microsurgery, *New Scientist*, p. 19, October 10, 1992.
11. Lancée C.T., Bom N., Ultrasonic instrument with a micro-motor having stator coils on a flexible circuit board, US patent application No. 07/820,571, January 14, 1992, New CIP 2 application of US patent application No. 07/591,652, October 2, 1990.
12. Yoshimoto Y., Ultrasonic observation endoscope, Japanese patent # 60-169760, 1985.
13. Timoshenko S.P., Gere J.M., *Mechanics of materials*, Van Nostrand Reinhold Company, New York, Converted version into S.I. units, 1973.
14. Timoshenko S.P., Goodier J.N., *Theory of elasticity*, 3rd edition, Mc Graw-Hill Int. Book Company, Tokyo, p. 307, 1970.
15. Klinkhamer J.F.F., Flexibele torsie-as, Idee-beschrijving, Internal memo Productcentre TNO, Delft, The Netherlands.
16. Niemann G., *Maschinen-elemente*, Band I, Springer-Verlag Berlin, Heidelberg, New York, p. 356, 1981.
17. Martín R.W., Johnson C.C., Design characteristics for intravascular ultrasound catheters, *Int. J. Cardiac Imag.* 4: 201-216, 1989.

CHAPTER 4 Flexible drive-shaft rotation transmission

Introduction

In the previous chapter several ways of catheter-tip rotation have been presented, including the application of a flexible drive-shaft to transmit the rotational motion from a proximal driving motor to the catheter-tip. Also the need for uniform tip-rotation has been demonstrated, in order to obtain reliable images with a minimum of image distortion. In this chapter the behaviour of the flexible shaft driving system will be discussed in terms of angle transmission fidelity. § 4.1 describes the analytical modelling of the rotational behaviour of a flexible drive-shaft in a curved tube and reveals some important catheter design parameters as well as properties of the drive-shaft to optimize running behaviour. In § 4.2 and § 4.3 these findings are verified by respectively numerical calculations, based on the finite element method (FEM) and some relevant measurement results. Conclusions concerning the validity of modelling and measurements as well as design specifications for flexible drive-shafts with high fidelity rotation angle transmission can be found in § 4.4.

Symbols

Drive-shaft parameters:

EI	$[Nmm^2]$	flexural rigidity ⁽¹⁾
EI_y	$[Nmm^2]$	flexural rigidity while bending around the principal axis \bar{y} ⁽¹⁾
EI_z	$[Nmm^2]$	flexural rigidity while bending around the principal axis \bar{z} ⁽¹⁾
\bar{EI}	$[Nmm^2]$	average flexural rigidity = $(EI_y + EI_z)/2$
p	--	= $(EI_y - EI_z)/(EI_y + EI_z)$
I_y	$[mm^4]$	moment of inertia of the cross-sectional area, while bending around the principal axis \bar{y}
I_z	$[mm^4]$	moment of inertia of the cross-sectional area, while bending around the principal axis \bar{z}
E	$[N/mm^2]$	Young's modulus of the drive-shaft material
EI_y	$[Nmm^2]$	flexural rigidity while bending around the y-axis ⁽¹⁾
EI_z	$[Nmm^2]$	flexural rigidity while bending around the z-axis ⁽¹⁾
S_t	$[Nmm^2]$	torsional rigidity
GI_p	$[Nmm^2]$	torsional rigidity of a drive-shaft with circular cross-section ⁽¹⁾
G	$[N/mm^2]$	shear modulus of the drive-shaft material
I_p	$[mm^4]$	polar moment of inertia of drive-shaft with round cross-section
m/L	$[g/mm]$	mass of a drive-shaft per unit length
J_i	$[kgm^2/m]$	moment of inertia per unit length with respect to the central axis
EA	$[N]$	axial stiffness ⁽¹⁾

Geometric parameters:

x	$[mm]$	x-coordinate of Cartesian coordinate system
y	$[mm]$	y-coordinate of Cartesian coordinate system
z	$[mm]$	z-coordinate of Cartesian coordinate system
\bar{y}	$[mm]$	coordinate along the principal axis of bending \bar{y}
\bar{z}	$[mm]$	coordinate along the principal axis of bending \bar{z}
s	$[mm]$	coordinate along the curved section of the drive-shaft
D	$[mm]$	catheter-tube inner diameter (ID)
d	$[mm]$	drive-shaft outer diameter (OD)
c	$[mm]$	clearance of a drive-shaft in a catheter-tube: $c = D - d$
A	$[mm^2]$	cross-sectional area of a drive-shaft
l	$[mm]$	length of defined section of a drive-shaft
l_1	$[mm]$	straight length of a drive-shaft
L	$[mm]$	total length of a drive-shaft
s_1	$[mm]$	curved length of shaft
φ	$[rad]$	rotation angle of bending
φ_1	$[rad]$	rotation angle of bending in the simple model geometry
$\psi_1 = \psi_{prox}$	$[rad]$	proximal (driving) rotation angle of drive-shaft
ψ_2	$[rad]$	rotation angle of the drive-shaft at the transition between straight and curved section

⁽¹⁾Only for a solid material drive-shaft, made of isotropic material, the value of this quantity is equal to the product of the quantities as given. In other cases however, it is an effective quantity.

$\psi_3 = \psi_{\text{dist}}$	[rad]	distal rotation angle of drive-shaft
ρ	[mm]	radius of curvature
ρ_0	[mm]	radius of curvature of drive-shaft pre-curvature
ρ_1	[mm]	radius of curvature of the centre-line of the catheter-tube
κ_0	[mm ⁻¹]	pre-curvature of drive-shaft: $\kappa_0 = 1/\rho_0$
κ_1	[mm ⁻¹]	curvature of the centre-line of the catheter-tube: $\kappa_1 = 1/\rho_1$
κ_y	[mm ⁻¹]	drive-shaft curvature in y-direction
κ_z	[mm ⁻¹]	drive-shaft curvature in z-direction
$\kappa_{\bar{y}}$	[mm ⁻¹]	drive-shaft curvature in \bar{y} -direction
$\kappa_{\bar{z}}$	[mm ⁻¹]	drive-shaft curvature in \bar{z} -direction
β	[rad]	angle of non-contact in which the drive-shaft crosses from the inside bend to the outside bend (Fig. C-4)
η	[rad]	torsion angle over the drive-shaft
χ	[rad/mm]	specific torsion angle: $\chi = d\eta/ds$
θ	[rad]	rotation error angle over the drive-shaft: $\theta = -\eta$
θ_{l_1}	[rad]	rotation error angle over straight length of shaft l_1
θ_{s_1}	[rad]	rotation error angle over curved shaft section s_1
θ_{p-p}	[rad]	peak-to-peak value of the periodic rotation error angle: $\theta_{p-p} = 2 \times \text{amplitude}$
θ_G	[rad]	rotation error angle due to friction, caused by gravitation
γ	[°]	rotation error angle over the drive-shaft
γ_{p-p}	[°]	peak-to-peak value of periodic rotation error angle
γ_G	[°]	rotation error angle due to friction, caused by gravitation
γ_{fr}	[°]	rotation error angle due to friction, caused by curvature

Forces and power:

W	[Nmm]	work performed on (a section of) a drive-shaft
W_{str}	[Nmm]	strain energy of a curved and torqued drive-shaft (section)
W_b	[Nmm]	strain energy of a curved drive-shaft (section)
W_t	[Nmm]	strain energy of a torqued drive-shaft (section)
W_f	[Nmm]	work performed to serve a (friction) load
T	[Nmm]	(driving) torque
T_{EI}	[Nmm]	driving torque due to $EI_y \neq EI_z$
T_{ρ_0}	[Nmm]	driving torque due to pre-curvature
T_{fr}	[Nmm]	driving torque due to friction
T_G	[Nmm]	driving torque due to gravitation
M_t	[Nmm]	torque in the drive-shaft
M	[Nmm]	drive-shaft bending moment
M_y	[Nmm]	drive-shaft bending moment around the y-axis
M_z	[Nmm]	drive-shaft bending moment around the z-axis
$M_{\bar{y}}$	[Nmm]	drive-shaft bending moment around the principal axis \bar{y}
$M_{\bar{z}}$	[Nmm]	drive-shaft bending moment around the principal axis \bar{z}
F	[N]	force
F_n	[N]	lateral force of catheter inner wall on drive-shaft
F_w	[N]	force of friction

Miscellaneous:

μ	--	friction coefficient
ω	[rad/s]	angular velocity of the driven proximal side of the drive-shaft
ω_0	[rad/s]	fundamental radial frequency of a (section of a) drive-shaft, vibrating in torsional mode
t	[s]	time
A	[rad]	amplitude of periodic error angle due to $EI_y \neq EI_z$
B	[rad]	amplitude of periodic error angle due to pre-curvature
g	[m/s ²]	acceleration due to gravitation (= 9.8 m/s ²)

§ 4.1 Analytical modelling

The parameters ruling flex-shaft rotation angle transmission in a curved (catheter-) tube have been investigated. After recognizing the important parameters, their influence on the rotation angle transmission is determined analytically for simple geometries.

Ruling parameters

Many different parameters influence the error angle of the tip-rotation as defined in Chapter 3, eq. 3-1; the following eight influences will be considered:

1. Unequal flexural rigidities in different bending planes: $EI_y \neq EI_z$

The flexural rigidity of the drive-shaft EI may differ according to the plane in which the shaft is bent. For instance a stainless steel (SS) capillary drive-shaft with an eccentric lumen or an oval cross-section has this property. If such a drive-shaft is rotated, while being curved, the strain energy of the shaft changes in accordance with the changing bending rigidity. A varying torque is the result, causing a varying torsion angle. In the manufacturing process a tight tolerance should be held on the roundness of the shaft. A slightly elliptic cross-section with axes, deviating $\pm 1\%$ from a nominal diameter, causes a difference in bending rigidity, while bending around the two principal axes, of 4% of the nominal bending rigidity [1]. The parameter p , defined in eq. 4-4, is 0.02. Under circumstances to be discussed later, the effect of this can be significant.

2. Pre-curvature: radius of curvature $\rho = \rho_0$

In case no forces (also no gravitational forces) are applied to a drive-shaft with elastic bending behaviour, the shaft should be straight. If this is not entirely the case a pre-curvature with radius ρ_0 is present. If such a drive-shaft is rotated, situated in a curved tube, the strain energy of the shaft changes according to the angle between the plane of pre-curvature of the shaft and the plane of curvature of the tube. A varying torque is the result, causing a varying torsion angle.

The production process should yield straight drive-shafts. Otherwise a complementary straightening treatment is necessary. Pre-curvature will occur if the shaft material undergoes "cold flow", being in a coiled position under shipping and storage conditions. Excessive deformation during usage, like accidental kinking, will also cause pre-curvature.

3. Lateral forces F_n induce friction F_w which causes a torque T_{fr} :

$$T_{fr} = F_w \frac{d}{2} = \mu F_n \frac{d}{2} \quad (4-1)$$

In order to bend the drive-shaft in accordance with the curvature of the (catheter-) tube, the presence of external forces is necessary. These external forces are lateral forces of interaction between the inside wall of the tube and the drive-shaft. Given a certain friction coefficient μ between these two bodies, tangential friction forces will occur, while rotating the drive-shaft. Multiplication of these forces by half the drive-shaft diameter renders the driving torque (due to friction, in every drive-shaft cross-section proximal to the friction force). The torque causes a torsion angle over the drive-shaft (segment proximal to the friction force). The summation of these torsion angles due to all friction forces present (in case of only friction) is equal to minus the error angle of the tip-rotation.

4. The friction coefficient may be dependent on velocity: $\mu = \mu(v)$

The situation described in the previous point at issue (3) presumes a constant friction coefficient μ under all circumstances. However, the friction coefficient may be dependent on the relative velocity of the two surfaces concerned. In the simplest model the cases of static and dynamic friction can be distinguished, with a larger friction coefficient in the static situation, which may cause the stick-slip phenomenon. Furthermore the friction can be influenced by any lubricating fluid present.

This chapter will not present a model for stick-slip, because it will be shown that good catheter and drive-shaft design ensures continuous, although possibly fluctuating, tip-motion. The tip of the drive-shaft may only come to a full stop, if a large extra external (friction) load is applied to the (tip of the) drive-shaft.

5. Loss of energy in the bending shaft: damping and internal friction

The bending behaviour of the drive-shaft is never entirely elastic. Some energy will be lost by the damping and internal friction of the material, as is the case for a stainless steel capillary drive-shaft, or in the construction of the shaft, as is the case for the double-layer spiral drive-shafts. Here the coils will slightly slide over each other causing friction losses. Rotation of a drive-shaft under curved conditions causes an alternating extension and compression of the "axial fibers" of the shaft resulting in a constant over-all energy conversion into heat. This energy has to be supplied by the existent driving torque, which causes a torsion angle over the shaft.

6. Inertia of moving parts and fundamental frequency

If a static equilibrium is not maintained, the system will obey dynamic laws involving the moment of inertia of the rotating masses around their central axes. Here the drive-shaft itself and mounted transducer-head should be regarded. When rapid changes of velocity

occur, the influence of inertia may also have to be taken into account.

In specific cases, combining the elastic torsional rigidity, inertia, free rotating length and driving rotation frequency, the amplitude of the error angle may increase by resonance. An investigation concerning the fundamental frequencies of the system has been conducted.

7. Gravitation.

Supporting forces on the drive-shaft are applied by the catheter-tube not only to overcome elastic forces of the drive-shaft, but also its weight on the supporting surface contributes to the shaft-wall interaction. The mass of the drive-shaft is very small, so that in most cases this reason for the presence of lateral forces, causing friction (see point 3 of this paragraph) can be neglected.

8. Movement of the catheter tube (in moving vessels).

This phenomenon will not be analysed in depth here.

In reality these influences on the rotation error angle all work together, (partly) compensating or amplifying each other's effect on the tip rotation. As an indication of the importance of each influence, they will first be analysed separately: while one is being investigated, the other's effect is assumed to be zero. Subsequently some combinations will be discussed.

Unequal bending rigidities in different bending planes; $EI_y \neq EI_z$

The analytical modelling of this influence is based on the fluctuation of the strain energy content of the flex-shaft during rotation and is performed for a simple flex-shaft geometry (Fig. 4.1-1)

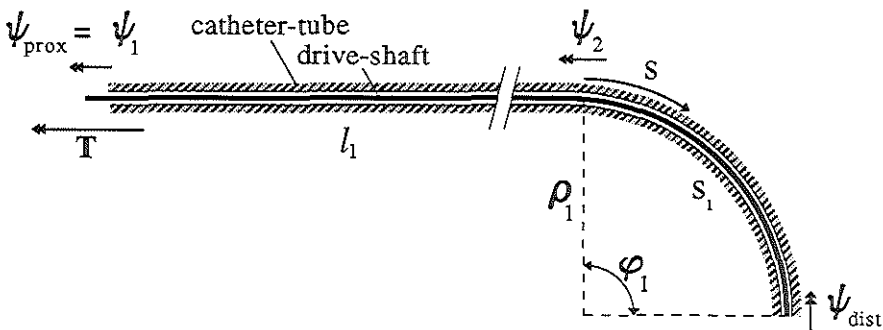


Fig. 4.1-1 Catheter drive-shaft with one simple curve at the tip.

A catheter-tube with a drive-shaft inside is curved in the following way:

- A proximal part l_1 is kept straight and
- a distal part s_1 is curved with $\rho = \rho_1$ over an angle $\phi = \phi_1$ by a bending moment M on the drive-shaft.
- The coordinate along the curved section of the shaft, in the direction of the tip, is s .
- The shaft is assumed to have a linear elastic behaviour. Plastic deformation of the shaft will only superficially be dealt with in this chapter, neither will fatigue be investigated thoroughly. Therefore some of the given numerical examples may be of no practical value, because of drive-shaft failure due to these causes.

The step-by-step analysis is described in Appendix B for two models: a first approximation model and an improved model.

First approximation model

If $l_1 \gg s_1$ (Fig. 4.1-1), the error angle $\theta = \psi_{\text{dist}} - \psi_{\text{prox}}$ is approximated by $\theta = \psi_2 - \psi_1$, where ψ_1 is the proximal rotation angle and ψ_2 is the rotation angle at the transition between the straight and curved section of the drive-shaft.

This way the torsion angle over the curved section of the shaft is thought to be zero (the torsional rigidity $S_t = \infty$), so that the rotation angle ψ is thought to be ψ_2 over the whole curved section.

In this case the rotation error angle θ [rad] over the shaft, which equals minus the torsion angle η , is given by:

$$\theta \approx -A \sin(2(\omega t + \theta)) \quad (4-2)$$

where

$$A = \frac{s_1 l_1 p \overline{EI}}{\rho_1^2 S_t} \quad [\text{rad}] \quad (4-3)$$

and

$$\overline{EI} = \frac{(EI_{\bar{y}} + EI_{\bar{z}})}{2}, \quad p = \frac{(EI_{\bar{z}} - EI_{\bar{y}})}{(EI_{\bar{y}} + EI_{\bar{z}})} \quad (4-4)$$

$EI_{\bar{y}}$ [Nmm²] = flexural rigidity while bending around the principal axis \bar{y} (Fig. B-1)

$EI_{\bar{z}}$ [Nmm²] = flexural rigidity while bending around the principal axis \bar{z} (Fig. B-1)

S_t [Nmm²] = torsional rigidity

ω [rad/s] = angular velocity of the driven proximal side of the drive-shaft

t [s] = time

and p is small for a good quality drive-shaft.

For a drive-shaft curve angle $\varphi_1 = \pi/2$:

$$A = \frac{\pi l_1 p \overline{EI}}{2 \rho_1 S_t} \quad (4-5)$$

Eq. 4-2 describes the rotation error angle θ as a periodic function with twice the frequency of the driving rotation and a variable phase-shift, in relation to a pure sine function, which equals the value of the function itself. The amplitude of the rotation error angle is A , which depends on geometrical parameters and drive-shaft characteristics.

The rotation error angle θ is given in radians. For the sake of easier comprehension, the error angles in most figures will be expressed in degrees. Therefore the rotation error angle γ [degrees] is introduced so that:

$$\gamma = \frac{180}{\pi} \theta \quad (4-6)$$

Fig. 4.1-2a shows the error angle γ as a function of ωt for different values of $A \leq 0.5$.

Eq. 4-2 only gives a valid prediction of the rotation error angle throughout the whole rotation cycle, if $A \leq 0.5$ (Fig. 4.1-2a). If $A > 0.5$ the model curve will get a more pronounced S-shape, predicting a tip rotation sector corresponding with a driving rotation in reverse direction (Fig. 4.1-2b, $A = 0.75$). This is due to the fact that the analysis is based on static equilibrium, maintained throughout the whole rotation cycle. Reverse driving rotation does not occur in reality. In stead, the static equilibrium will be lost as soon as $d\gamma/dt = \infty$ and the angular position of the tip of the shaft will be determined by the laws of dynamics rather than statics. The low value of the rotating mass enables a fast restoring of static balance of forces by a near-vertical part of the curve, representing the "whip-effect". The curve becomes saw tooth shaped. If this behaviour is incorporated into the model, its validity is extended to values of $A > 0.5$.

The criterion to insure the absence of "whip" due to unequal bending rigidities in different bending planes is:

$$A = \frac{s_1 l_1 p \overline{EI}}{\rho_1^2 S_t} \leq 0.5 \quad (4-7)$$

For $A \leq 0.5$, the peak-to-peak rotation error angle $\theta_{p-p} = \theta_{\max} - \theta_{\min} = 2A$. But if $A > 0.5$, $\theta_{p-p} < 2A$, due to the "short cut" in the curve, representing the "whip-behaviour". In the latter case the minimum value of the rotation error angle $\theta_{\min} = -A$, but the maximum value $\theta_{\max} < +A$. The value of θ_{\max} can be derived from the combination of the model of eq. 4-2 with the "whip-effect". It is determined by the intersection of the vertical "whip-line" with the descending part of the curve described by eq. 4-2.

The peak-to-peak rotation error angle θ_{p-p} can be found this way as a function of A (Fig. 4.1-2c). Considering the fact that the tip-rotation direction is never opposite to the driving direction, the maximum value of θ_{p-p} is π , which is the asymptote in Fig. 4.1-2c. In this case the tip does not rotate at all during most of the driving rotation cycle and catches up twice in a quick "whip-motion" of π radians.

Drive-shaft behaviour like this should be avoided by keeping the factor A low. The amplitude of the error angle γ has been calculated for different drive-shafts, using the drive-shaft characteristics of Table 4.1-1. The drive-shaft geometry has been defined by $l_1 = 1000$ mm, $\phi_1 = \pi/2$, whereas the radius of curvature $\rho_1 = 100$ mm or $\rho_1 = 20$ mm. The results can be seen in Table 4.1-2.

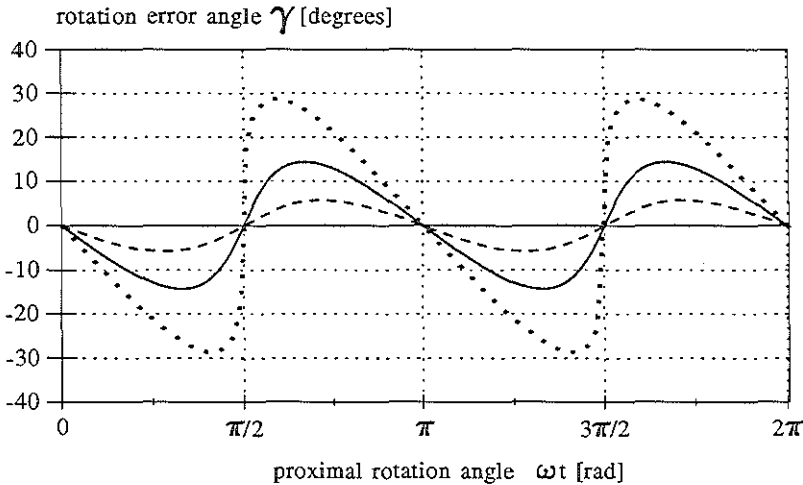


Fig. 4.1-2a Rotation error angle γ [degrees] due to unequal bending rigidities in different bending planes for $A \leq 0.5$: $A = 0.1$ (---); $A = 0.25$ (—); $A = 0.5$ (···).

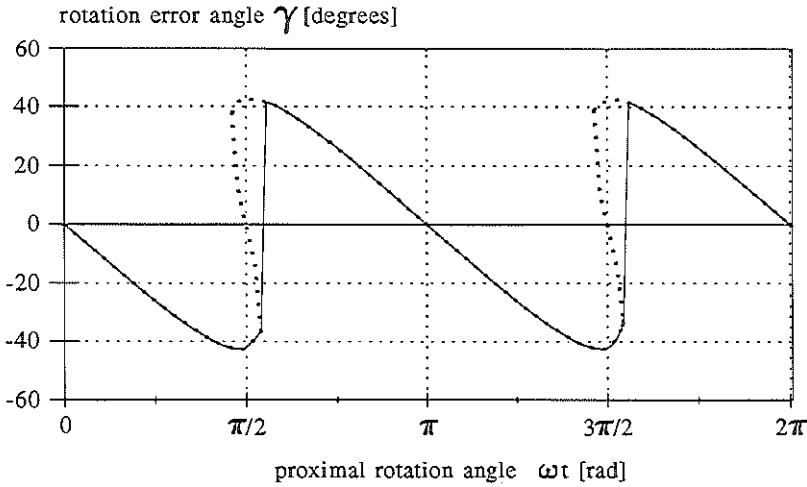


Fig. 4.1-2b Rotation error angle γ [degrees] due to unequal bending rigidities in different bending planes for $A = 0.75$. Analytical model according to eqs. 4-2 and 4-6 (---); realistic curve with "whip-effect" (—).

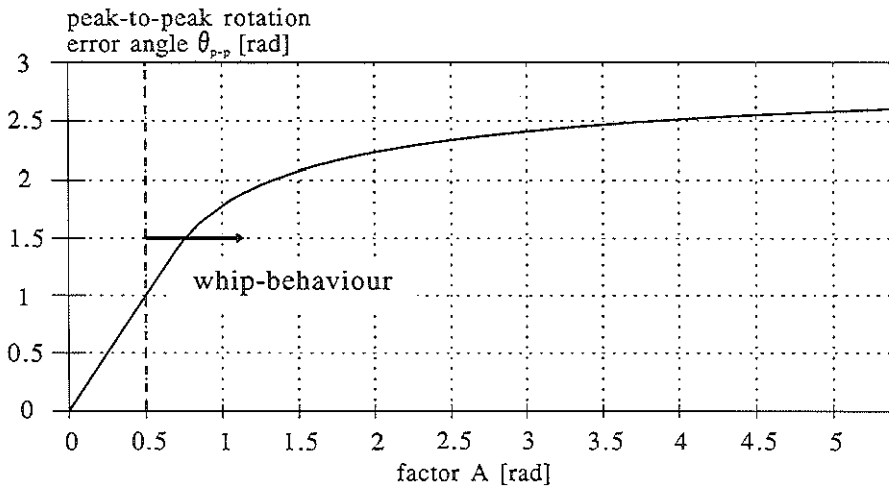


Fig. 4.1-2c Peak-to-peak rotation error angle θ_{p-p} [rad], due to unequal bending rigidities in different bending planes as a function of the factor A.

Table 4.1-1 Specifications of several drive-shafts.

	SS-capillary	flex-shaft with optical fiber	SS double spiral type I	SS double spiral type II
ID [mm]	0.3	--	0.5	0.5
OD [mm]	0.5	0.82	0.84	0.8
EI [Nmm ²]	534	14	8	1.5
S _t [Nmm ²]	368	27	25	100

Table 4.1-2 A-value [rad] and peak-to-peak error angle γ_{p-p} [degrees] per metre straight length, caused by unequal flexural rigidities in different bending planes.

Curve angle $\phi_1 = \pi/2$.

ρ_1 [mm]	s_1 [mm]	p	SS- capillary		flex-shaft with optical fiber		SS double spiral type II	
			A [rad]	γ_{p-p} [°]	A [rad]	γ_{p-p} [°]	A [rad]	γ_{p-p} [°]
100	157	0.01	0.23	26	0.08	9.3	0.0024	0.3
		0.05	1.14	110	0.41	46.7	0.012	1.4
20	31.4	0.01	1.14	110	0.41	46.7	0.012	1.4
		0.05	5.7	150	2.04	130	0.059	6.8

Improved model

If the assumption $l_1 \gg s_1$ is not valid, torsion in the curved section cannot be disregarded in comparison with the torsion in the straight section. In this case the rotation angle ψ of a point on the curved section cannot be approximated by ψ_2 . A better approximation model is described in Appendix B.

The rotation error angle θ_{it} over the straight section is given by:

$$\theta_{it} = -A \sin \left\{ 2\omega t + 2\left(1 + \frac{s_1}{3l_1}\right)\theta_i \right\} \quad (4-8)$$

where A is given by eq. 4-3 and for a drive-shaft curve angle $\phi_1 = \pi/2$, A is given by eq. 4-5.

For the improved fit of this analytical model with the finite element model see Fig. 4.2-2.

The rotation error angle θ over the whole length of the shaft is given by:

$$\theta = -A \left(1 + \frac{s_1}{2l_1}\right) \sin \left\{ 2\omega t + 2\left(1 + \frac{s_1}{3l_1}\right)\theta_{i_1} \right\} \quad (4-9)$$

In comparison with eq. 4-2 the amplitude of the error is larger (a torsion angle over the curved section is added) and the phase-shift predicted by this model is also larger.

If $l_1 \gg s_1$ is applied to the improved model represented by eq. 4-9, it turns into eq. 4-2.

The criterion to ensure the absence of "whip" due to unequal bending rigidities in different bending planes is better represented by:

$$A \left(1 + \frac{s_1}{3l_1}\right) \leq 0.5 \quad (4-10)$$

Drive-shaft pre-curvature

First approximation model

The model is based on the simple drive-shaft geometry, given in Fig. 4.1-1 and again with the assumption that $l_1 \gg s_1$, so that for the curved section $S_t = \infty$ and $\psi = \psi_2$. The bending rigidity is equal in all bending planes, but the section of the shaft situated in the curve with $\rho = \rho_1$ is not straight without load; it has a pre-curvature with $\rho = \rho_0$.

In this situation the rotation error angle θ [rad] over the shaft is (Appendix B):

$$\theta = \psi_{dist} - \psi_{prox} \approx \psi_2 - \psi_1 = -B \sin(\omega t + \theta) \quad (4-11)$$

where

$$B = \frac{s_1 l_1 EI}{\rho_0 \rho_1 S_t} \quad [\text{rad}] \quad (4-12)$$

and for a drive-shaft curve angle $\varphi_1 = \pi/2$:

$$B = \frac{\pi l_1 EI}{2\rho_0 S_t} \quad (4-13)$$

Eq. 4-11 describes the rotation error angle θ as a periodic function with the same frequency as the driving rotation and a variable phase-shift, in relation to a pure sine

function, which equals the value of the function itself (Fig. 4.1-3a). The amplitude of the rotation error angle is B , which depends on geometrical parameters and drive-shaft characteristics.

Similar to the model for $EI_y \neq EI_z$, this formula is only valid as long as static equilibrium is maintained. This can be shown to be the case for:

$$B = \frac{s_1 l_1 EI}{\rho_0 \rho_1 S_1} \leq 1 \quad (4-14)$$

Fig. 4.1-3b, $B = 1.5$, shows a non-existent reverse driving rotation in the model curve. The real curve has a nearly vertical part, where the static equilibrium can no longer be maintained, so this part of the curve is ruled by the laws of dynamics (the "whip-effect"). For values of $B > 1$, the saw tooth shaped curve will get an off-set: the mean value between the extremes will become negative, because the peak-to-peak rotation error angle becomes smaller than $2B$, while the minimum function value remains $-B$ (Fig. 4.1-3c). The maximum value of the peak-to-peak error angle is 2π , which is the asymptote in Fig. 4.1-3c.

The peak-to-peak rotation error angle at the tip γ_{p-p} can be found in Table 4.1-3 for three types of drive-shaft, specified in Table 4.1-1 and three radii of pre-curvature (20, 100 and 1000 mm). The radius of curvature of the catheter is not of any interest, because we defined the curve ϕ_1 to extend over $\pi/2$ (eq. 4-13). The straight length $l_1 = 1000$ mm.

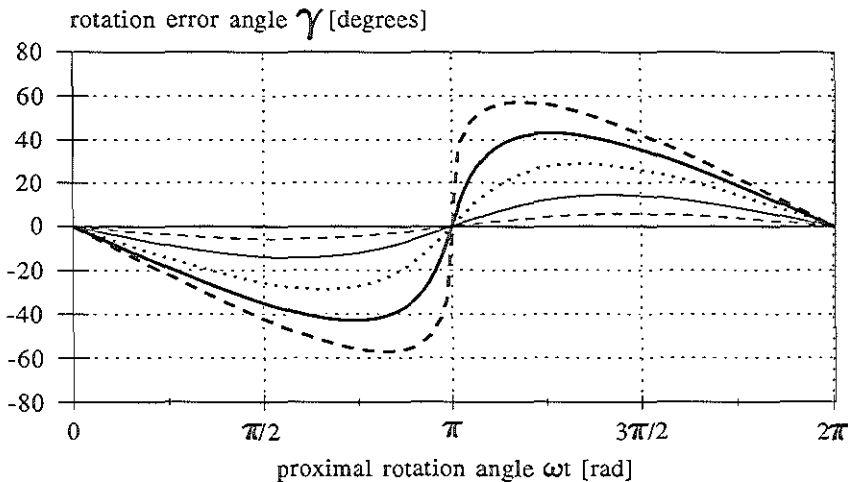


Fig. 4.1-3a Rotation error angle γ [degrees] due to drive-shaft pre-curvature for $B \leq 1$: $B = 0.1$ (---); $B = 0.25$ (—); $B = 0.5$ (···); $B = 0.75$ (—); $B = 1.0$ (—).

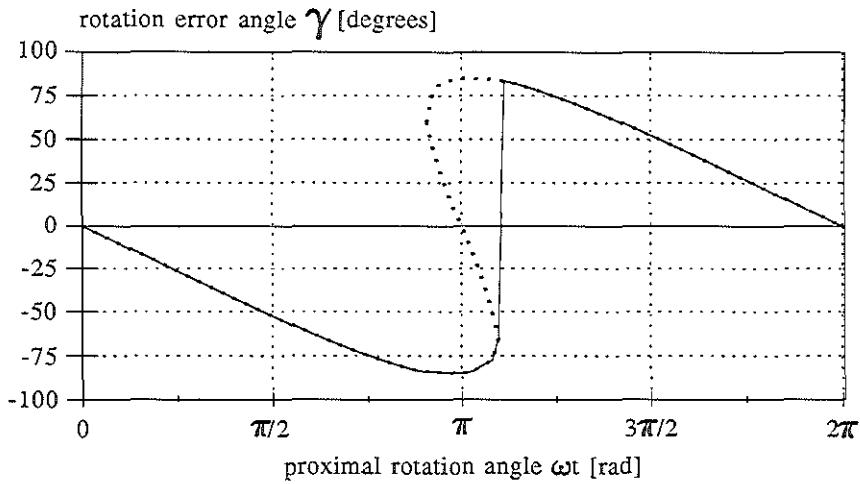


Fig. 4.1-3b Rotation error angle γ [degrees] due to drive-shaft pre-curvature for $B = 1.5$. Analytical model according to eqs. 4-11 and 4-6 (---); realistic curve with "whip-effect" (—).

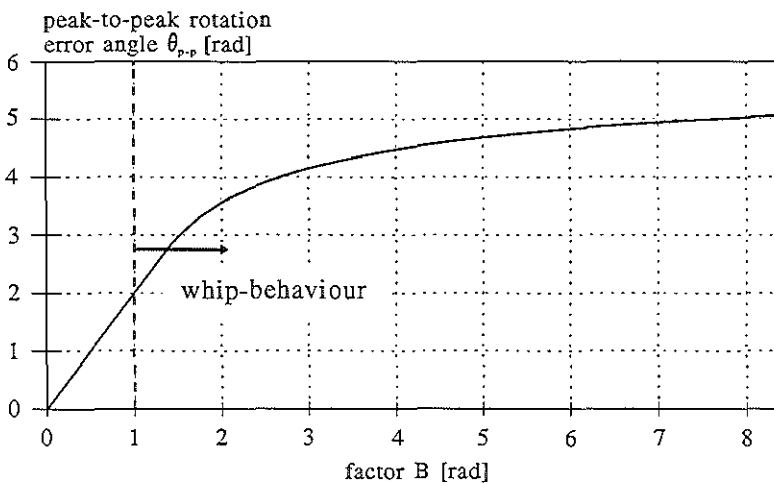


Fig. 4.1-3c Peak-to-peak rotation error angle θ [rad] due to drive-shaft pre-curvature as a function of the factor B.

Table 4.1-3 *B-value [rad] and peak-to-peak error angle γ_{p-p} [degrees] per metre straight length, caused by pre-curvature of the drive-shaft. Curve angle $\varphi_1 = \pi/2$.*

	SS-capillary		flex-shaft with optical fiber		SS double spiral type II	
	B [rad]	γ_{p-p} [°]	B [rad]	γ_{p-p} [°]	B [rad]	γ_{p-p} [°]
$\rho_0 = 20 \text{ mm}$	114	≈ 360	40.7	≈ 360	1.18	135
$\rho_0 = 100 \text{ mm}$	22.8	≈ 360	8.1	290	0.24	27.0
$\rho_0 = 1000 \text{ mm}$	2.28	220	0.8	93	0.024	2.7

It can be seen from Table 4.1-3 that these error angles are very large. It is therefore of utmost importance to avoid pre-curvature of the drive-shaft.

Improved model

If the assumption $l_1 \gg s_1$ is not valid, torsion in the curved section cannot be disregarded in comparison with the torsion in the straight section. In this case the rotation angle ψ of a point on the curved section cannot be approximated by ψ_2 . In Appendix B a better approximation model for the effect of pre-curvature on the drive-shaft running behaviour is derived similar to the improved model for $El_y \neq El_z$.

The rotation error angle θ_i over the straight section is given by:

$$\theta_i = -B \sin \left\{ \omega t + \left(1 + \frac{s_1}{3l_1}\right) \theta_i \right\} \quad (4-15)$$

where B is given by eq. 4-12 and for a drive-shaft curve angle $\varphi_1 = \pi/2$, B is given by eq. 4-13.

For the improved fit of this analytical model with the finite element model see Fig. 4.2-4.

The rotation error angle θ over the whole length of the shaft is given by:

$$\theta = -B \left(1 + \frac{s_1}{2l_1}\right) \sin \left\{ \omega t + \left(1 + \frac{s_1}{3l_1}\right) \theta_i \right\} \quad (4-16)$$

In comparison with eq. 4-11 the amplitude of the error angle is larger (a torsion angle over the curved section is added) and the phase-shift, predicted by this model, is also larger. If $l_1 \gg s_1$ is applied to the improved model, represented by eq. 4-16, it turns into eq. 4-11.

The criterion to ensure the absence of "whip" due to unequal bending rigidities in different bending planes is better represented by:

$$B \left(1 + \frac{s_1}{3l_1} \right) \leq 1 \quad (4-17)$$

Friction

A drive-shaft, enclosed by a catheter-tube with little clearance between drive-shaft and tube, can be bent in any given curve. External forces on the drive-shaft due to interaction between the tube and the shaft are needed to deform the drive-shaft, which follows the lumen of the tube. These forces give rise to friction, if the shaft is rotated around its central axis in this curved situation. Although in reality the intravascular US-catheter is filled with a fluid, as a conducting medium for the US-waves, the drive-shaft catheter-wall interaction is modelled to give rise to dry friction according to Coulomb. A possible lubricating effect will be discussed later.

In [2] a numerical model is proposed to determine axial and tangential friction forces on a catheter or a flexible cable while they are advanced from the femoral artery to the coronary arteries. The lateral interaction forces between the blood-vessel wall and the catheter/cable are modelled based on continuous interaction, giving rise to a distributed force over the whole length of the catheter/cable, depending on the local curvature. In reality this is not the case. Interaction between a catheter and the blood-vessel-wall (or between a drive-shaft and a catheter inner wall) is localized, as will be shown later. Many sections, even curved ones, will not be in contact with the wall. Curvature of these sections is possible by the presence of a bending moment, induced as a reaction to the localized forces, applied to the shaft elsewhere. Therefore another model will be proposed.

In principle it is possible to determine the external forces working on the drive-shaft, knowing the deformed geometry and the elastic properties of the shaft.

If large deflections occur, which is the case here, a numerical solution can be obtained. However, because the clearance of the drive-shaft in the catheter-tube is much smaller than the radius of curvature, the deformed geometry of the shaft is well represented by the curved centre-line of the tube. The effect of external forces onto this geometry can be studied, after which small deviations (within the clearance) will be taken into account. This assumption offers a valid simplification so that an analytical solution can be obtained, offering better and quicker comprehension of the effect of geometrical parameters and drive-shaft characteristics on the friction.

For the analytical model we describe a drive-shaft in a catheter-tube, bent in a simple curve.

Two cases are analysed in Appendix C:

1. A drive-shaft in a curved piece of tubing, with constant radius of curvature.
2. A drive-shaft in a curved piece of tubing, with a section of constant radius of curvature and two equal connecting straight ends.

Case 1

It is shown in Appendix C that the (constant) bending moment in the drive-shaft, causing the (constant) curvature, is induced by a couple of forces of interaction between the drive-shaft and the inside wall of the catheter-tube at both ends of the curve. If the clearance c of the shaft in the tube is small in comparison with the radius of curvature ρ , the two forces F , forming one couple, are situated close to each other, between which the drive-shaft crosses from the inside bend to the outside bend (Fig. C-2 and Fig. C-3).

The friction torque T_{fr} on the drive-shaft, caused by one couple of forces is:

$$T_{fr} = 2 \mu F \frac{d}{2} = \frac{\mu d E I}{\rho \sqrt{6 c \rho}} \quad (4-18)$$

where

d is the drive-shaft diameter

μ is the friction coefficient between drive-shaft and catheter-tube material

The rotation error angle θ over a shaft length l , which equals minus the torsion angle η due to this torque, is given by:

$$\theta = \psi_{dist} - \psi_{prox} = - \frac{T_{fr} l}{S_t} = - \frac{\mu d l E I}{S_t \rho \sqrt{6 c \rho}} \quad (4-19)$$

and is negative, because the direction of the driving rotation angle ωt is chosen to be positive.

The error angle θ represents a constant drag of the more distal shaft section and depends on geometrical parameters as well as drive-shaft and catheter-tube characteristics. Note that a very small positive clearance c , although enough to allow the drive-shaft to fit in the catheter-tube lumen, gives rise to a very high friction torque and error angle.

Case 2

Appendix C also describes the analysis in case the curve in the catheter-tube passes into straight sections at both ends. Again two couples of forces F determine the bending moment in the curved middle part, both situated at a transition between curved and straight tube sections (Fig. C-4 and Fig. C-5).

Here we find for the friction torque T_{fr} , caused by one couple of forces:

$$T_{fr} = 2 \mu F \frac{d}{2} = \frac{\mu d E I}{2 \rho \sqrt{6 c \rho}} \quad (4-20)$$

The rotation error angle θ over a shaft length l , which equals minus the torsion angle η due to this torque, is given by:

$$\theta = \psi_{dist} - \psi_{prox} = - \frac{T_{fr} l}{S_t} = - \frac{\mu d l E I}{2 S_t \rho \sqrt{6 c \rho}} \quad (4-21)$$

A straight section connected to the end of the curved part of the tube causes the arm of the couple of forces to increase with a factor 2, so that the lateral forces F are reduced to half, compared to case 1, which also applies for the friction torque and the rotation error angle.

Some rotation error angles γ in degrees (see eq. 4-6), caused by friction have been calculated for the simple geometry of Fig. 4.1-1, with a short distal straight section, and have been gathered in Table 4.1-4.

Note that two couples of forces are operating: one at $l = l_1$ and the other at $l = l_1 + s_1$.

Table 4.1-4 Tip-rotation error angle γ in degrees, caused by friction in a 90° curve with straight ends. For drive-shaft characteristics see Table 4.1-1.

Catheter tube ID = 1.14 mm, friction coefficient $\mu = 0.4$ (Table 4.2-1),
straight length = 1000 mm.

	SS-capillary $\gamma [^\circ]$	flex-shaft with optical fiber $\gamma [^\circ]$	SS double spiral type II $\gamma [^\circ]$
$\rho = 20$ mm	- 96	- 80	- 2.2
$\rho = 50$ mm	- 25	- 21	- 0.6
$\rho = 100$ mm	- 9	- 8	- 0.2

Lubrication

The catheter needs to be filled with a fluid to support US-energy transmission. This fluid may possibly also act as lubricating medium and hence reduce friction.

For medical safety reasons the choice of fluids is very limited. Only non-toxic and blood-compatible fluids can be considered. Even fluids that don't disperse easily can cause embolic complications, whenever they may be released into the bloodstream (oils). Water based fluids like saline may be the most obvious choice.

The rotating drive-shaft in the catheter-tube can be compared to a slide bearing. Especially the points of interaction, as defined in a previous section of this paragraph, can be modelled as such [3, 4].

Knowing the shaft diameter d , the tube inner diameter D , the angular velocity ω , the bearing load = normal force F_n and the viscosity of the fluid and estimating the order of magnitude of the axial bearing length, it is possible to predict the possible development and thickness of the fluid-film separating the two bearing surfaces.

Unfortunately the watery fluids have a very low viscosity (for water at 37 °C, the viscosity $\eta = 7 \cdot 10^{-4} \text{Ns/m}^2$). It appears that a flex-shaft type II, rotating with 1000 rpm in a catheter-tube with an inner diameter of 1.14 mm, filled with water and curved with a radius of 15 mm, develops a fluid-film of by far not enough thickness to separate the contact surfaces. The model of dry friction will be valid in this case, apart from some possible change in friction coefficient.

Application of less clearance between the drive-shaft and the catheter-tube inner wall or a much higher angular velocity of the shaft (e.g. 3600 rpm) still cannot create a situation of full film lubrication. Only a much more viscous fluid might help, although that could induce even more friction, because friction will become manifest over the whole length of the shaft.

If under circumstances, using a double-layer spiral flex-shaft, a lubricating film would be built up theoretically, the fluid pressure in the film, necessary to carry the load, might cause fluid transport into the shaft, passing the little spaces between the coils. This could also prevent the development of full film lubrication.

The situation for the SS-capillary in a curve with $\rho_1 = 100 \text{ mm}$ is even less promising for full film lubrication.

Material damping and internal friction

A drive-shaft which is bent in a curve and rotated around its central axis, will be forced to constantly bend and unbend in different planes. The deformation of the drive-shaft is never purely elastic. Even a solid drive-shaft, made of for instance stainless steel, will lose energy by internal friction and damping of the material. This loss of energy converted into heat has to be supplied by a driving torque, which causes an error angle.

The SS capillary drive-shaft will not lose much energy per revolution due to this material damping and internal friction; the elastic material behaviour dominates the driving torque as described in previous sections of this paragraph.

The double-layer spiral drive-shaft, however, may show more hysteresis in a bending cycle, depending on material and construction, which means that some non-elastic behaviour is present. This behaviour can probably be explained by the friction between the inner and outer spiral coils. The contact surfaces of the coils may give rise to more friction when flat wire is used than when the coils are wound of round wire.

Non-elastic behaviour not only causes the presence of a driving torque and error angle, it can also change the shape of the drive-shaft. E. g. a double-layer spiral drive-shaft may receive a pre-curvature, without plastic deformation of the coil material itself, after having spent some time under certain curved conditions. This may look like time-dependent material behaviour, but a stick-slip friction phenomenon between the coils is a more likely cause. The pre-curvature obtained this way may cause a periodic error angle as described before. But because of the non-elastic behaviour it may also be reversible as soon as the radius of curvature forced onto the rotating shaft (in a curved catheter-tube) is becoming equal to or smaller than the radius of pre-curvature.

It seems therefore of great importance not only to produce drive-shafts as straight as possible, but also to maintain this straightness by handling the shafts with great care and storing them as straight as necessary to avoid pre-curvature.

A safe minimum radius of curvature that will not at all induce pre-curvature in a certain type of drive-shaft cannot be given without extensive experimentation. Also the nature and magnitude of the non-elastic drive-shaft behaviour should be investigated experimentally just as their effect on the running behaviour of the drive-shaft.

Fundamental frequency and inertia

The system under consideration for the analysis of the fundamental frequency consists of the drive-shaft as elastic element, and the inertia distributed over the drive-shaft and represented by the transducer-tip. The transducer-tip is very small and represents not much more inertia than a piece of the drive-shaft of the same measures would do. Therefore this inertia will be neglected.

The linear coordinate x is defined along the central rotational axis of the shaft.

For every infinitesimal part dx of the shaft we find:

$$dT = J_t dx \ddot{\eta} \Rightarrow \frac{dT}{dx} = J_t \ddot{\eta} \quad (4-22)$$

where

dT = infinitesimal change of torque

J_t = moment of inertia with respect to the central rotational axis, per unit length

η = torsion angle (= - rotation error angle θ)

For torsion it is known that:

$$T = \frac{S_t d\eta}{dx} \Rightarrow \frac{dT}{dx} = S_t \frac{d^2\eta}{dx^2} \quad (4-23)$$

Eqs. 4-22 and 4-23 give, considering $\theta = -\eta$:

$$\frac{\partial^2 \theta}{\partial t^2} = \frac{S_t}{J_t} \frac{\partial^2 \theta}{\partial x^2} \quad (4-24)$$

A solution of the differential equation, containing the fundamental frequency ω_0 can be found as:

$$\theta = \theta_0 \cos \omega_0 t \sin bx \quad (4-25)$$

Substitution of this solution into eq. 4-24 and using the initial condition that at $t = 0$ and $x = l \Rightarrow \theta = \theta_0$, result in:

$$b = \frac{\pi}{2l} \quad \text{and} \quad \omega_0 = \frac{\pi}{2l} \sqrt{\frac{S_t}{J_t}} \quad (4-26)$$

Given the moments of inertia per unit length:

SS capillary: $J_t = 4.5 \cdot 10^{-11} \text{ kgm}^2/\text{m}$,

double-layer spiral flexible drive-shaft, type I: $J_t = 2.3 \cdot 10^{-10} \text{ kgm}^2/\text{m}$ (filling 67% stainless steel), double-layer spiral flexible drive-shaft, type II: $J_t = 1.9 \cdot 10^{-10} \text{ kgm}^2/\text{m}$ (filling 69.5% stainless steel) and the torsional rigidities according to Table 4.1-1, the fundamental frequencies for a free length of 1 m can be calculated and compared with the rotation and the excitation frequencies (Table 4.1-5).

Table 4.1-5 Fundamental frequency of drive-shafts in comparison with rotation and excitation frequencies. Free length of the drive-shaft is 1 m.

	fundamental frequency [Hz]	rotation frequency [Hz]	excitation frequency [Hz]	
			$EI_y \neq EI_z$	pre-curvature
SS capillary	715			
SS double spiral type I	82	16.7	33.3	16.7
SS double spiral type II	181			

In these cases the fundamental frequency is much higher than the maximum driving frequency of 16.7 Hz (1000 rpm) and the excitation frequencies due $EI_y \neq EI_z$ and pre-curvature. Periodic error angles will therefore not be amplified by resonance.

It also means that for a drive-shaft tip-rotation with a uniform rotation component and a sine-shaped error angle component, with sub-critical frequency, the influence of inertia of the shaft can be neglected. For small values of the factors A and B (eqs. 4-3 and 4-12) this is the case, so that the static analysis, as presented, is valid.

For larger values of the factors A and B, when the rotation error angle curve becomes saw-tooth shaped, the influence of inertia may change the curve in the specific section where large rotation angle accelerations occur. However, these sections of the rotation error angle curve are small so that not much effect is to be expected.

Gravitation

If the mass per unit length of the drive-shaft is m/L , the supporting force per unit length, applied to the drive-shaft by the catheter-tube, if situated in a horizontal plane, is mg/L ($g = 9.8 \text{ m/s}^2$ is acceleration due to gravitation). The torque T_{Gx} necessary to overcome friction due to this lateral force, as a function of the axial coordinate x is:

$$T_{Gx} = \frac{\mu m g}{L} \frac{d}{2} (L - x) \quad (4-27)$$

and the distal rotation error angle θ_{GL} is:

$$\theta_{GL} = - \int_0^L \frac{T_{Gx} dx}{S_t} = - \frac{\mu mg d L}{4 S_t} \quad (4-28)$$

In Table 4.1-6 the driving torque $T_{G,0}$ and the tip-rotation error angle γ_{GL} (eqs. 4-28 and 4-6) due to friction, caused by gravitation, can be found for several types of drive-shafts of 1 m length and positioned in a horizontal plane. As a comparison the driving torque T_{fr} (eq. 4-20) due to friction, caused by a 90° curve with a radius $\rho = 100 \text{ mm}$ and straight ends has been added.

These figures show that for drive-shafts with a lower bending rigidity, like the double-layer spiral flex-shafts, the positioning of the catheter in space will significantly influence or even dominate the friction contribution to the total driving torque, which of course still may be small compared to other influences. Indeed in these cases the distributed friction force due to gravitation causes only small error angles γ_{GL} .

Table 4.1-6 Effect on drive-shaft rotation of friction due to gravitation, for several drive-shafts (Table 4.1-1 and Table 4.2-1); also in comparison with friction due to curvature ($\rho = 100 \text{ mm}$ and straight ends). Shaft length of 1 m, positioned in a horizontal plane.

	$T_{G,0}$ [10^{-3} Nmm]	T_{fr} [10^{-3} Nmm]	γ_{GL} [$^\circ$]
SS capillary	1.0	54.5	- 0.08
SS double spiral type I	3.1	2.0	- 3.6
SS double spiral type II	2.7	0.3	- 0.8

Reduction of EI , while EI/S_t is constant, does not change the effect of all influences previously dealt with. But θ_G is proportional to $1/S_t$ and not to EI/S_t . Reduction of EI and S_t by a factor 5 to 10 (while maintaining all other parameters), starting from flex-shaft type II, will allow gravitation to play a role of some importance, meaning that a change in the error angle in the order of several degrees may be observed when the catheter is positioned differently in space, while maintaining its geometry.

Because error angles due to gravitation are small for the drive-shafts currently in use, this friction component will be disregarded henceforth. In case error angles due to friction will be mentioned, only the component due to curvature is taken into account.

Combination of influences

The influences which determine the running behaviour of the tip of the drive-shaft have been described separately in the previous sections of this paragraph. In reality they all work together, also influencing each other's effect on the error angle. This situation becomes too complex to describe analytically. If needed the final element method can show combined effects in well defined cases.

It is possible, however, to make some theoretical estimations about the order of magnitude of the different influences, when they work together. It will show that under certain circumstances one influence may be neglected compared to the other.

$EI_y \neq EI_z$ and pre-curvature combined with friction

Unequal bending rigidities in different bending planes as well as pre-curvature causes a fluctuation of the friction torque, which then creates another periodic rotation error angle. In Appendix D it is shown that for practical situations, the effect of the fluctuating friction due to $EI_y \neq EI_z$ and pre-curvature can be neglected with respect to the effect of these phenomena themselves.

$EI_y \neq EI_z$ combined with pre-curvature

These two influences are given by drive-shaft characteristics and this way they are coupled. The unequal bending rigidities EI_y and EI_z are defined respectively for bending in the $x\bar{z}$ - and $x\bar{y}$ -plane of the drive-shaft (Fig. B-2). The plane in which the pre-curvature of the shaft occurs is also fixed with respect to the drive-shaft. The relative angular position of these planes determines whether both effects will amplify or compensate each other in the resulting error angle. As worst case we assume the plane of pre-curvature to be the $x\bar{z}$ -plane. In that case once per revolution an extreme error angle will occur equal to the sum of the extremes of both effects.

Summation of effects

The effects of the three most important influences on the error angle, mentioned above, can roughly be summed up to obtain an estimation of the resulting effect, taking into account that unlike the two others, friction does not cause a periodic error angle with, in practical cases, alternating negative and positive values, but a constant "running behind" (drag). The more practical geometry with straight ends at both sides of the curve is used for the friction model (case 2).

From eqs. 4-2 (or 4-8) and 4-5, 4-11 (or 4-15) and 4-13 and 4-21 (for two couples of forces operating), combined with eq. 4-6, it can be deduced that:

$$\gamma_{EI} = Q \frac{p}{\rho_1} \quad (4-29)$$

$$\gamma_{\rho_0} = \frac{Q}{\rho_0} \quad (4-30)$$

$$\gamma_{fr} = Q \frac{2q\mu}{\rho_1 \sqrt{\rho_1}} \quad (4-31)$$

where

γ_{EI} [°] = the extreme error angle, just proximal to the curve, due to $EI_y \neq EI_z$

γ_{ρ_0} [°] = the extreme error angle, just proximal to the curve, due to pre-curvature

γ_{fr} [°] = the constant error angle, just proximal to the curve, due to friction

$$q = \frac{d}{\pi \sqrt{6c}} \quad [\sqrt{mm}] \quad (4-32)$$

and is hence only dependent on the drive-shaft and catheter-tube dimensions, whereas:

$$Q = \frac{90 EI}{S_t} \quad [^\circ mm] \quad (4-33)$$

only depends on the drive-shaft characteristics.

Fig. 4.1-4 shows the rotation error angle γ in degrees⁽²⁾, per metre straight length of the drive-shaft, proximal to the curve, for all three influences as a function of the radius of curvature of the catheter ρ_1 (the effect of pre-curvature does not depend on ρ_1 , if always the same curve angle is applied, here $\phi_1 = \pi/2$). For a defined combination of drive-shaft and catheter-tube, all three influences are dependent on one more parameter, respectively p , ρ_0 and μ .

The behaviour of the SS-capillary drive-shaft combined with the 5.2 French CORDIS angio-catheter (1.73 mm OD) is shown in Fig. 4.1-4a, the characteristics of the double-layer spiral flex-shafts type I and II combined with the same catheter-tube are the basis of respectively Fig. 4.1-4b and Fig. 4.1-4c on page 88.

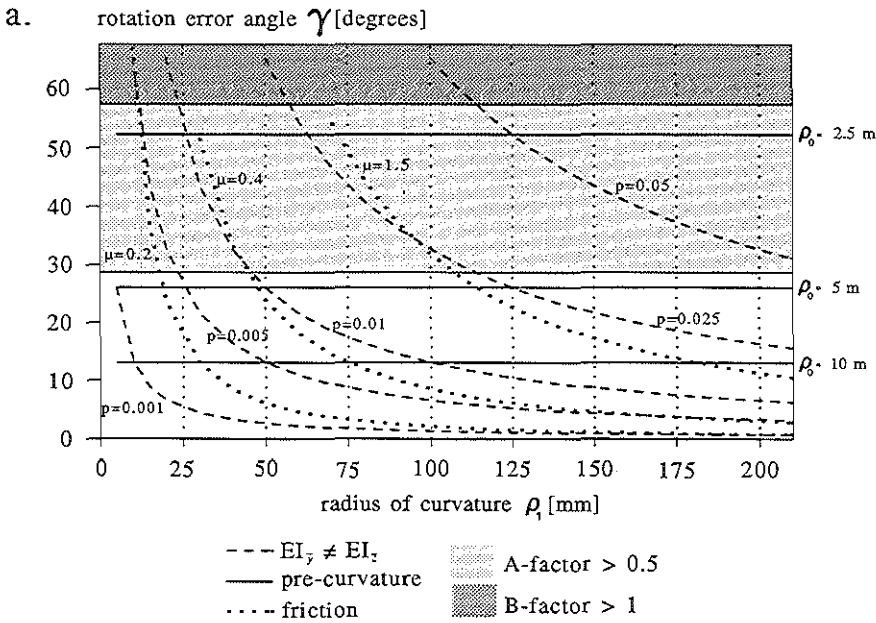


Fig. 4.1-4 Rotation error angle γ [degrees]⁽²⁾, just proximal to the curve, per metre straight proximal length, due to $EI_1 \neq EI_2$, pre-curvature and friction independently, as a function of ρ_1 and dependent on respectively p , ρ_0 and μ . The error angles are shown for a SS-capillary drive-shaft (a) and for the double-layer spiral flex-shafts type I (b: page 88) and type II (c: page 88), in a 5.2F angio-catheter (1.14 mm ID). Geometry: long proximal straight part with distal 90° curve with radius ρ_1 and short distal straight end.

⁽²⁾For $EI_1 \neq EI_2$ and pre-curvature the amplitude of the periodic rotation error angle is meant here, whereas in the case of friction, γ is the constant "drag" angle, which is shown here to be positive, for easier comparison with the other curves.

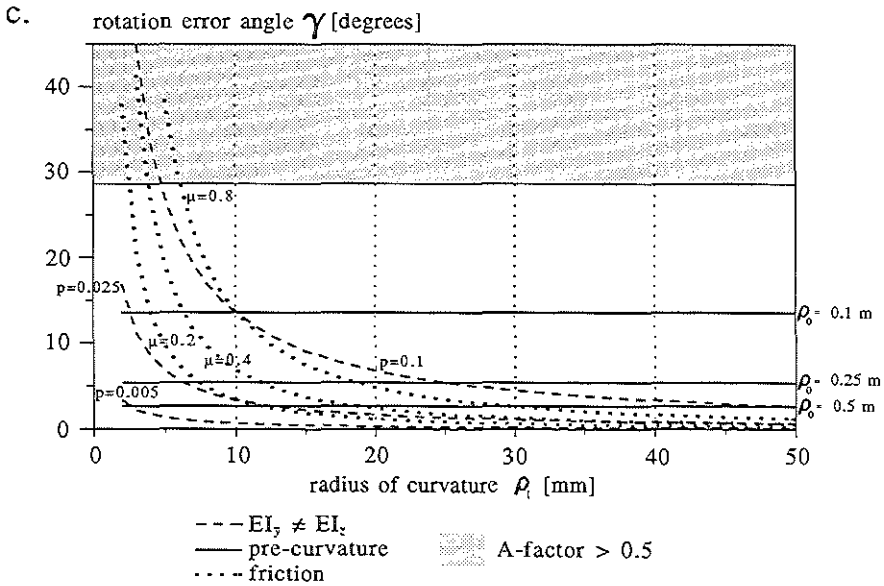
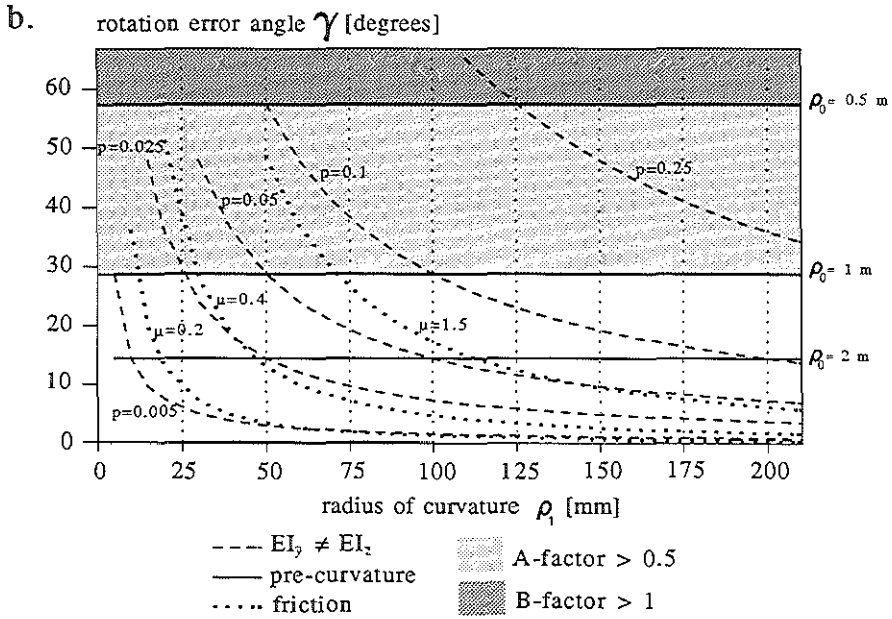


Fig. 4.1-4b,c See caption page 87.

Among other things these figures show that:

- The rotation error angle of a SS-capillary drive-shaft is much more sensitive to the parameters influencing the running behaviour than is the case for the flex-shafts.
- Friction starts to play a role for a small radius of curvature or high friction coefficient μ . For a SS-capillary and $\mu = 0.4$, this happens if $\rho_1 < 100$ mm; for flex-shaft type II, if $\rho_1 < 10$ mm. This latter drive-shaft therefore is suitable for use under extremely curved conditions as far as friction is concerned ($\rho_1 \approx 15$ mm in coronary use).
- Pre-curvature is a dangerous phenomenon, ruining the uniformity of the catheter-tip running behaviour. Already a relatively large radius of pre-curvature of 100 mm causes a peak-to-peak error angle of 30° in the best flexible drive-shaft (type II). Plastic deformation of the SS-capillary shows to be disastrous.
- If the maximum acceptable peak-to-peak error angle is 20° and the minimum radius of curvature at the tip (for coronary use) is 15 mm, the bending rigidity in different bending planes should be controlled for the flex-shaft type II within 20 % ($p < 0.1$, see eqs. B-9 and B-13); for flex-shaft type I within 1%.

§ 4.2 Finite element modelling

Introduction

The finite element method (FEM) is a powerful tool to investigate the combined effects of influences on the running behaviour of the drive-shaft. The FEM will show the drive-shaft rotational behaviour for one case, specified in the model input. Many computer runs will be necessary to reveal tendencies and dependencies in order to gain understanding of the underlying mechanics of a rotating (flexible) drive-shaft in a curved tube.

Results of the analytical models of § 4.1 are compared with results of FEM-calculations, to verify their validity. At the same time the reliability of the finite element model will be tested, so that for more complicated configurations, where analytical modelling will fail, a reliable model is available.

Model description

The catheter drive-shaft is modelled by a string of spatial beam elements, having two nodal points at the ends. The shaft is confined within a catheter-tube with an inner diameter D which is larger than the outer diameter d of the string. It is assumed that the catheter-tube is clamped at one end, while the shaft is driven by a motor at a constant angular velocity.

A dedicated FEM computer program has been composed, containing methods from the SPACAR program. Both have been developed at the Laboratory for Engineering Mechanics of the Delft University of Technology, Faculty of Mechanical Engineering and Marine Technology. The software is based on dynamic analysis, so that a finite element model describing kinematics and dynamics of the shaft has been used, although a static analysis would have been sufficient (§ 4.1).

The description of the kinematic and dynamic modelling for the nodes, the elements and the interaction between the shaft and the wall of the tube can be found in Appendix E, together with a description of the solution method for the resulting equations.

Use of the model

Input

The input data for the program are divided in two parts: the definition of the geometry of the structure under investigation and the mechanical parameters, ruling the drive-shaft behaviour. The geometry of the structure is defined by the determination of the xyz-coordinates of the nodal points and the tangent in these points. The structure mostly used for the modelling of the flexible drive-shaft is shown in Fig. 4.2-1.

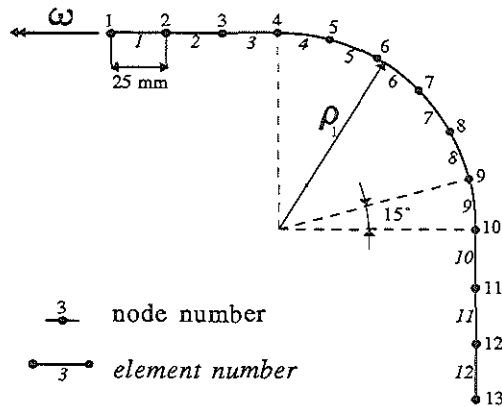


Fig. 4.2-1 Structure mostly used for FEM-calculations: a single 90° curve with radius ρ_1 and two straight ends.

The main input parameters are:

for the drive-shaft (element data):

- outer diameter d [mm]
- bending rigidities EI_r and EI_t [10^{-3}Nmm^2]
- torsional rigidity S_t [10^{-3}Nmm^2]
- axial stiffness EA [10^{-3}N]
- mass per length [kg/mm]
- damping parameters SD [s]
(damping = $SD \times \text{stiffness}$ [$10^{-3}\text{Nmm}^2\cdot\text{s}$])
- pre-curvature/initial strain

for the catheter-tube:

wall contact:

- inner diameters D_1 [mm] and D_2 [mm]
- wall-stiffness [10^{-3}N/mm^2] (Fig. 4.2-7)
- friction coefficient μ

for the calculation process:

- circular frequency ω [rad/s]
- time interval [s]
- time step [s]

The values chosen for these parameters in the FEM-calculations are partly found from real drive-shafts and a 5.2F CORDIS angiographic catheter (Table 4.2-1). For the driving rotation frequency $\omega = 100$ rad/s has been chosen (≈ 1000 rpm).

Table 4.2-1 Practical parameters for FEM-calculations.

	EI/S_t [$\text{Nmm}^2/\text{Nmm}^2$]	EA [10^3 N]	d [mm]	mass/L [g/m]	ID [mm]	μ
SS capill.	534/368	25.13	0.5	0.98	0.3	--
flex-shaft type I	8/25	0.132	0.84	1.91	0.5	--
flex-shaft type II ⁽³⁾	1.5/100	--	0.80	1.70	0.5	--
5.2F Angio-cath.	--	--	--	--	1.14	0.4 ⁽⁴⁾

⁽³⁾Not used for FEM-calculations.

⁽⁴⁾For lack of a more realistic figure, an upper limit for the friction coefficient is chosen by using the static friction coefficient between poly-urethane and stainless steel, known from handbooks, disregarding the relative motion between the shaft and the tube-wall and the presence of a fluid.

Output

The program allows for presentation of output data in two ways:

1. As a function of time.

A maximum of 3 quantities for a given nodal point (coordinates, displacements/rotations, linear and angular velocities and accelerations, internal forces/moments or external forces/moments) or element (stresses and strains) can be monitored in time. Most interesting are the rotation angles of nodes 1, 4 and 13 (Fig. 4.2-1), from which the rotation error angles can be derived.

2. Representing the status at the end of the calculation.

All data for all nodal points and elements, representing the status at the end of the defined time interval for calculation, become available.

The results of the finite element modelling, combined with corresponding analytical results will be presented in figures. The choice of parameter combinations and graphs is made to facilitate comparison of the two methods.

Unequal bending rigidities in different bending planes; $EI_y \neq EI_z$

The structure of Fig. 4.2-1 has been used for the calculations. Some parameters were changed in different calculation runs to investigate their influence on the error angle (Table 4.2-2).

Table 4.2-2 Input parameters for several FEM-calculation runs to investigate their influence, when $EI_y \neq EI_z$

run #	\bar{EI} [Nmm ²]	S_t [Nmm ²]	\bar{EI}/S_t	$p = \frac{(EI_z - EI_y)}{(EI_y + EI_z)}$	ρ_1 [mm]
a1	534	368	1.45	0.01	100
a2	534	368	1.45	0.05	100
a3	534	368	1.45	0.25	100
a4	8	25	0.32	0.01	100
a5	8	25	0.32	0.05	100
a6	8	25	0.32	0.25	100
a7	450	500	0.90	0.01	100
a8	90	100	0.90	0.05	100
a9	18	20	0.90	0.25	100
a10	8	25	0.32	0.05	147.7
a11	8	25	0.32	0.05	20

Fig. 4.2-2 shows as illustration the results of run a2 (a) and run a3 (b). The rotation error angle over the first straight 75 mm (nodal point 4) is shown as a function of the driving rotation angle ωt . Also the results of the first approach and improved analytical models for these cases are given in this figure. They are very similar and especially Fig. 4.2-2b shows the better fit of the improved model with the FEM-results.

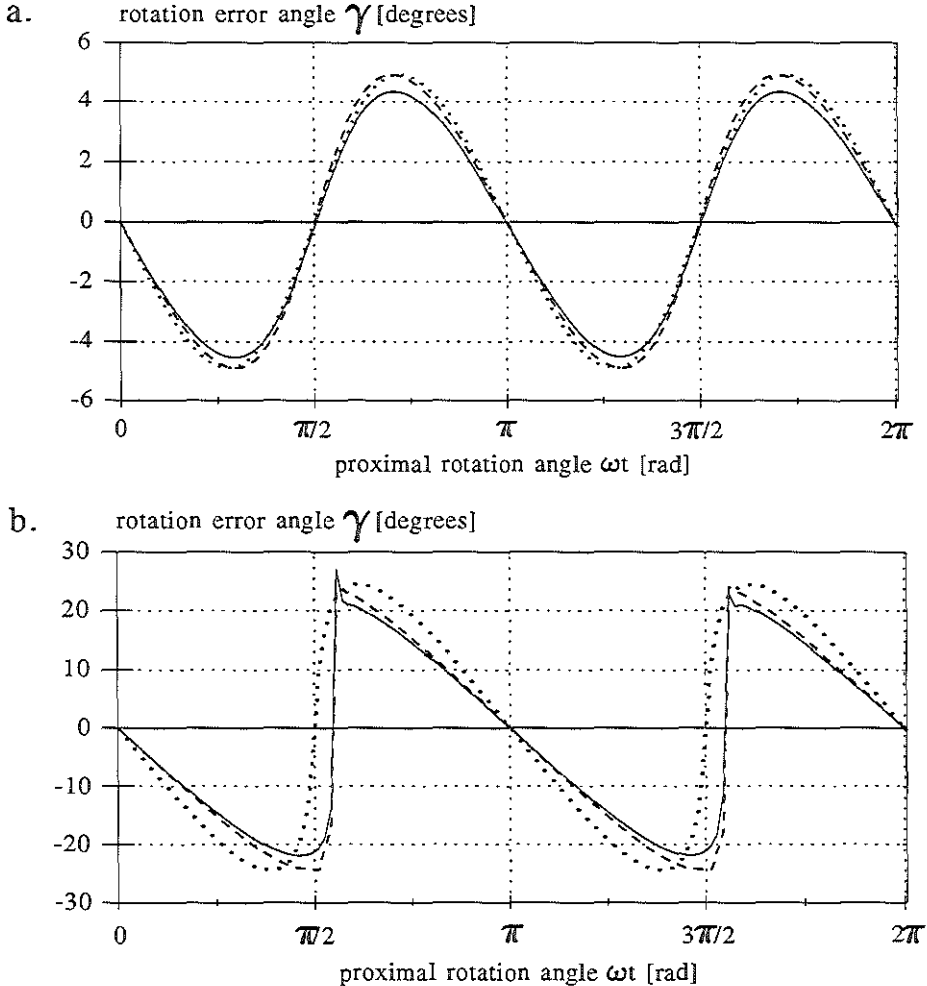


Fig. 4.2-2 Rotation error angle γ , just proximal to the curve, due to unequal bending rigidities in different bending planes, as a function of the driving rotation angle for run a2 (a), where $A = 0.085$ rad and run a3 (b), where $A = 0.427$ rad. First approximation analytical model (\cdots); improved analytical model ($---$); finite element model ($-$).

Fig. 4.2-3 shows the amplitude of the error angle γ (γ_{\max}) [degrees] of nodal point 4 as a function of respectively p (a), \bar{EI}/S_i (b) and $1/\rho_1$ (c) (see also eq. 4-5), both as a result of the FEM-calculations and the analytical model. The results are very similar and the proportionality of γ_{\max} with these parameters is being confirmed. Fig. 4.2-3d shows the phase-shift of the extreme value of the error angle. The FEM-results are compared with the improved analytical model and they match well. Comparison of the phase-shift for small error angles is not possible, because the resolution of the phase-shift, chosen in the output of the FEM-program, was $0.05 \text{ rad} \approx 3^\circ$.

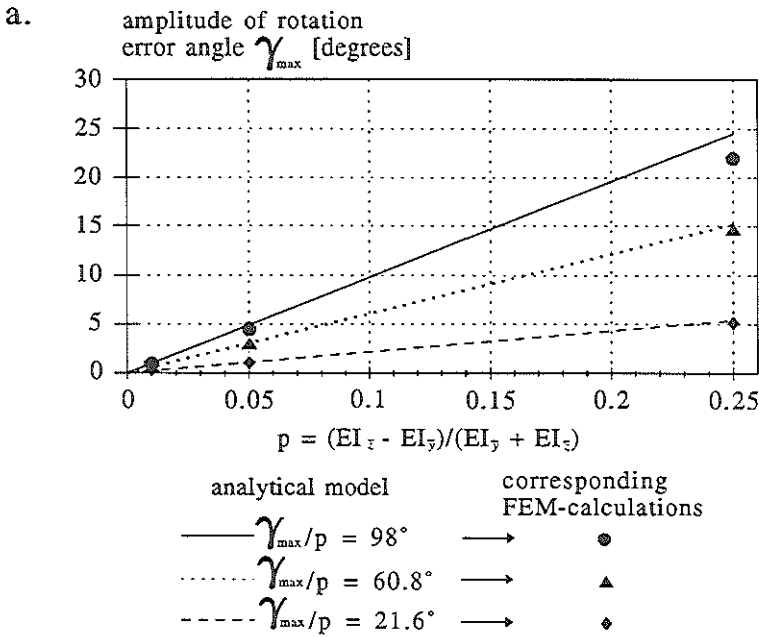
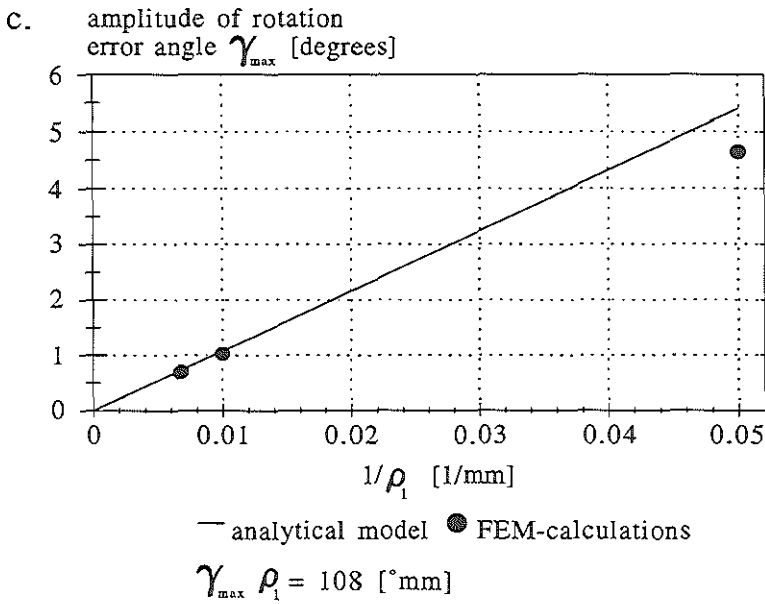
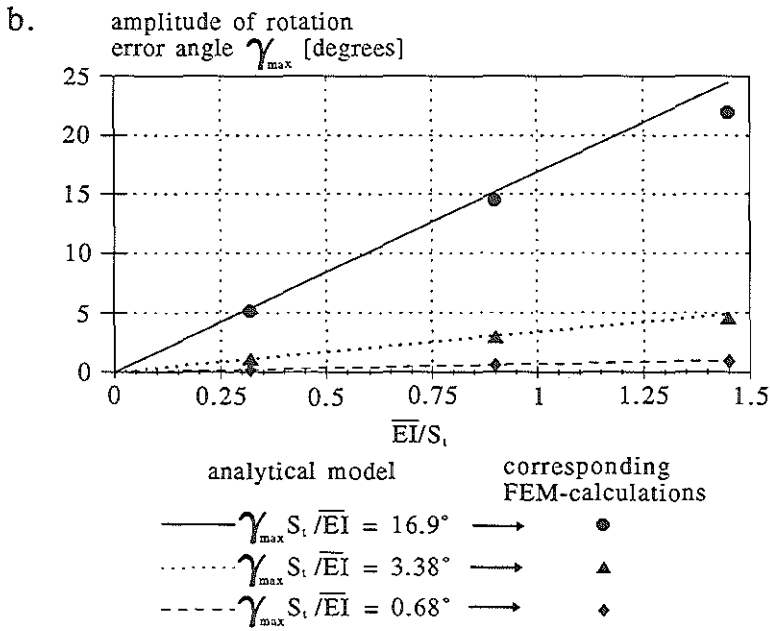


Fig. 4.2-3 Amplitude of rotation error angle γ_{\max} [degrees], just proximal to the curve, due to unequal bending rigidity in different bending planes as a function of p (a), \bar{EI}/S_i (b: page 95) and $1/\rho_1$ (c: page 95). Phase-shift of the extreme values of the error angle (d: page 96). FEM-calculations against improved analytical model.



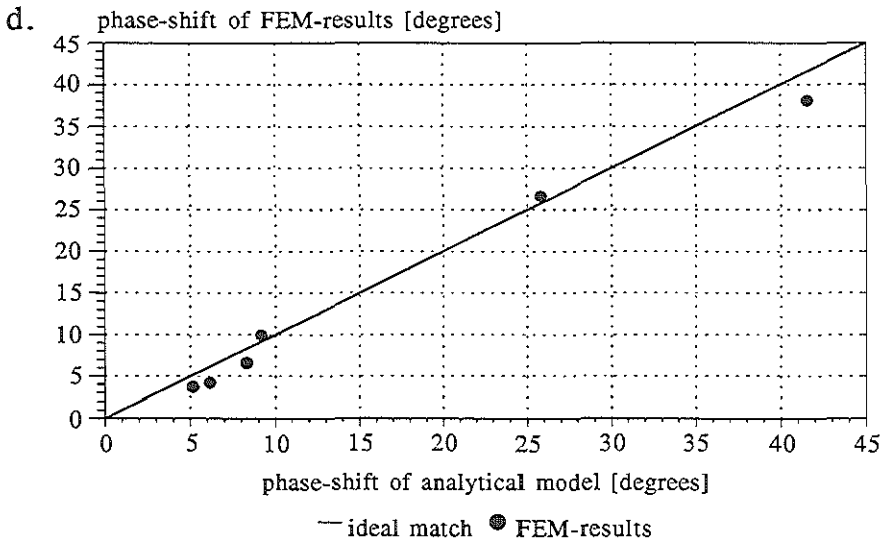


Fig. 4.2-3d See caption page 94.

Pre-curvature

The same structure of Fig. 4.2-1 has been used for these calculations and the changes of parameters in different calculation runs are shown in Table 4.2-3.

Fig. 4.2-4 shows the error angle γ over the first straight 75 mm (nodal point 4) as a function of the driving rotation angle, for run b1, as a result of the FEM-calculations in combination with the first approach analytical model and the improved model. Again a close fit can be observed especially between the FEM and the improved analytical model.

Table 4.2-3 Input parameters for FEM-calculation runs to investigate their influence, in case of pre-curvature.

run #	EI [Nmm ²]	S _t [Nmm ²]	EI/S _t	ρ ₀ [mm]
b1	534	368	1.45	100
b2	534	368	1.45	1000
b3	8	25	0.32	100
b4	106.8	73.6	1.45	100
b5	8	25	0.32	1000
b6	1.6	5	0.32	100
b7	4	25	0.16	100
b8	50	50	1.0	100
b9	30	50	0.60	100
b10	534	368	1.45	200
b11	8	25	0.32	200

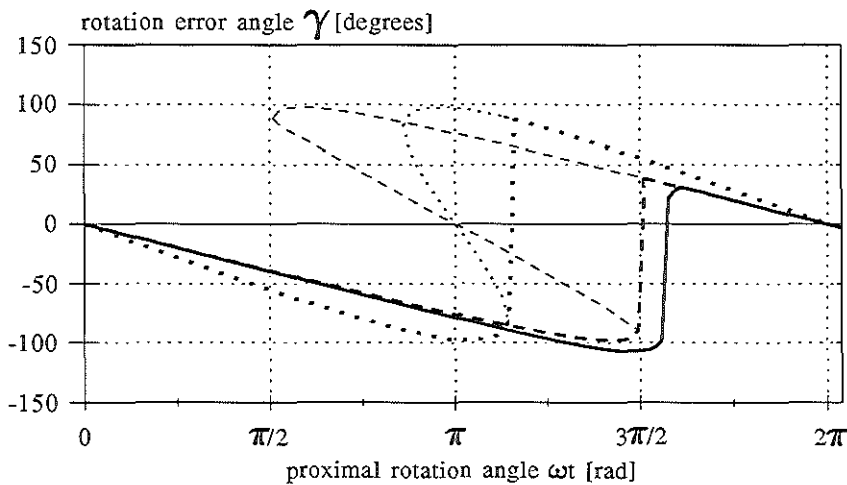


Fig. 4.2-4 Rotation error angle γ [degrees], just proximal to the curve, due to pre-curvature as a function of the driving rotation angle for run b1 ($B = 1.71$). FEM-results (—) combined with the first approach analytical model (···) and the improved model (---). Note: the bold dashed and dotted lines represent the practical rotational behaviour, including "whip".

Fig. 4.2-5 shows the amplitude of the error angle γ (γ_{\max}) of nodal point 4 as a function of respectively EI/S_t (a) and $1/\rho_0$ (b) (see also eq. 4-13), both as a result of the FEM-calculations and the analytical model. The results are very similar and the proportionality of γ_{\max} with these parameters is being confirmed. Fig. 4.2-5c shows the phase-shift of the extreme value of the error angle. The FEM-results are compared with the improved analytical model and they match very well again. Comparison of the phase-shift for small error angles is again not possible, because the resolution of the phase-shift, chosen in the output of the FEM-program, was $0.05 \text{ rad} \approx 3^\circ$.

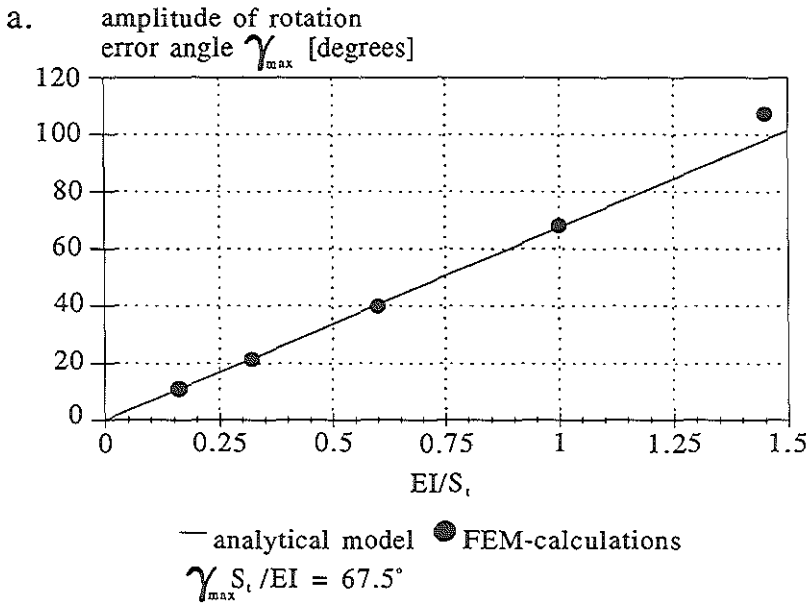
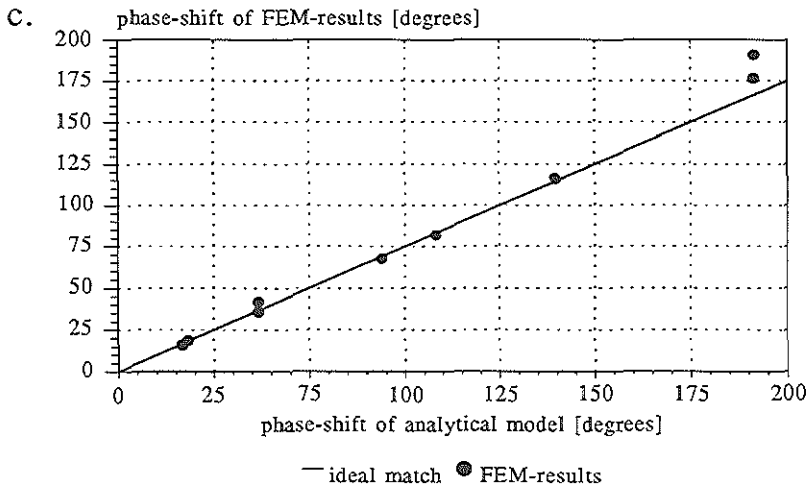
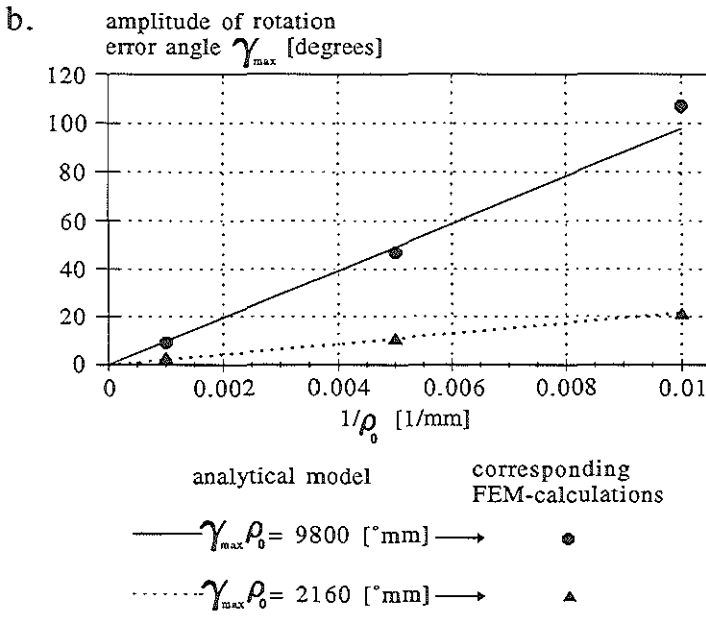


Fig. 4.2-5 Amplitude of the rotation error angle γ_{\max} [degrees], just proximal to the curve, due to pre-curvature as a function of EI/S_t (a) and $1/\rho_0$ (b: page 99). Phase-shift of the extreme values of the error angle (c: page 99). FEM-calculations against improved analytical model.



Friction

Two different drive-shaft geometries have been used for the FEM-calculations, corresponding with the two cases described in § 4.1. The first is merely a 90° curve with no straight ends, represented by a structure which equals the part of the structure of Fig. 4.2-1 between the nodal points 4 and 10 (structure 1). The second is represented by Fig. 4.2-1 entirely (structure 2). A third structure has been used for calculations, representing the geometry of case 1, but with smaller elements at the proximal and distal ends (Fig. 4.2-6).

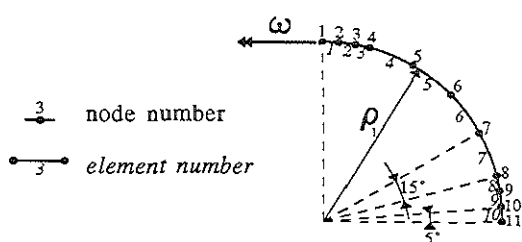


Fig. 4.2-6 Structure 3, used for FEM-friction-calculations, representing the geometry of case 1 (§ 4.1: Friction): 90° curve with radius ρ_1 and no straight ends, with smaller proximal and distal elements.

In structures 1 and 3 the driving motor, operating at the proximal end, centres the drive-shaft, so that shaft-wall interaction is not possible here. Only at the distal end of the curve friction forces occur. In the second structure the shaft is centred in the proximal nodal point 1, which hardly influences the interaction between drive-shaft and catheter-tube-wall close to nodal points 4 and 10.

The different parameters for which FEM-calculations were carried out can be found in Table 4.2-4. Especially different values for modelling the shaft-wall contact have been investigated. The wall-stiffness describes the increase of the reaction force on the shaft, when it slightly intrudes into the catheter-tube wall. The wall-stiffness has been modelled using three parameters: a first catheter-tube inner diameter (D_1), at which the shaft, moving out of the centre of the tube, will come in contact with the wall and a second, larger inner diameter (D_2), from which a linear increase of the reaction force on the shaft starts with a defined slope ($\tan \zeta = \text{wall-stiffness}$, see Fig. 4.2-7). Between D_1 and D_2 the reaction force increases according to a fourth order polynomial.

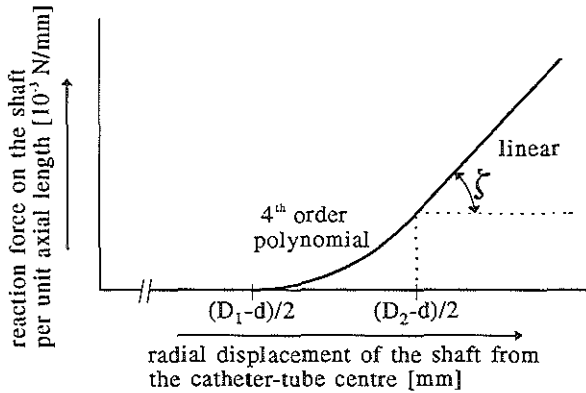


Fig. 4.2-7 Modelling of the contact between drive-shaft and inner wall of the catheter-tube.
 Wall-stiffness = $\tan \zeta$ $[10^{-3} \text{ N/mm}^2]$

For all calculations the parameters of the SS-capillary drive-shaft have been used and a radius of curvature $\rho_1 = 100 \text{ mm}$.

In the FEM-calculation runs, the friction forces build up to a certain level. To reach a stable solution, damping has to be present in the model, representing an energy loss in the drive-shaft. In run c1 the friction coefficient $\mu = 0$ has been chosen, to investigate the resulting torque and error angle due to only this damping.

Table 4.2-4 Input parameters for FEM-calculation runs to investigate their influence, in case of friction. Shaft is SS-capillary (Table 4.2-1).

run #	structure #	wall-contact: $D_1/D_2/\tan \zeta$ $[\text{mm}]/[\text{mm}]/[10^{-3} \text{ N/mm}^2]$	μ
c1	1	1.12/1.16/1000	0
c2	1	1.00/1.28/100	0.4
c3	1	1.10/1.20/500	0.4
c4	1	1.12/1.16/1000	0.4
c5	2	1.00/1.28/100	0.4
c6	2	1.12/1.16/1000	0.4
c7	3	1.00/1.28/100	0.4
c8	3	1.13/1.15/5000	0.4

Fig. 4.2-8 shows the driving torque T_{fr} and the corresponding rotation error angle γ_{fr} , calculated by different FEM-runs and as a result of the analytical model. The contribution of the damping is also shown in this figure.

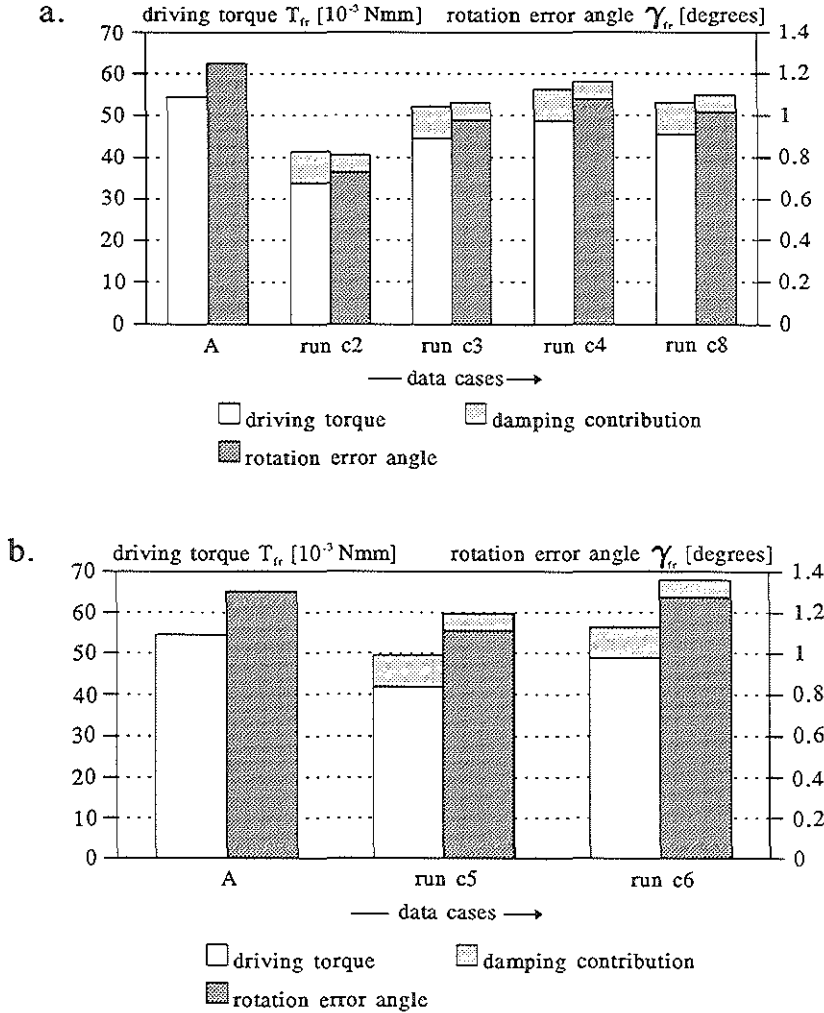


Fig. 4.2-8 Driving torque T_{fr} and rotation error angle γ_{fr} of the distal tip, due to friction of a SS capillary in a catheter-tube, bent in a 90° curve with radius of 100 mm, without straight ends (a) and with straight ends (b). FEM-runs are compared with analytical results (A).
Note: in (a) only one couple of forces operates at the distal part of the curve, in (b) at both sides of the curve a couple of forces operates.

The results are very similar and match better when a higher wall stiffness is used. A lower wall stiffness gives rise to more deformation of the material, so that the inner diameter of the catheter-tube appears to be larger, causing the torque and error angle to decrease.

The end-status of the FEM-calculations gives all external nodal forces in the stabilized situation. As would be expected from the analytical model we find external nodal forces not equal to zero only for nodal points close to the beginning or ending of the curve, because here the interaction between shaft and catheter-tube takes place. From these forces and the position of the nodal points the lateral forces F on the drive-shaft, inducing the bending moment, and the angle of non-contact β can be estimated and compared with the analytical results. This has been done for runs c4, c8 and c6 (Table 4.2-5).

Table 4.2-5 Comparison between FEM results and analytical model showing the drive-shaft-wall contact, expressed in lateral forces F and "angle of non-contact" β (Fig. C-5).

run #	Lateral forces F of bending couple [10^{-3}N]		Angle of non-contact β [rad]	
	FEM	Anal. model	FEM	Anal. model
c4	208/236	274/274	0.209	0.196
c8	212/238	274/274	0.209	0.196
c6	81/105	136/136	0.407	0.393

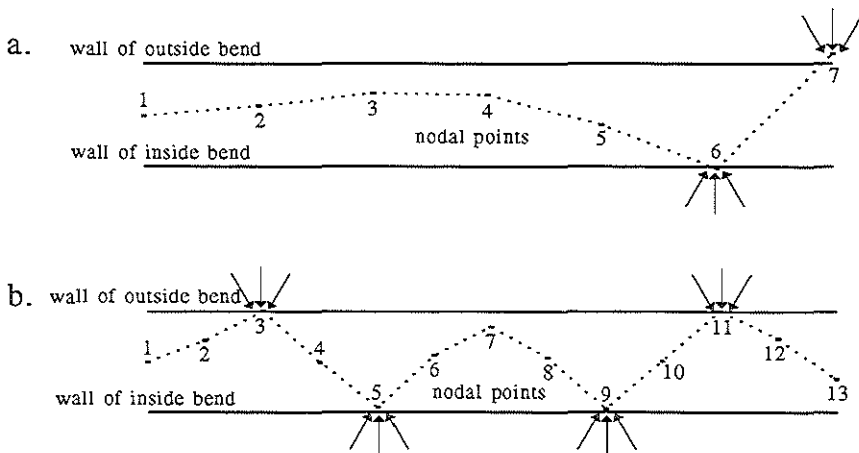


Fig. 4.2-9 Locations of contact between the SS-capillary drive-shaft and the inner wall of the catheter-tube, for a 90° curve with radius of 100 mm, according to FEM-results. Without straight ends (a: run c4) and with straight ends (b: run c6).

The lateral forces of the FEM are smaller than the predicted values of the analytical model, but they are of the same order of magnitude. The angle β is very similar for both models.

The stabilized geometry of the drive-shaft in the FEM shows its points of contact with the wall of the catheter-tube (Fig. 4.2-9). This also confirms the validity of the analytical friction model on a basic level.

Damping

In the FEM-calculations a damping in the drive-shaft deformation behaviour has been introduced to enable the model to find a stable solution after some time. A practical value for the damping has been chosen to serve this purpose, but has no relation to the energy loss of the drive-shaft in reality.

Combination of influences

The finite element method is pre-eminently suitable to study the combined effects of different influences on the drive-shaft running behaviour for well defined individual cases. In reality, however, some parameters occur with large deviation around a mean value, while others can only roughly be determined, because no adequate measuring method is available.

Extensive FEM-calculations using many different parameter combinations will reveal some tendencies and relationships.

Here the dealing with this issue is confined to the analytical modelling of § 4.1, illustrated by the following FEM-results.

Pre-curvature plus friction

The calculation runs b2 and b10 (pre-curvature) have been repeated, introducing a friction coefficient $\mu = 0.4$. The error angle of nodal point 4 has been monitored. In Table 4.2-6 the positive extreme value γ_{\max} is shown (the tip runs ahead) as well as the negative extreme value γ_{\min} (the tip runs behind). The theoretical values were obtained using the formulas of § 4.1.

The results are very similar and changes due to the addition of friction are in the same order of magnitude, but they are too small with respect to the accuracy of the models to draw more precise conclusions from this comparison.

Table 4.2-6 Extremes of rotation error angle γ [degrees] of nodal point 4, structure 1 (Fig. 4.2-1), determined by FEM and analytical model, for the combination of pre-curvature and friction, similar to runs b2 and b10 (pre-curvature), with friction coefficient $\mu = 0.4$.

	Analytical model no friction		Analytical model friction		FEM no friction run 2 run 10		FEM friction run 2 run 10	
	1000	200	1000	200	1000	200	1000	200
ρ_0 [mm]	1000	200	1000	200	1000	200	1000	200
γ_{\min} [°]	-9.8	-49.0	-10.5	-50.1	-9.2	-46.7	-9.7	-48.0
γ_{\max} [°]	9.8	49.0	9.3	48.8	9.0	45.3	8.5	45.4

§ 4.3 Experimental results

In § 4.1 the parameters have been introduced that rule the rotational behaviour of a flexible drive-shaft running inside a curved tube. In § 4.1 and § 4.2 analytical and finite element modelling have been presented to describe this behaviour. This paragraph will show some experimental results and the comparison with the analytical models.

Flexible drive-shaft test set-up

Functionality

The main experiments make use of a specially developed set-up to monitor the drive-shaft running behaviour by dynamic registration of the rotation error angle. This test set-up (Figs. 4.3-1 and 4.3-2) consists of a motor to drive the proximal end of the flexible drive-shaft, which is enclosed by a catheter-tube fixed in a suited geometry. On the distal end of the flex-shaft a small mirror is mounted in order to monitor the rotational motion of the tip optically (Fig. 4.3-2). This method is contactless and therefore does not introduce an extra (friction) load to the tip. The optical monitoring of the rotation angle makes use of a small diode-laser, which sends its light axially onto the mirror at the tip of the drive-shaft. The mirror deflects the light over 90° and by the rotation the light-beam is swept around. On a certain radius from the central axis the light meets with a code-cylinder, containing 200 equidistantly divided light absorbing lines, parallel to the axis and as many transparent lines. Around the code-cylinder a PMMA (plexiglass) pot is mounted, the

surface of which, facing the code-cylinder, is roughened in order to disperse the light into the PMMA body. Six photo-sensors, mounted circularly distributed on the distal flat side of the pot, register 200 light-pulses per revolution of the tip of the drive-shaft.

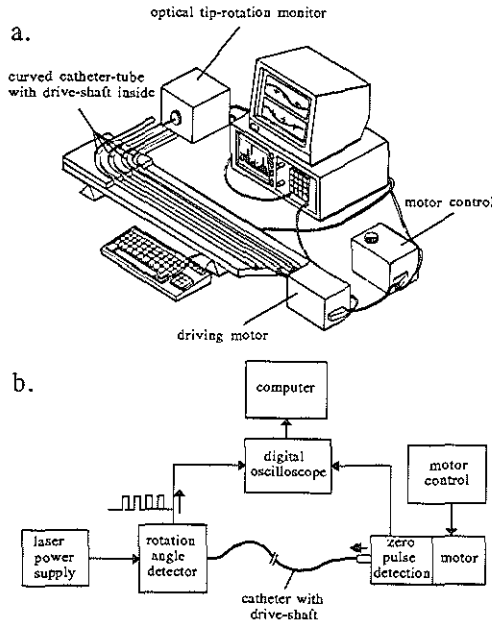


Fig. 4.3-1 Set-up for dynamic measurement of flexible drive-shaft rotation transmission. Overview (a) and structure (b).

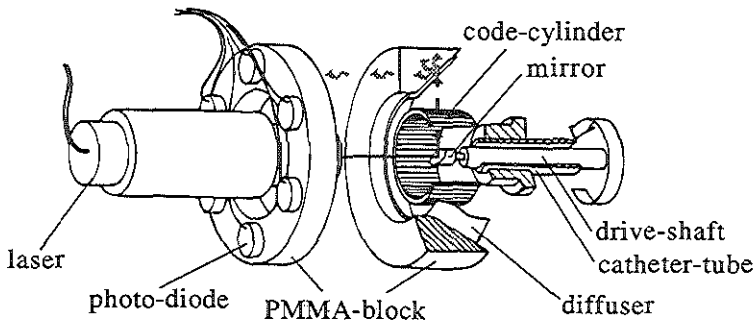


Fig. 4.3-2 Optical tip-rotation angle detection.

This configuration has several advantages over the set-up described in [5]. It allows for axial motion of the tip of the shaft with the mirror, as long as the deflected light-beam hits the spokes of the code-cylinder. This means that the tip of the drive-shaft does not need to be kept within narrow axial displacement limitations, which may introduce friction. Furthermore the laser, the code-cylinder, the PMMA pot and the photo-sensors make a solid-state set-up, so that disturbances of the measurement signal due to relative displacement of set-up components are minimized.

Geometry

The standard catheter geometry, used for the analytical modelling has also been applied in practice. The driving motor-shaft is attached to the flex-shaft, which has a long, proximal, straight part l_1 , in-line with the driving shaft. At the distal end a 90° curve with varying radii of curvature ρ_1 and curved length s_1 can be applied, which ends into a short straight part l' , leading to the tip-rotation angle measuring device.

The next thirteen catheter geometries have been investigated (Table 4.3-1).

Table 4.3-1 Catheter/drive-shaft geometry of test cases.

#	radius of curvature ρ_1 [mm]	proximal straight length l_1 [mm]	curved length s_1 [mm]	distal straight length l' [mm]
G1	15	1050	24	67
G2	40	1011	63	67
G3	70	963	110	68
G4	100	916	157	68
G5	∞	1141	-	-
G6	110	246	173	81
G7	150	185	236	79
G8	190	124	298	78
G9	110	225	173	97
G10	150	177	236	82
G11	190	118	298	79
G12	100	1042	157	--
G13	plexiglass models of catheter-track to coronary arteries (see Fig. 2.3-1)			

Determination of flexible drive-shaft properties

The measured deviation from uniform tip-rotation can be compared with calculated values, based on the analytical models. These calculations can only represent reality adequately when the relevant flex-shaft properties are known with high enough accuracy. For the determination of some properties special measurement procedures have been developed, that are described in Appendix F.

The relevant drive-shaft properties are:

1. bending rigidity EI [Nmm^2] (see Appendix F)
2. variation of the bending rigidity in accordance with the plane of deflection: p (see eq. 4-4 and Appendix F).
3. torsional rigidity S_t [Nmm^2] (see Appendix F)
4. friction coefficient μ (see Appendix F)
5. pre-curvature ρ_0 [mm] (see Appendix F)
6. drive-shaft mass per unit length m/L [g/m]

Four types of drive-shafts have been tested:

Type A: Stainless steel capillary

Type B: Double-layer spiral drive-shaft⁽⁵⁾, made from flat wire filaments:
0.075 x 0.125 mm

Type C: Double-layer spiral drive-shaft⁽⁵⁾, made from round wire filaments:
diameter 0.075 mm

Type D: Stainless steel wire

The properties of these shafts differ according to the type, but also individual differences may occur within one type. Therefore the relevant parameters of all tested drive-shafts have been determined individually (Table 4.3-2).

⁽⁵⁾Self-made flex-shaft: developed by the Erasmus University Rotterdam and produced at Du-MED B.V., Rotterdam.

Table 4.3-2 Properties of tested drive-shafts.

Type-#	OD[mm]/ ID[mm]	EI [Nmm ²]	S_t [Nmm ²]	μ^*	ρ_0 [mm]	p
A-1	0.50/0.25	559	425	-	1336	-
A-2	0.50-0.47/ 0.25	559	425	-	3240	0.042
B-1	0.86/0.50	9.8	116	0.24	300	-
C-1	0.77/0.45	1.6	132	0.14	50	-
C-2	0.80/0.45	1.2	53	0.14	64	-
C-3	0.79/0.45	1.3	96	0.14	67	-
D-1	0.472/--	480	363	0.20	-	-

*Kinetic friction coefficient of the shaft in a high density polyethylene tube.

Pre-curvature

Drive-shafts B-1, C-1, C-2 and C-3 have been tested in geometries G1 to G4. The tip rotation error angle θ has been recorded as a function of the proximal rotation angle $\psi_{\text{prox}} = \omega t$ (or as a function of the time t , while ω is constant) and as a function of the distal rotation angle ψ_{dist} . Measurement data have been recorded for both driving directions: clockwise and counter clock-wise (clockwise is defined as a rotation to the right, looking towards the distal tip).

According to eq. 4-11 the function $\theta(\psi_{\text{dist}})$ represents a sine-function, whereas the function $\theta(\psi_{\text{prox}})$ shows a phase-shift of the extremes, equal to the amplitude itself. On the functions $\theta(\psi_{\text{dist}})$ a sine fit has been applied, based on minimizing the root-mean-square of the residuals. In all cases a reasonable to very good fit could be accomplished, yielding an accurate estimation of the amplitude of the periodic error angle. Model values of all cases have been calculated using eqs. 4-14 and 4-16, the drive-shaft properties and geometrical parameters, given in Tables 4.3-1 and Table 4.3-2. The two determinations of the periodic error angle due to pre-curvature are compared in Fig. 4.3-3.

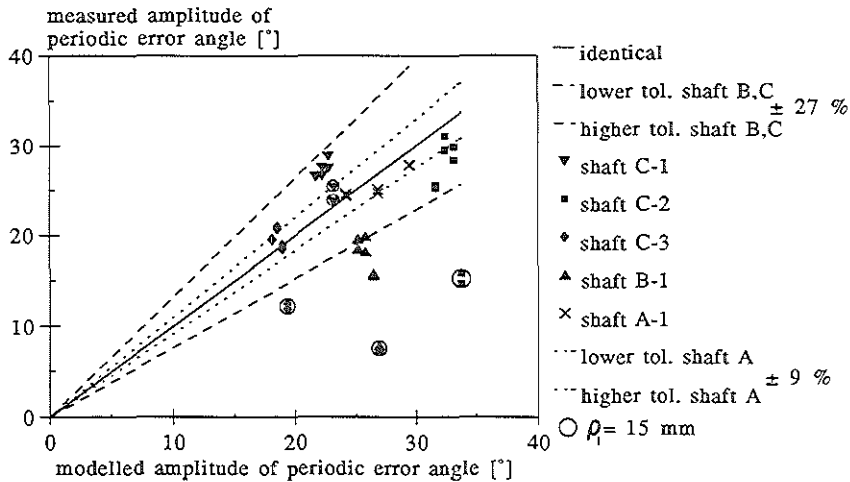


Fig. 4.3-3 Measured values of the amplitude of the periodic error angle, in comparison with results obtained from the analytical model, in case of pre-curvature.

Because of the difficulty of accurate measurement of the drive-shaft parameters for these very flexible drive-shafts (see Appendix F), a large tolerance zone around the line of identity exists of $\pm 27\%$ (dashed lines). This represents the inaccuracy of the model values on the horizontal axis (e.g. the pre-curvature ρ_0 could be determined with a 12 % error, and the bending rigidity EI suffers an inaccuracy of 10 %).

According to eqs. 4-14 and 4-16 it is to be expected that for increasing radius of curvature ρ_1 , but constant angle φ_1 , (geometries G1 to G4) only a very slight decrease of the amplitude of the error angle will occur, due to small changes in the values for s_1 and l_1 . Furthermore, the model does not anticipate different results for both driving directions and indeed most couples of data-points (representing both driving directions) are situated close together on a vertical line. All data points collected from one drive-shaft should therefore be close together. And indeed they form clusters in Fig. 4.3-3, except from a few points that also drop out of the tolerance zone. These points represent measurements, all performed at small radii of curvature (geometry G1: $\rho_1 = 15$ mm, encircled data points).

For these points the measurements do not agree with the model, because the model is based on purely linear elastic material behaviour. At small radii of curvature ($\rho_1 < 55$ -70 mm) the drive-shaft undergoes some plastic deformation, so some of the pre-curvature will be lost and the actual radius of pre-curvature becomes larger than the value of Table 4.3-2. A lower amplitude of the periodic error angle will be the result.

This behaviour for the shafts B-1, C-1 and C-3 has been proved by bending an originally straight section of these shafts with a curvature $\kappa_{\text{appl}} (= 1/\rho_{\text{appl}})$ and determining the remaining curvature $\kappa_{\text{pl}} (= 1/\rho_{\text{pl}})$ after release (Fig. 4.3-4).

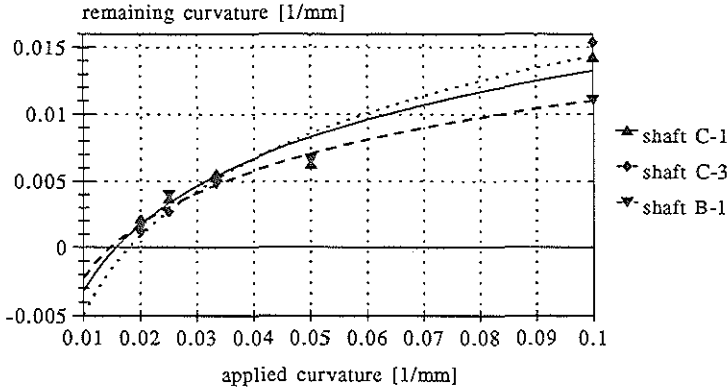


Fig. 4.3-4 Plastic deformation of flexible drive-shafts.

The lines in Fig. 4.3-4 represent the fit of a logarithmic curve for every shaft. This way a purely elastic deformation is predicted, defined by the intersections of the curves with the horizontal axis. For values of the applied curvature: $0.014 \text{ mm}^{-1} < \kappa_{\text{appl}} < 0.018 \text{ mm}^{-1}$, the purely elastic limit is reached; the minimum radius of curvature, not causing any plastic deformation, ranges from 55 to 70 mm.

The assumption of a logarithmic curve to describe the relationship between the applied and the plastic deformation (in the chosen data range) is fundamentally deviating from the behaviour of a stainless steel wire. In the latter case the contribution of plastic deformation to the total applied deformation will increase with growing total applied deformation. The lines in Fig. 4.3-4 show the opposite. A cause for this behaviour should be found in the structure of the double-layer spiral. Extensive modelling of this structure, with respect to its flexural and torsional behaviour, may yield more understanding of the interesting properties of the double-layer spiral flexible drive-shaft. This modelling lies outside the scope of this thesis.

The occurrence of plastic deformation at small radii of curvature causes energy dissipation in the shaft, which requires a driving torque and thus causes a constant rotation error angle component.

A more accurate comparison between the model and measured values can be made, testing stainless steel capillary drive-shaft A-1 (Table 4.3-2) in geometries G6 to G8, for both driving directions. The inaccuracy of the model values is limited to $\pm 9\%$ (dotted lines in Fig. 4.3-4). All six data-points (x) are situated within the tolerance zone. The measurements confirm the validity of the model for linear elastic drive-shaft behaviour.

Unequal bending rigidities in different bending planes; $EI_y \neq EI_z$

Verification of this aspect of the model has only been performed using SS-capillary shaft A-2 in geometries G9 to G11. It appeared to be impossible to modify a double-layer spiral drive-shaft in such a way that a constant and accurately measurable difference of bending rigidity in two perpendicular planes of bending would be present over a certain length of the shaft.

By carefully rolling the SS capillary over a certain length, its thickness in the direction of compression was reduced from 0.5 to 0.47 mm, while its dimension in the perpendicular direction was hardly affected. The rolling activity, however, inflicted a slight pre-curvature onto the capillary, with $\rho_0 \approx 3200$ mm. From many measurements of the bending rigidity in both perpendicular planes, the p -value (eq. 4-4) has been determined with reasonable accuracy: $p = 0.042 \pm 5\%$.

Both effects were clearly present in the measurement signal of the tip rotation error $\theta(\psi_{\text{dist}})$. The signals have been processed by performing a sine-fit, with a frequency equal to the driving rotation frequency. This shows the effect of the pre-curvature. The residuals show a clear sine function with twice the driving rotation frequency, which is the expected effect of the difference in bending rigidity (eq. 4-9). The amplitudes of the tip-rotation error due to both causes have been determined and a comparison with the theoretical models (respectively eqs. 4-16 and 4-9) is depicted in Fig. 4.3-5. The inaccuracy of the calculated values according to the models is $\pm 15\%$ for the pre-curvature (the error in ρ_0 is already $\pm 10\%$) and $\pm 10\%$ for the unequal bending rigidity in different planes (the error in p is $\pm 5\%$).

According to Fig. 4.3-5 the measured values and the model calculations correspond very well. The combined effect of pre-curvature and unequal bending rigidity consists of the one superimposed onto the other.

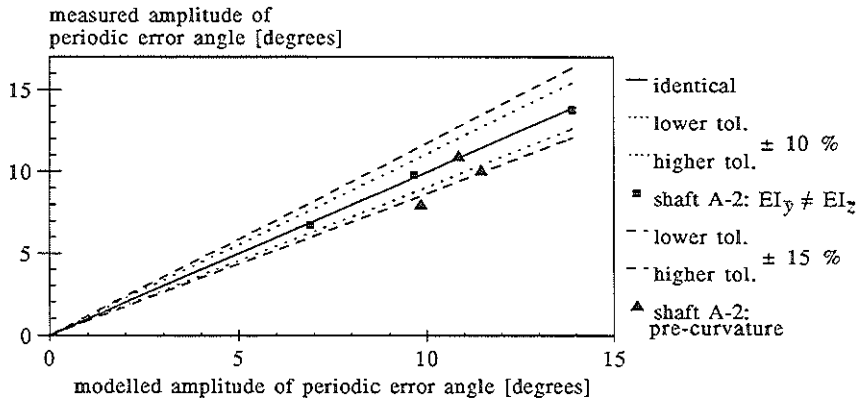


Fig. 4.3-5 Measured values of the amplitude of the periodic error angle, in comparison with values obtained from the analytical model, in case of pre-curvature ($\rho_0 \approx 3200$ mm), combined with $EI_y \neq EI_z$ ($p = 0.042$).

Friction

Measurements of the constant tip-rotation error angle, performed on the double-layer spiral drive-shafts, either wound from flat or round wire (Type B respectively C), don't give results that confirm the validity of the analytical model, describing the friction between the shaft and the catheter-tube wall. The measured drag of the tip is much larger than the predicted model values. After correction for friction caused by gravity and by the non-straight, wavy geometry of the free shaft, which cause friction even in the straight section of the shaft, still less than half of the measured error angle is accounted for.

Fig. 4.3-4 shows the tendency of these shafts to plastic deformation at practically used radii of curvature. While rotating a strongly curved shaft at an angular velocity ω , energy is dissipated in the drive-shaft. This requires the presence of a driving torque T ($T \cdot \omega =$ energy dissipation), which is assumed to be responsible for the remaining error angle.

Analysis of this phenomenon would require modelling of the properties of the double-layer spiral drive-shaft as a result of its structure, which will not be presented here.

Drive-shaft D-1 (Table 4.3-2) consisting of a stainless steel wire has better linear elastic bending characteristics and therefore yields better matching results. Measurements have been performed using geometry G12 and a high density polyethylene tube with an inner diameter of 0.559 mm. The clearance c therefore is 0.087 mm. The friction coefficient μ has been determined to be 0.20, using the measurement method described in Appendix F.

According to eq. 4-21 the theoretical constant rotation error angle is $11.1^\circ \pm 10\%$. The measured drag in the set-up of Fig. 4.3-1 is $10.9^\circ \pm 10\%$. This shows a perfect match.

Practical catheter use

In order to get an idea about the rotation error angles, occurring during practical coronary catheterization, a plexiglass tube, curved according to the practical catheter-track (see Fig. 2.3-1) has been built into the set-up of Fig. 4.3-1, in between the driving motor and the optical tip-rotation monitor. Through the lumen of the plexiglass tube a catheter-tube has been advanced. The catheter-tube encloses a flexible drive-shaft of type C (Table 4.3-2), which is driven.

It has been shown that for good quality shafts of this type ($EI \approx 1.5 \text{ Nmm}^2$, $S_t \approx 100 \text{ Nmm}^2$ and little pre-curvature), the constant error angle is in the order of 10° and the peak-to-peak periodic error angle is $< 20^\circ$. Stochastic errors will stay within 1° .

Considering the requirements, defined in § 3.1, this flexible drive-shaft may well be suitable.

§ 4.4 Conclusions; flex-shaft specifications

General conclusions

The comparison of the values of the rotation error angle, obtained from the analytical modelling, the numerical FEM-calculations and the practical measurements, shows a high degree of similarity for the simple cases that have been investigated, as long as linear elastic material behaviour is maintained.

On the one hand this means that the analytical models represent a strong tool to help understand the influence of different parameters on the resulting rotational behaviour of the drive-shaft. On the other hand the finite element model may show to be a reliable tool to describe the running behaviour in more practical cases, where all influences together cause a combined effect on the running behaviour and the geometry becomes too complex to be described by the analytical models.

Drive-shaft and catheter design

The modelling of the drive-shaft rotational behaviour has yielded a few design criteria to optimize the performance of the shaft.

- For all three main influences, causing a rotation error angle, their effect has been found to be proportional to the factor EI/S_t . Minimizing this ratio will improve the drive-shaft running behaviour (compare Fig. 4.1-4a, b and c). For the SS-capillary drive-shaft $EI/S_t = 1.32$ and for the double-layer spiral flex-shaft type C (Table 4.3-2), $EI/S_t = 0.015$, which means an improvement of about factor 90.
- This double-layer spiral drive-shaft type C, curved in a geometry similar to the catheter-track in practical coronary catheterization, performs in accordance with the requirement of § 3.1.
- Pre-curvature may be the most important reason for bad drive-shaft performance. It is therefore necessary to produce straight drive-shafts that are not easily deformed plastically, either during catheter assembly handling or clinical use, so that pre-curvature will not be induced later. A purely elastic bending behaviour down to the very small practical radii of curvature is expedient. If pre-curvature occurs anyhow, a small value of the ratio EI/S_t will restrict its effect on the rotation error angle.
Also a drive-shaft configuration with no elastic behaviour at all in bending mode (chain of beads) overcomes the problem of pre-curvature.
- The clearance c of the drive-shaft in the catheter-tube should be large enough not to cause too much friction. The torque due to friction and the resulting error angle are proportional to $1/\sqrt{c}$ (eqs. 4-18, 4-19 and 4-20, 4-21).
A special tip bearing construction, with small clearance, may yield a better definition of the axis of rotation of the catheter-tip. However, under curved conditions, it will cause substantial friction and should therefore be avoided.
- Friction hardly plays a role in causing a periodic error angle, even in combination with $EI_y \neq EI_z$ and pre-curvature. Its effect mostly is a constant drag, which increases for smaller ρ_1 and c and higher μ . For application under severely curved conditions ($\rho_1 \approx 15$ mm for coronary use) the described flex-shaft type II is suitable, as far as friction is concerned (Fig. 4.1-4c), when used in the described catheter-tubes (Table 4.2-1 and § 4.3).
- Gravitation may start to play a role (error angle in the order of several degrees) for ultra-flexible drive-shafts with $EI/S_t \approx 0.015$ if $S_t < 20 \text{ Nmm}^2$ and a mass of 2 g/m . It should be taken into account when developing smaller diameter drive-shafts or other types of drive-shafts than the double-layer spiral version.
- If the material behaviour of the shaft is not purely elastic, but also plastic deformation will occur, the constant component of the rotation error angle will increase and cannot be explained entirely by the friction model. This phenomenon seems to occur for the double-layer spiral drive-shafts.

High torque catheter and guide-wire design

The modelling of the drive-shaft rotational behaviour also reveals design criteria for "high torque" catheters and guide-wires. These are designed to facilitate manipulation of the tip in the required rotational position by rotating the proximal side of the catheter or guide-wire. High fidelity transmission of a uniform rotation is not required. But all tip-rotation angles should be attainable and stable. In case $EI_y \neq EI_z$ and $\rho_0 \neq \infty$, stability will not be maintained if the requirements, expressed in eqs. 4-10 and 4-17 are not being met. The quantities A and B in these formulas are determined by catheter or guide-wire characteristics and their geometry in practical use (eqs. 4-3 and 4-12).

These criteria are hardly applicable to drive-shaft design, because much higher demands are made to their rotational behaviour.

References

1. Timoshenko S.P., Gere J.M., Mechanics of Materials, Van Nostrand Reinhold Company, International Student Edition, p. 562, 1973.
2. Martin R.W., Johnson C.C., Design characteristics for intravascular ultrasonic catheters, Int. J. Cardiac. Imag. 4: 201-216, 1989.
3. Bosma R., Beknopte samenvatting van het Kollege Tribologie, Collegedictaat, Technical University Twente, 1967, correction 1976.
4. Heijningen G.J.J. van, Tribotechniek, deel B: Zelfwerkende vloeistoffilms, Collegedictaat, Technical University Delft, 1987.
5. Hoff H. ten, Korbijn A., Smit Th.H., Klinkhamer J.F.F., Bom N., Imaging artifacts in mechanically driven ultrasound catheters, Int. J. Cardiac Imag. 4: 195-199, 1989.

CHAPTER 5 Correction for non-uniform catheter-tip rotation.

§ 5.1 Indications for application

In the previous chapter the performance of a flexible drive-shaft in a curved catheter-tube has been described in terms of rotation transmission fidelity. It has been shown that a low value of the ratio bending rigidity/torsional rigidity is beneficial to its behaviour, as is the only scanty presence of disturbing influences like pre-curvature, unequal bending rigidities in different bending planes and friction.

It has also been shown that a well-constructed double spiral flexible drive-shaft in a catheter-tube, following the tortuous pathway from the introduction site at the femoral artery to the coronary artery (see Fig. 2.3-1), can perform adequately, so that useful images of this blood-vessel will be obtained.

Some distortion of the image, although mostly little, will always be present. The clinical value of the images depends on the desired information to be extracted from them, varying from a qualitative impression of the local blood-vessel geometry to accurate quantitative analysis of the rate of stenosis, the open lumen, intima thickening, etc. In the latter cases image distortion will affect the accuracy with which these parameters can be determined, so that an image correcting system may be helpful.

Furthermore, in some specific applications of the echo-imaging catheter the high fidelity rotation transmission may no longer be maintained, so that special measures have to be taken to reduce the image distorting effect of the non-uniform rotation of the US-beam.

In purely diagnostic applications the need for extra long catheters and extremely curved catheter geometries (coronary use) may be indications for the implementation of an image correcting system. It should be emphasized here that a very small catheter-tip diameter (≤ 1 mm) may be required to be able to investigate deep enough into the coronary arterial system. The implemented system to reduce image distortion should allow for down-scaling to this size.

If the US-diagnostic system is combined with a desobstruction method, which delivers (part of) the energy needed for recanalization through the same flex-shaft rotation, the echo-tip rotation will be affected by the (friction) load at the tip. If simultaneous imaging and deobstructive action is required, implementation of a system to reduce or correct for image distortion may be necessary.

§ 5.2 Methods

§ 5.2.1 Reduction of rotary speed in the catheter-tip

A speed-reducing mechanism at the tip of the flexible drive-shaft is only proposed here as one of the alternatives. Its possibilities have not been fully analyzed and development nor prototyping have been performed. However, present developments in the creation of micro-mechanical structures, based on silicon technology or the LIGA-method, contribute to the confidence in the producibility of the proposed device in the required small dimensions.

During uniform driving motor rotation, the rotation angle ψ_{prox} of the proximal side of the flex-shaft is:

$$\psi_{prox} = \omega t \quad (5-1)$$

The expression for the rotation angle ψ_{dist} of the distal side of the flex-shaft, including the occurrence of a periodic error angle θ is:

$$\psi_{dist} = \omega t + \theta = \omega t + \theta_0 \sin(\omega t + \varphi) \quad (5-2)$$

If a speed-reduction ratio r is achieved at the tip, the rotation angle ψ_{US} of the US-beam is:

$$\psi_{US} = \frac{\omega t}{r} + \frac{\theta_0}{r} \sin(\omega t + \varphi) \quad (5-3)$$

In order to accomplish real-time imaging and to avoid image deformation due to the catheter motion in a physiologically moving blood-vessel, the minimum rotation speed of the US-beam is about 1000 rpm. The driving speed in that case is a factor r higher. The amplitude of the periodic error angle θ_0 is basically not sensitive to the average rotation speed (Chapter 4), so that a reduction of the periodic error angle of the US-beam rotation with factor r will be achieved by the implementation of an rotary speed-reducing device.

However, if the considerably higher driving angular frequency is close to the fundamental frequency of a freely moving drive-shaft section in torsion-mode, the error angle amplitude will be amplified (§ 4.1: "Fundamental frequency and inertia"). This should be carefully avoided.

§ 5.2.2 Angle detection systems

Principles of image correction by means of angle detection

The extent of non-uniformity of the rotation at the catheter-tip is strongly dependent on the exact geometry of the catheter in the practical situation (see Chapter 4). Therefore it is impossible to predict its running behaviour according to a calibration test in a phantom outside the patient's body, just prior to clinical use. Once the need for image correcting means is established a dynamic, built-in correcting system, influencing or monitoring the catheter-tip rotation is required.

Correction of the image, with the use of actual information on the tip-rotation angle can be performed in two ways.

In the first method the angle detection signal can be used to measure or estimate the traversed angle between two successive directions of the US-pulse, emitted at equal time intervals. This information can be fed to the display processing, for correct positioning of the corresponding image-lines. However, the tangential resolution, becomes dependent on the rotation angle, which diminishes the image quality (Fig. 5.2-1a).

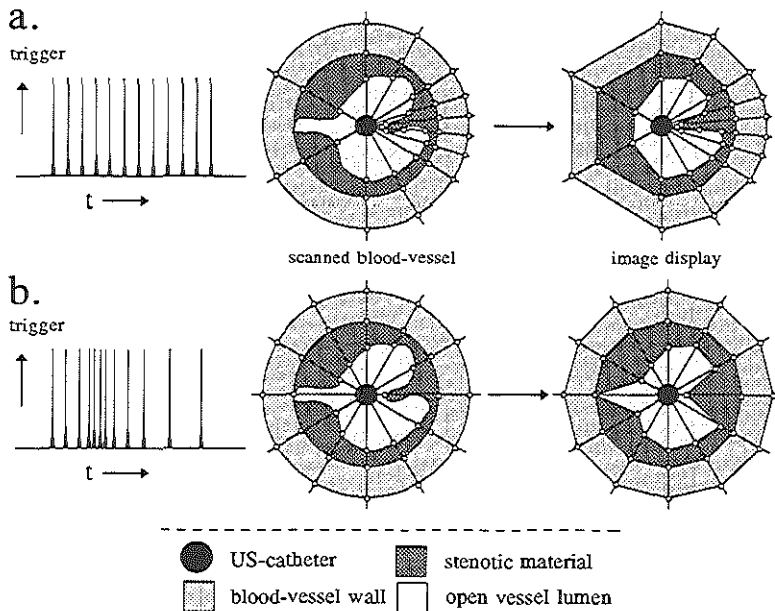


Fig. 5.2-1 The image correction method of displaying image-lines, generated equally spaced in time, at their right angular positions, results in rotation angle dependent tangential resolution (a). Tangential resolution is not affected, when image-lines are collected at equal angle increments (b).

In the second method the angle detection signal can be used to trigger the emission of US-pulses at equal traversed angle increments, so that image-lines are not generated periodically. Display of the image-lines then is straight forward (Fig. 5.2-1b).

Physical principles of angle detection

Acoustic

In the search for an adequate principle for angle detection of the tip-rotation of an US-imaging catheter it is obvious to consider an acoustic approach. In this case the US-system itself should be equipped with means to detect the angular position of the rotating tip. Unfortunately this option shows to be less self-evident as may be thought at first sight.

US-reflecting structures, equidistantly positioned around the rotating transducer, may be detected and thus define several angular positions of the catheter-tip. However, specific requirements are made to these reflecting structures and their position in the dome. For obvious reasons the reflecting structures should not be positioned in the "dead zone" around the transducer (see Fig. 2.2-4). If the catheter-tip configuration of Fig. 2.2-3a is applied in a 1.73 mm OD (French Size 5.2) catheter, it extends nearly to the dome. On the other hand positioning the structures too close to or even in the dome-material causes the reflection signals to coincide with the unavoidable reflections of the dome-material boundaries, that already saturate the amplifier.

Furthermore, multiple reflection and shadowing should be avoided, not to disturb the image-field and by doing so, lose vital information of the imaged blood-vessel.

Very thin round wires (of about 10 μm OD; much smaller than the US wave-length), placed parallel to the catheter axis on a suitable radius around the rotating transducer could be used as reflecting structures. But they should be held there by means, "invisible" to the US-transducer and yet providing mechanical protection against the rotating transducer-head.

A step-structure in e.g. the dome-material, with a step of half the acoustic wave-length (at 30 MHz i.e. 25 μm), will cause destructive interference of the reflecting signal and provides a way for acoustical rotation angle detection. However, an adequate step-structure will not easily be made into the sonolucent dome-material (a polymer: PE or TPX).

Multiple reflection of the code-reflectors may not be so problematic if the reflectors are placed just proximal to the imaging window and the drive-shaft-transducer-assembly can be adjusted axially either in imaging-mode or in angle-detection-mode. This will work only under the assumption that the drive-shaft rotation behaviour will hardly change by this very small axial displacement. But it remains necessary in any case to re-calibrate the system after every change of the catheter geometry.

Another draw-back of an acoustic solution is its low resolution. The reflectors are situated in the near-field of the US-transducer, which has an outer diameter of 1 mm. Therefore the US-beam-width, when interacting with the reflectors, is also about 1 mm and the intensity profile is erratic. In a 5.2 French catheter (1.73 mm OD) not more than 10 to 20 reflectors may be separately identified in one revolution. For smaller catheter sizes this number will decrease.

Capacitive

A capacitive angular position sensor can be developed, where either the gap-size between two capacitor plates or their overlapping area changes with the rotation angle. The method will yield a weak analogue signal from which the angular position can be deduced with poor resolution. Extra concern should be given to shielding against disturbing influences. The location of the sensor in the catheter-tip, close to the US element, may show to be problematic in this respect.

Electro-magnetic

An electro-magnetic micro-motor, as described in Chapter 3, can also be used as a generator of an AC-current. It can be built into the catheter-tip, between the flexible drive-shaft and the driven US-element or rotating mirror. From the phase of the sinusoidal signal the rotation angle can be found.

Optical reflection

An optical fiber, incorporated in the catheter is led to a code-disk with reflecting lines, at the catheter-tip. Light transmitted through the fiber core reflects on the code-disk lines and partly re-enters the fiber, so that the reflection signal can be monitored at the proximal end of the catheter. Either the optical fiber is incorporated in the flexible drive-shaft and the code-disk is stationary, or the fiber runs through a catheter-lumen and the code-disk is driven together with the US-transducer or acoustic mirror. This way the catheter-tip rotation is defined by the reflection signal.

An elaborate account of a first approach development effort to realize a high resolution angle detection system, based on this principle, is presented in § 5.3.

In § 5.3.4 the deficiency of this system is discussed, together with recommendations for a more promising design.

§ 5.3 High resolution optical angle detection system; a first design approach

When this development started, not much was known about the rotational behaviour of a flexible drive-shaft in a curved catheter tube (Chapter 4). But it was known that it would be difficult to design and construct a flex-shaft with high fidelity rotation transmission for reliable imaging in tortuous blood-vessels. Therefore, in this early stage of the project, an angle detection system was considered to be the effective solution [1].

This paragraph describes the learning process of the many aspects of the optical angle detection system, varying from basic design mistakes to manufacturing methods of components. Six catheter prototypes were built, but none of them was fully functional.

§ 5.3.1 System requirements

Many of the general characteristics and requirements of intravascular ultrasound imaging have been described in Chapter 2. Some specific requirements with respect to the angle detection system will be given here.

Dimensions

The US-transducer and angle detection system were built into a 5.2 French (1.73 mm OD) CORDIS angiography catheter. The wall of this catheter tube contains a stainless steel braiding, which is grounded as an additional shielding against electro-magnetic interference. The presence of the braiding determines the wall thickness, yielding a maximum available inner diameter of 1.14 mm, which in turn determines the maximum outer diameter of the drive-shaft.

Resolution

Presuming that the rotational behaviour of the tip was unpredictable, apart from its average rotary speed, which equals the speed of the driven proximal side of the shaft, all the image accuracy would depend on the angle detection system. An important requirement was thought to be a high angular resolution, because the angle detection should provide all the image reliability the flex-shaft could not guarantee. At the time, we were imaging in an in-vitro set-up with 500 image-lines per revolution. So to meet this image-quality an angular resolution of 0.7° would be required. This resolution showed to be too high for the chosen technology, so that a compromise of 2.3° angular resolution was used. The achievement of better flex-shaft characteristics and more understanding of its behaviour justify a lower resolution (§ 5.3.4).

Catheter use and patient safety

- The rotating tip of the catheter should not be able to damage the inner wall of the blood-vessel and therefore is covered by a dome. This dome should be made of a material that causes a minimum of reflection and attenuation of the ultrasound. The polyurethane of the catheter tube is not suited for this purpose.
- For hygienic reasons the catheter should be for one-time-use only, designed as a disposable, so expensive components should be avoided.
- For other general catheter characteristics see § 2.3.

Drive-shaft

- For easy introduction into tortuous blood-vessels, the drive-shaft should not add considerably to the over-all flexural rigidity of the catheter. The catheter-tube which we have used in this development has a flexural rigidity of about 170 Nmm². The rigidity of the shaft should be one order of magnitude lower.⁽¹⁾
- The rotation transmission characteristics of the drive-shaft, in terms of tip-rotation error angles and tip-velocity changes, should allow for correction. Too much deviation from uniform tip-rotation gives rise to problems concerning "the fire-hose effect" and data acquisition (see § 3.1).

This means that:

- * The shaft should possess a low enough ratio bending rigidity/torsional rigidity (Chapter 4).
- * The over-all diameter of the drive-shaft should leave enough clearance in the catheter-tube, to restrain friction. From practical observations, using the described catheter-tube with an inner diameter of 1.14 mm, a maximum tolerable outer diameter of the shaft of less than 0.9 mm could be found.
- The shaft should be suited for real-time imaging (rotation speed up to 1000 rpm) in curved vessels (radius of curvature down to 20 mm). These conditions require high fatigue-resistance of the shaft.

Fluid-filling

The catheter-tip should be filled with a fluid (§ 2.2). The angle detection system should function under these conditions.

Connection to driving unit

The disposable catheter has to be connected to a non-disposable driving unit, which in turn is connected to the system main-frame (Fig. 2.4-1). All functional connections (mechanical,

⁽¹⁾ As a comparison, the stainless steel capillary drive-shaft, used for prototyping, OD 0.5 mm, ID 0.25 mm, has a flexural rigidity of 575 Nmm².

electrical and optical) between the catheter and the driving unit should be established easily and reliably, by "plugging in" the catheter connector. Especially the driving unit side of the connector should guarantee proper connection for many times.

§ 5.3.2 Design-structure

The optics design allows for two options: a rotating optical fiber, incorporated in the flex-shaft, communicating with a stationary code-disk or a shaft-driven code-disk combined with a static fiber.

The first concept has been chosen. A concentric structure is preferred, in order to maintain equal bending rigidity in all planes. This is beneficial to the catheter's behaviour during introduction and advancement into the arterial system. Furthermore the second concept needs a costly custom-made extrusion to obtain a complex two-lumen catheter-tube, one for the drive-shaft and one for the optical fiber.

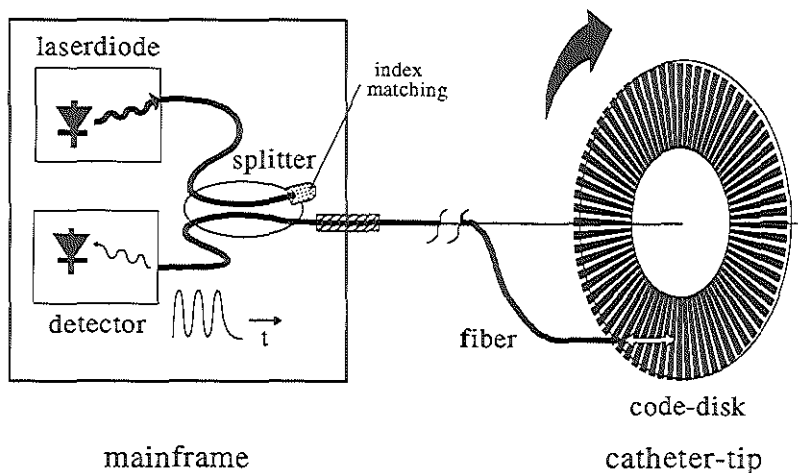


Fig. 5.3-1 Structure of the opto-electronical angle detection system.

The structure of the first concept can be seen in Fig. 5.3-1. A light-source mounted on a rotating PC-board emits light into an optical fiber which is connected by the catheter connector to the fiber running through the catheter drive-shaft. At the tip the fiber is bent away from the centre to face the radial reflecting lines of the static code-disk. The drive-shaft itself is extended beyond the code-disk, where an ultrasonic transducer is attached to it. Reflected light from the code-disk will be coupled into the same fiber again and transmitted to the proximal end. It passes the connector and is split off into another fiber by a beam-splitter. This fiber leads to the optical detector.

§ 5.3.3 System design and development

The most important components of the described optical angle detection system are the light-source, the optical fiber, the code-disk and the flexible drive-shaft assembly. The first two items were available on the market. The code-disk and the drive-shaft, however, had to be custom-made for our application, leading to a study of the optimal performance and production process.

Light-source and detector

In the first approach to obtain a high resolution angle detection system a 3 mW laser-diode, wavelength 780 nm, in combination with a single-mode (SM) optical fiber has been investigated. For easier application in the system a "pig-tailed" version is chosen, meaning that an optical fiber already has been connected to the laser by the manufacturer. The laser has been provided with a monitor diode to help controlling the lasing-stability.

In one of the early stages of the development a special designed pig-tailed laser-diode with strong sensitivity for external reflections entering the cavity from the outside world was used. The aim of these experiments was to investigate the possibility of using the built-in monitor diode to detect external reflections coming from the code-disk. Unlike shown in Fig. 5.3-1, a separate detector with a beam-splitter would than become redundant.

The current of the monitor diode indeed showed modulation features caused by external reflections. However, these features had to be detected against the lasing intensity emitted from the rear facet of the laser-diode, resulting in very low contrast. Therefore it was decided not to exploit this detection scheme any further.

In a new set-up a pig-tailed laser-diode with low sensitivity for external reflections has been used. A separate detector for detection of the light reflected from the code-disk, combined with a fiber-optic splitter has been applied, in accordance with Fig. 5.3-1. This configuration however creates an unbalanced Mach-Zehnder interferometer, which by nature is very sensitive to phase differences in the recombining signals, being reflected from the fiber end-faces of the two respective output ports of the splitter.

In the situation of the catheter drive-shaft, the difference in length between the fiber in the shaft itself (being illuminated by one output port of the splitter) and the other port (being the end of the fiber coming from the laser-diode) is shorter than the coherence length of the laser-light, giving rise to the interference effects mentioned. These effects can be partly eliminated by index matching of the second output port of the splitter, thus preventing reflections (Fig. 5.3-1).

To avoid implementation of an optical rotational connector-joint, which for single-mode application should guarantee highly accurate alignment ($< 1 \mu\text{m}$), the laser and detection diode are mounted on a rotating PC-board and electrical connections are made through slip rings.

In the next section, it is outlined that the use of monochromatic coherent light can result in signal fluctuations caused by interference. Abandoning the concept of the single-mode fiber in favour of the multimode (MM), the need for the use of a laser disappears, so that a simple light emitting diode can be implemented.

Optical fiber

The general concept of fiber optics and the different types of optical fibers are described in [2]. For a better understanding of the design considerations concerning the use of an optical fiber in our catheter design, some basic theory has been summarized in Appendix G.

Application of a single-mode fiber

In an early stage of the development we have been using a single-mode optical fiber for our catheter application, assuming that the small fiber-core would be necessary to obtain a small enough light-spot in front of the fiber, without the use of a costly lens, to detect every single, very narrow reflecting line on the code-disk (width $13 \mu\text{m}$ at 78 lines).

The standard single-mode fiber, designed for an operational single-mode wave-length of 1300 nm for use in telecommunication, has a jacket with an outer diameter of $250 \mu\text{m}$. A number of design constraints however make this fiber unfit for application as central element of the drive-shaft. Necessary minimum thickness of copper wires and dielectric layer demand a thinner optical fiber, considering the maximum over-all outer diameter of the drive-shaft. Later in this paragraph it is also shown that a fiber with a thin hard material jacket, unlike the one mentioned above, is preferred to avoid mounting problems.

A solution has been found in a fiber, 7/80/133 μm (core/cladding/jacket), available for sensor applications, having an operational wave-length of 850 nm, with a single-mode cut-off wave-length of 780 nm.

An experimental angle detection system accommodating the single-mode fiber, which interrogates a rotating code-disk (Fig. 5.3-1), has performed quite well under idealized conditions, but built into a complete catheter-system important draw-backs have been revealed.

The small core size of a single-mode fiber, combined with a certain numerical aperture (e.g. N.A. = 0.1, $\beta = 5.7^\circ$) allows only very little distance between the fiber-tip and the code-disk surface to enable the reflected light to re-enter the narrow core of the fiber (Fig. 5.3-5a). Experiments have shown that this distance should be smaller than $45\text{ }\mu\text{m}$ (Fig. 5.3-2), which turns out to be very difficult to realize in the catheter-tip, also considering the fact that the defined distance includes the necessary axial clearance of the bearing.

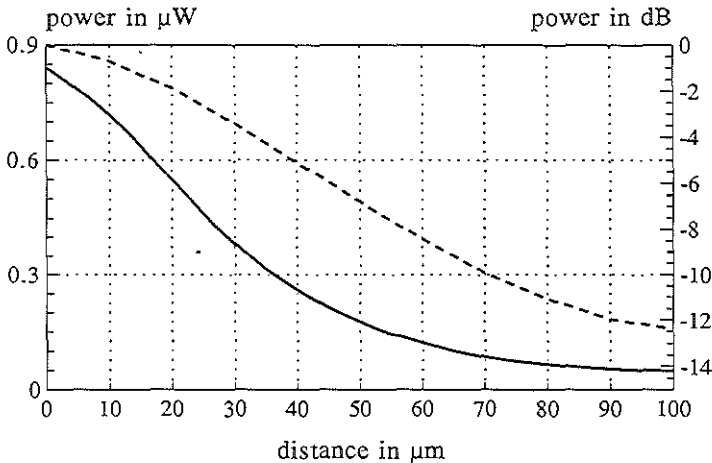


Fig. 5.3-2 Power of the reflection signal in μW (—) and in dB (---), as a function of the distance between fiber-tip and code-disk, for a single-mode fiber [3].

For single-mode fibers (typical cladding diameter of $80\text{ }\mu\text{m}$) hardly any standard help and handling materials are available. Coupling of these fibers for instance without using standard ferrules is not an easy task and is only to be performed by specialists. The cores of two single-mode fibers should be very well aligned (within $1\text{ }\mu\text{m}$) to minimize the loss of power caused by the coupling.

This problem will even be bigger in the optical connector between the catheter and the driving unit. Such a connector should be able to place the ends of the single-mode fibers accurately opposite to each other by simply plugging in the catheter connector. The optical connector at the side of the driving unit should guarantee this proper aligning for many times.

For multimode fibers (standard cladding diameter $125\text{ }\mu\text{m}$) a large number of inexpensive devices are on the market, because of the extensive use of these fibers in telecommunication.

The connector problem mentioned above may be solved therefore by permanently coupling the $80\text{ }\mu\text{m}$ single-mode fiber of the catheter to a piece of $125\text{ }\mu\text{m}$ multimode fiber in the body of the catheter connector (Fig. 5.3-3).

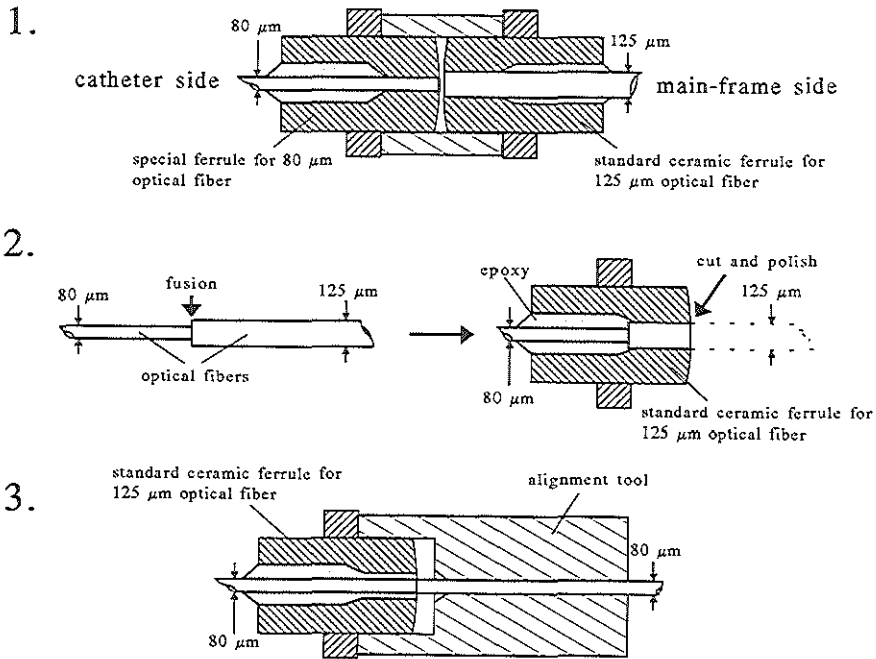


Fig. 5.3-3 Coupling methods of single-mode fibers.

An optical connector for 125 μm cladding diameter (multimode) can then be incorporated in the catheter connector. Alignment of these multimode fibers is much less critical and is therefore much easier to maintain within specifications over a large number of connecting/disconnecting cycles.

As discussed in Appendix G, single-mode fibers only transmit light-waves corresponding with the basic mode of electromagnetic field vibration and therefore should be used preferably in combination with a single-mode laser, tuned to that wave-length. However the use of monochromatic coherent laser light causes a loss of stability of the code-disk reflection signal (Fig. 5.3-4). This may be due to interferometric functioning of the assembly. Light reflects on the code-disk as well as on the end-face of the fiber, the distance between which changes in time by the rotation of the fiber. Amplifying and destructive interference of these two beams add an erratic component to the alternating code-disk signal.

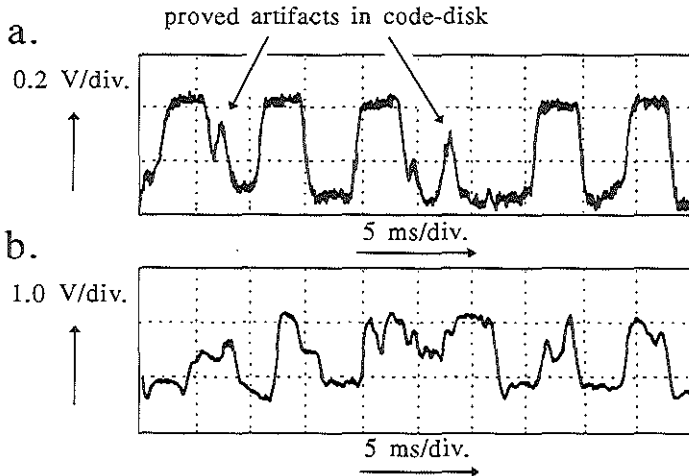


Fig. 5.3-4 Reflection signals of a code-disk, made by lift-off of nickel on macor® (a glass-ceramic): using a MM-fiber with a LED light-source (a) and a SM-fiber with a single-mode laser (b).

To overcome this problem the tip-surface of the fiber can be made somewhat slantingly (e.g. under 6°), so that light reflecting on this surface will not be transmitted by the fiber. Too large an angle will inhibit the light reflected by the code-disk from re-entering the fiber-core.

Cutting and polishing the tip-end of the fiber is a critical and time-consuming job. Cleaving slantingly has shown to be a more practical solution. However it adds another specialized action to the process of assembling a catheter.

Application of a multimode fiber

The possibilities of these fibers have only been recognized later in the course of the project. A multimode optical fiber has a larger core-diameter (typical sizes are 50 or 100 μm). Therefore the spot in front of the fiber-tip is also much larger. However, using a multimode fiber to guide the light to and from the code-disk sufficient signal modulation can be obtained, although several reflecting lines of the code-disk are within "the field of view" of the fiber. At some distance from the fiber-tip, e.g. 1 mm, a large spot on the code-disk is illuminated (Fig. 5.3-5). But most of the light reflecting from the code-disk will not be captured back into the fiber. In fact, only light reflecting on the very central spot, around the optical axis will be able to do so. This way a high resolution of the system is maintained, even for relatively large distances between the fiber-tip and the code-disk. Evidently, the signal amplitude will decrease with increasing distance (Fig. 5.3-6). Because of the large fiber diameter a surplus of light can be guided to the code-disk, so that the distance will be less critical.

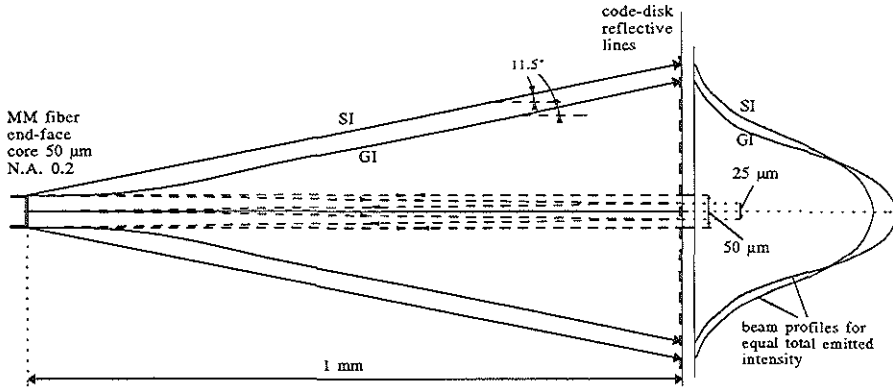


Fig. 5.3-5 Communication between a multimode fiber-tip and a code-disk at a distance of 1 mm. SI = step-index, GI = graded index.

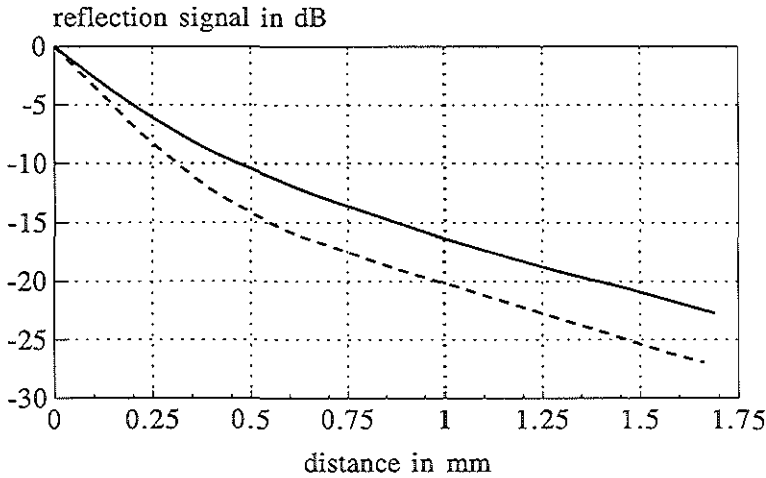


Fig. 5.3-6 Power of the reflection signal in dB, as a function of the distance between fiber-tip and code-disk, for a graded index multimode fiber, with a core diameter of 62.5 μm . Measurements performed dry (---) and in water (—).

The intensity profile of a step-index fiber is uniform in the fiber and close to the fiber-tip and develops to a Gaussian profile further away from the tip.

The intensity profile of a graded index multimode fiber is Gaussian in the fiber as well as outside the fiber, so the highest intensity appears in a small diameter. The maximum angle with the central axis of the fiber, under which light-rays can leave or enter the fiber-tip is a function of the radius r from the center of the core. The maximum numeric aperture exists in the center and decreases to zero at the core-cladding interface, where rays are

only allowed to travel parallel to the fiber axis.

At small distances to the fiber-tip, the performance of a graded index fiber, with respect to detection of the single reflecting lines of the code-disk, will be better than using a step-index fiber. This is due to the concentration of light intensity close to the optical axis for the graded index fiber (Fig. 5.3-7). At larger distances, where detection becomes more critical, the difference between both types of fibers becomes marginal. Both fibers are superior to the single-mode fiber for this application (compare Fig. 5.3-6 and Fig. 5.3-2).

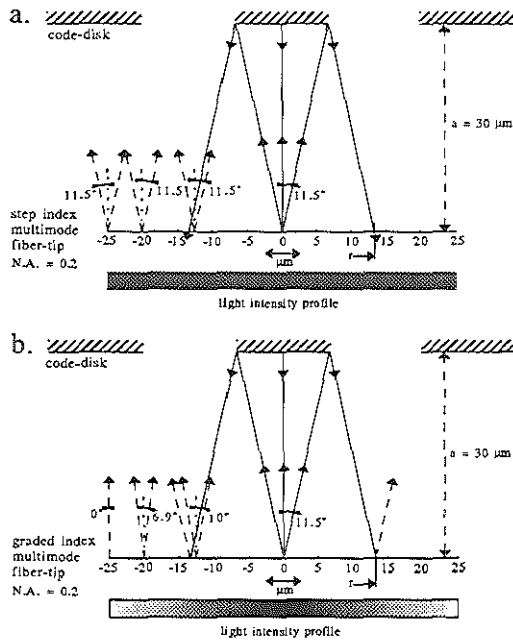


Fig. 5.3-7 Pathways of the light between the fiber-tip and the code-disk with respect of the visibility of single reflecting code-disk lines, for small distance between fiber-tip and code-disk ($30 \mu\text{m}$). Using a step-index MM fiber (a). Using a graded index MM fiber (b).

The power transmitted by a multimode fiber is higher than the power conducted by the narrow core of a single-mode fiber, using the same optical source. Coupling of multimode fibers is less critical because of the larger core-diameter, while standard coupling devices for these fibers are readily available. By using a Light Emitting Diode instead of a laser, in combination with a multimode fiber, the problem of interference will also be solved.

Other optical fiber considerations

The fiber-jacket provides a mechanical protection depending on the jacket material and thickness.

Built into the catheter the fiber has to withstand a certain maximum curvature (radius ≥ 20 mm), while the drive-shaft with the fiber inside is rotating at 1000 rpm. Furthermore, close to the code-disk the fiber is led away from the centre-line of the catheter, to face the code-disk lines, resulting in a fairly sharp S-curve caused by a lateral displacement of 0.4 mm over an axial distance of 0.8 mm (Fig. 5.3-10, Fig. 5.3-14). This fiber deformation is static and may cause considerable loss of power. Besides that, micro-cracking or even fracture of the fiber may occur caused by creep.

All fibers to be applied in the catheter system have been tested for their mechanical qualities in terms of breaking and power loss (Fig. 5.3-8 and 5.3-9).

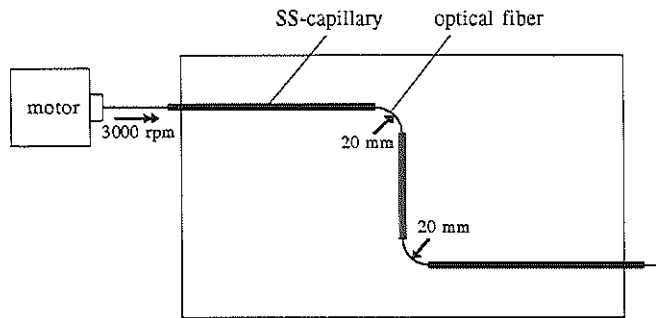


Fig. 5.3-8 Set-up for testing of mechanical fatigue of the fiber [3].

Other considerations will also influence the choice of the jacket.

It has been shown that a single-mode fiber with a 27 μm thick UV-acrylate jacket cannot easily be mounted accurately into the S-curve fitting. The acrylate jacket layer is too soft to hold the quite rigid 80 μm optical fiber nicely in place in the intended S-curve (Fig. 5.3-10). Stripping the fiber over this distance of course is no solution, because without the jacket the fiber is too fragile.

The coating of a standard multimode optical fiber has a typical outer diameter of 250 μm and consists of a double layer system. The first layer is a soft silicone type buffer, the second layer consists of a UV hardened acrylate. The layers are thick and soft, so that the mounting problem in the S-curve still remains.

Special multimode fibers are available with very thin coatings, often metal or poly-imide (PI). We have chosen a 100/125/135 μm graded index multimode fiber with PI jacket. The 5 μm PI jacket proved to be a solution to this mounting problem.

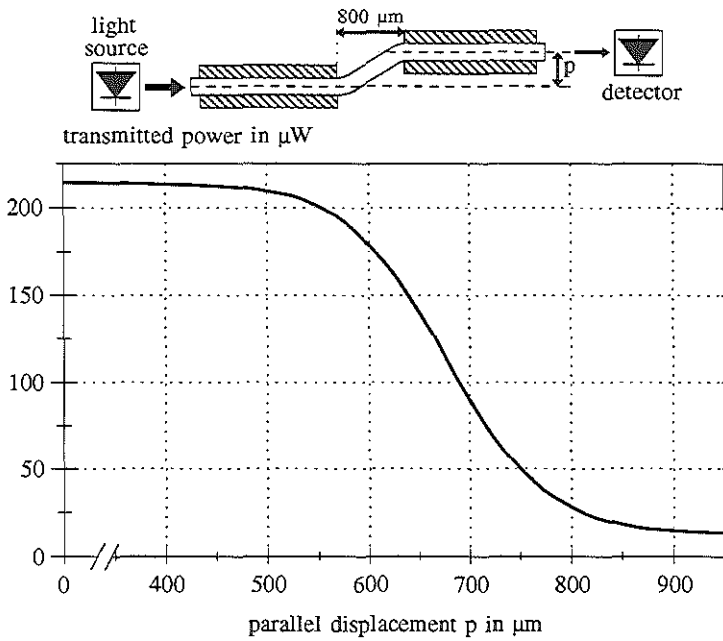


Fig. 5.3-9 Power loss of a SM fiber with UV-acrylate jacket in an S-curve, as a function of the lateral displacement p [3].

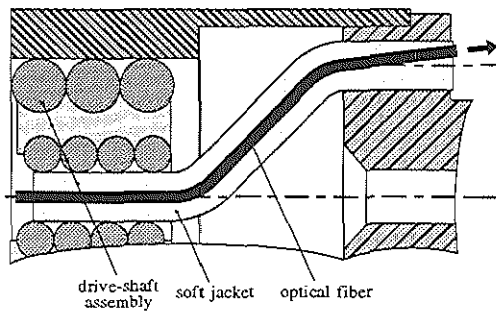


Fig. 5.3-10 Mounting problem of the SM fiber in an S-curve, due to the soft jacket material.

Code-disk

Design

Given the structure of the angle detection system, a rotating optical fiber interacting with reflecting code-lines on a static body, two types of these bodies are considered.

The first is a code-disk, mounted in the tip of the catheter with its reflecting surface perpendicular to the catheter axis and radial reflecting lines. To interact with the code-lines, the light path has to be oriented perpendicular to the reflective surface, so that the fiber will be mounted parallel to the catheter long axis.

A second approach can be a cylindrical code-body with reflecting lines on the inside surface, parallel to the catheter axis. The optical fiber now should either be bent over 90° or a mirror should provide the required orientation of the light path (Fig. 5.3-11).

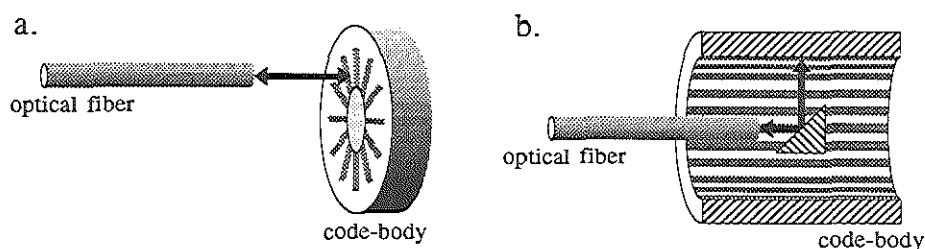


Fig. 5.3-11 Design of angular detection system, using a code-disk (a), using a code-cylinder (b).

Especially these last considerations were thought to be a draw-back for the second design. The small diameter of the catheter does not permit the fiber to be bent over 90° . The radius of curvature becomes too small and the fiber will crack. A 45° refractive surface at the fiber-tip can be achieved by very precise cleavage of the fiber, but this adds to the complexity of the system, as also does the application of a separate mirror construction element.

Therefore the code-disk system has been chosen for preliminary catheter prototyping. Reconsideration of the whole system, based on the acquired experience building these prototypes has resulted in a more favourable opinion about the application of a cylindrical code-body (§ 5.3.4).

Dimensions of the code-disk can be derived from the over-all diameter of the catheter and the necessity to minimize the stiff length of the catheter-tip. A catheter with a diameter of 1.7 mm can accommodate a 1.2 mm OD code-disk and a practical thickness of the disk is chosen to be 0.6 mm. Furthermore a hole (diameter 0.5 mm) should be present in the middle of the disk to accommodate the extension of the drive-shaft beyond the code-disk,

where the ultrasonic transducer is mounted onto the shaft (see Fig. 5.3-14).

To meet the high angular resolution requirements, derived from the amount of 500 produced image-lines per revolution, the code-disk should contain 250 reflecting lines. Triggering on both edges of the reflection signal will yield also 500 defined angular positions.

The optical path intersects the code-disk at a radial position of 0.425 mm. That means that applying 250 reflecting lines on this circle, the width of one line is about $5\text{ }\mu\text{m}$, assuming equal width of reflecting and non-reflecting lines. This resolution makes high demands upon the production method for code-disks, as well as the fiber-optic technology to detect every single line.

This high resolution angle detection is required only when rapid fluctuations of the rotation speed are to be expected. Otherwise a lower order approximation of the angular position will be sufficient.

Since the exact mechanical behaviour of the specially constructed drive-shaft, which contains the optical fiber as well as electrical conductors, was unknown, a compromise has been defined by applying 78 reflecting lines (Fig. 5.3-12).

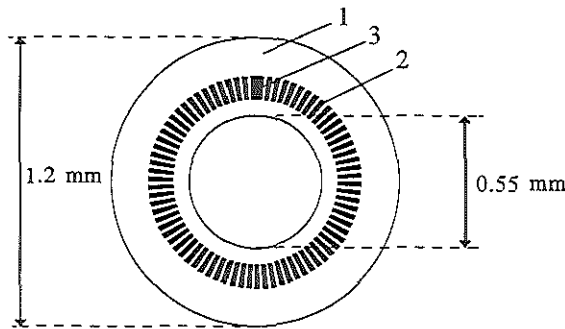


Fig. 5.3-12 Code-disk design consisting of a disk-shaped substrate with low reflectivity surface (1), highly reflective radial lines (2) and one radial line with triple width in order to generate a reset-pulse (3).

One of the optical requirements of a code-disk is the sharp code-pattern, without artifacts, to obtain adequate separation of the reflection signals of succeeding code-lines. The choice of materials with suitable reflective properties provides the modulation depth (contrast). Once built into the catheter-tip the code-disk requires a few more properties. The acoustical system demands fluid filling of the catheter-tip and because of medical safety reasons this fluid is chosen to be water. The code-disk has to survive in this environment. Furthermore, according to the design the code-disk itself represents an axial bearing surface, so that friction and wear may be an issue.

Manufacturing methods

A number of manufacturing methods has been explored to create an acceptable code-disk. Four methods are described in Appendix H and evaluated for the use in this application. A laser engraved pattern in nickel on a glass-ceramic (macor[®]) substrate gave the best results of all trials.

Drive-shaft assembly

For this catheter a drive-shaft (drive-cable) has been developed, performing three functions. Its first function is the rotation transmission from the proximal motor to the catheter-tip. Secondly the drive-shaft has to transmit electrical signals to and from the US-transducer and its third function is the transmission of optical signals for the angle detection system.

1. Rotation transmission

Nearly any drive-cable will do, if only transmission of rotary motion is needed, which seems to be the case when an angle detection system is implemented to correct for non-uniform tip-rotations. But it will be shown that the performance of the drive-shaft has to meet certain requirements, even with the angle-detection system present. The tip rotation should not deviate too much from the uniform motor rotation. This can be translated into desired mechanical properties of the drive-shaft, such as low flexural rigidity combined with high torsional rigidity. A spiral-type drive-shaft may perform well enough, if the coils are tightly wound upon an incompressible core or in case the double counter-wound spiral technique is used [4].

2. Electrical signal transmission

In Appendix I several configurations of conductors are analyzed with the help of [5] and compared for this application. The values of the signal loss in these transmission lines can only be used as a guidance, because of the use of a simplified model (tubular conductors instead of helical coils) and the fact that one always has to compromise with available wire sizes and different properties of materials. In conclusion all three arrangements (coax, tricoax around the optical fiber and twisted pair) may be suitable, as long as a certain optimal value for the design parameter D/d (Fig. I-1) is used.

3. Optical signal transmission

An optical fiber incorporated in the drive-shaft, preferably on the centre-line to ensure equal flexural rigidity in all planes, will perform this function. A multimode fiber is preferred, but a standard fiber with over-all diameter of 250 μm (mostly used for telecommunication) causes assembly problems. Therefore a special multimode fiber has been selected with dimensions 100/125/135 μm (core/cladding/jacket).

Manufacturing of the drive-shaft

In the first design approach of the angle detection system the tricoaxial drive-shaft design has been chosen (Fig. I-2, option b1).

Its construction is rotation symmetrical so that its flexural rigidity is equal in every plane of curvature, which contributes to a better mechanical behaviour.

A double wound stainless steel spiral is not used yet. The necessity for applying this complicated structure in the drive-shaft to improve the mechanical properties should first be proven.

A tricoax with an outer diameter of about 0.8 mm has been produced around a 135 μm optical fiber (Fig. 5.3-13). Although electrical transmission-line characteristics of the shaft allow the use of thin copper wire (20-50 μm OD), the manufacturing process runs into difficulty when copper wire smaller than 80 μm OD is used. Therefore a first layer of 7 lead copper wire with an outer diameter of 100 μm has been helically wound around the fiber. Then a 80 μm nylon 11 dielectric layer has been extruded on top of this. And finally the second layer of copper wire with an outer diameter of 140 μm , 6 lead helically wound, has been applied, serving also the purpose of improving the mechanical properties of the shaft.

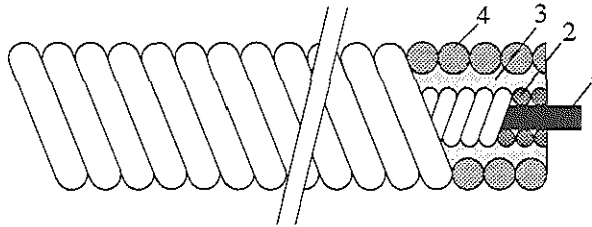


Fig. 5.3-13 First approach construction of the drive-shaft with integrated optical fiber (1), first conductor (2), dielectric (3) and second conductor (4).

The ratio D/d , defined in Appendix I, is about 1.5. Theoretically the total signal loss of this drive-shaft/transmission-line is about 6 dB (Fig. I-3a), which is close to optimal. The theoretical impedance of the cable is 14 Ω . Measurements have shown an impedance of 22 Ω . The order of magnitude is the same. The difference may be explained by the use of the simplified model and deviating material properties.

Other design considerations

The main issue of this paragraph is the incorporation of an angle detection system into the catheter. Some catheter requirements however influence design choices and performance of the angle detection system, so that they have to be taken into account.

Patient safety: enclosing dome

We found polymethylpentene (TPX) to be the best material, combining low loss of US-energy with enough strength and stiffness for the dome to be self-supporting at a wall-thickness of approximately 0.1 mm.

The dome also will prevent blood from entering the catheter so that the bearing friction and the optical path between fiber and code-disk will not be influenced by the presence of blood (-clots).

Fluid filling

The very small dimensions make it impossible to seal the dome compartment around the rotating shaft so that water will be confined to this volume. Therefore water may find its way to the space between fiber-tip and code-disk, which will change the optical path of the light due to change of refractive index.

Optical reflection signals will remain constant as long as there is no change of optical transmission medium during operation. That means that the space between fiber-tip and code-disk should be guaranteed to be filled with either air or water. Since the first is not possible, holes are created to facilitate access of filling fluid to this compartment (Fig. 5.3-14).

The optical performance of a water filled system is even better than the air filled system, because the divergence of the light-beam is lower.

The development of an easy, quick and reliable method of fluid filling, either as a last step in the manufacturing process or just before clinical use of the catheter, is a separate issue and will not be discussed here.

Of fundamental importance however is the choice for either a closed or an open dome. The closed dome seems to provide better protection against dust or wear particles in the filling fluid and possible toxic hazards. But it introduces a major problem for the fluid filling procedure, which in this case may have to take place as a step in the production process, because of an elaborate time-consuming vacuum-filling technique.

The catheter in this case has to withstand the vacuum, possibly combined with a small raise of temperature to accelerate the evacuation process. It has been shown that under these conditions some torsional tension built-in into the drive-shaft during the copper-wire winding process slowly is released. This causes torquing and coiling of the fiber in the proximal connector. By casting the fiber into epoxy, this mechanical strain is eliminated.

A filling procedure which forms part of the production process has more major drawbacks. It yields a water-filled product with limited shelf-life, due to degradation of polymers, glue-joints and the US-transducer. Swelling of polymers can cause jamming of the bearings. The polymer catheter will gradually loose water by diffusion so that a proper filling of the tip cannot be guaranteed in the long run.

After filling the product should be sterilized. The presence of water allows only gamma-sterilization. The combination of water and gamma-radiation has proven to limit the product shelf-life even more.

The open dome with a valve mechanism to prevent blood from entering the catheter without the need for a drip, allows fluid filling at the bed-side. The problems accompanying a wet product are much smaller in this case where the exposure to water is limited to the duration of the catheterization procedure (≈ 1 hour).

Connection to driving unit

The driving unit contains, besides stationary electronics, a motor for the drive-shaft/US-transducer rotation and a rotating PC-board with electronic and optical components to communicate with the rotating elements of the catheter. This rotating electronics provides for the pulse generation for excitation of the US-transducer and pre-amplification of the echo-signals. Locating these functions on a rotating PC-board between the motor and the connector to the catheter serves two purposes. The burning-in of the contacts of the slip-rings due to the high power excitation pulse is avoided and the interference noise is kept to a minimum by the early amplification of the weak echo-signals. The optics (light-source and detector) was chosen to rotate as well, because of anticipated alignment problems when using an optical rotational joint. This problem, however, may not arise when using a multimode fiber with a large core diameter (50-100 μm).

The connection between driving unit and catheter consists of two parts: the connector at the side of the non-disposable driving unit, which should guarantee proper connection to a catheter for many times, and the connector of the disposable catheter in which expensive components should be avoided. Both parts have been designed concurrently.

The catheter connector has to perform several functions. It should provide for:

- connection of the static catheter-tube to the stationary housing of the driving unit,
- mechanical coupling for rotation transmission from the motor to the catheter drive-shaft,
- electrical contact between the rotating electronics and the electrical leads in the catheter drive-shaft,
- electrical contact between the catheter braiding and the system ground for shielding purposes,
- optical communication between the rotating light-source/detector and the optical fiber incorporated in the catheter drive-shaft,
- an inlet for fluid filling.

This list of functions makes the connector rather complex. A drawing of a prototype is shown in Fig. 5.3-15, pointing out the main components.

Synthesis: the catheter design

The development and choices of components of the angle detection system have been described. Also other considerations influencing the system design have been discussed. The synthesis of these developments results in the catheter design, consisting of the catheter-tip design (Fig. 5.3-14) and the connector design (Fig. 5.3-15).

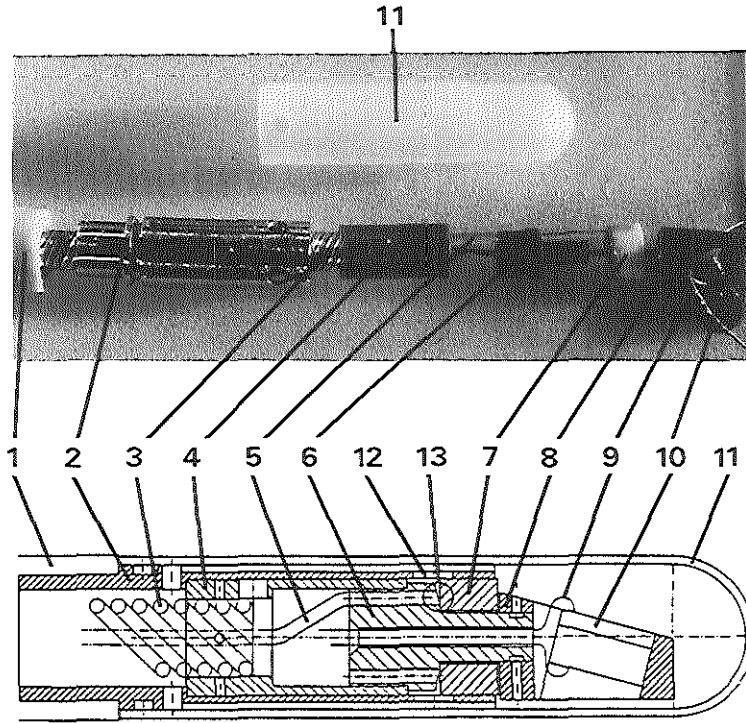


Fig. 5.3-14 Photograph of an "exploded view" of the catheter-tip (top) in combination with a construction drawing (bottom).

- | | | |
|-----------------------------------|------------------------------------|---------------------------------|
| 1. catheter-tube | 6. drive-shaft extension (PI) | 11. sonolucent dome |
| 2. outside bearing (SS) | 7. code-disk (substrate) | 12. hole for fluid access |
| 3. outer conductor of drive-shaft | 8. US-transducer housing | 13. optical interaction between |
| 4. inside bearing (PI) | 9. copper wire 40 μm OD | fiber-tip and code-disk |
| 5. optical fiber | 10. US-transducer | |

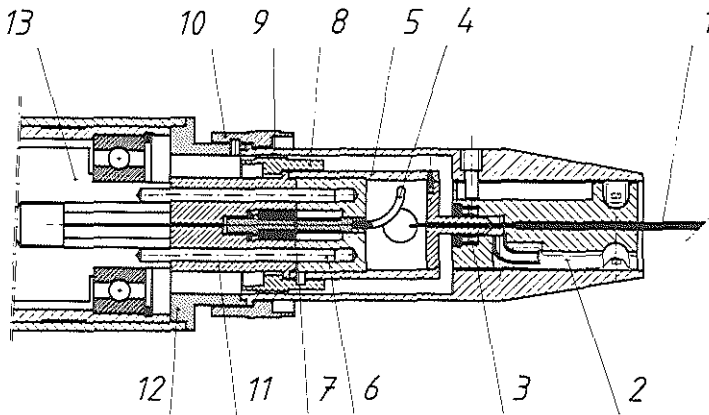


Fig. 5.3-15 Construction drawing of the catheter connector (by courtesy of the Productcentre TNO, Delft, The Netherlands).

- | | | |
|---------------------------------------------|-----------------------------------------------|--------------------------------------------------|
| 1. catheter | 6. electrical connection | 10. connecting nut of stationary connector |
| 2. fluid inlet | 7. optical connection | 11. rotating connector part of main-frame side |
| 3. closing ring | 8. connecting nut of rotating connector | 12. stationary connector part of main-frame side |
| 4. curled optical fiber | 9. stationary connector part of catheter side | 13. driving unit |
| 5. rotating connector part of catheter side | | |

§ 5.3.4 Discussion, conclusions and recommendations

Until now none of the catheter prototypes with a built-in angle detection system has been completely functional.

The angle detection system, isolated from the rest of the construction in an experimental set-up, is functional, i.e. provides well detectable spikes in accordance with the angle of rotation. However, processing this signal can be a problem.

The angle detection signal should be used to generate image-lines at equal tip-rotation increments, henceforth the display processing is straight forward. The success of this method depends on the maximum occurring momentary tip-rotation speed. For instance, if a tricoaxial drive-shaft performs under certain curved conditions, like the one described in [6, p. 197, Fig. 4b], its momentary angular velocity can be derived by differentiation (Fig. 5.3-16).

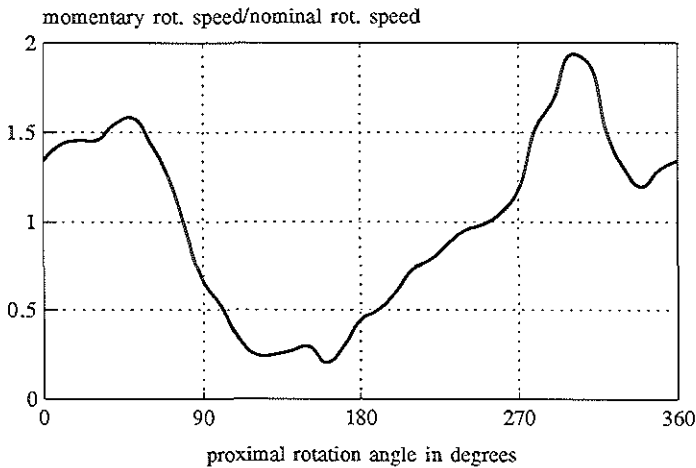


Fig. 5.3-16 Momentary divided by nominal tip-rotation speed of a tricoaxial drive-shaft, uniformly driven with 1000 rpm, 90° curved at the tip, $R = 20$ mm.

Momentary velocities occur of nearly two times the nominal rotation speed. Experience has shown that under more severely curved conditions, as is the case in coronary use of the catheter, the tricoaxial drive-shaft performs considerably worse. Adding a bearing at the tip for axial definition causes momentary velocities that exceed 10 times the nominal speed, causing problems related to "the fire-hose effect" and data-acquisition (§ 3.1). With respect to the first phenomenon it can be stated, that at a nominal rotation speed of 1000 rpm, the drive-shaft rotation transmission should not allow for momentary tip-rotation speeds higher than 10 times the nominal value. However, in this case the data-acquisition system (Fig. 2.4-3) can only produce 180 instead of 500 image-lines per revolution, reducing tangential resolution by 64 %. The momentary tip-rotation speed may therefore never exceed 3.6 times the nominal value.

Recommendations

The feasibility of a catheter-tip rotation-angle detection system, based on the optical interaction between a rotating optical fiber and a stationary code-disk has been demonstrated for the application in a 5.2 French flex-shaft driven intravascular echo-imaging catheter.

The effectiveness of the angle detection system regarding its image correction abilities has not been investigated, due to catheter prototype failure. To ensure the functionality of future prototypes, a redesign is necessary involving the following issues.

The mechanical properties of the tricoaxial drive-shaft are not sufficient to guarantee only small deviations from uniform rotation under all practical circumstances, so that the image building/correcting electronics will be able to follow. Application of the double-layer spiral flexible drive-shaft technique is recommended (Chapters 3 and 4). The optical fiber (135 μm OD) fits into the hollow lumen of the double-layer spiral drive-shaft (Table 4.3-2: type C), together with a micro-coaxial cable (290 μm OD). Of course this will cause an increase of the bending rigidity of the shaft, probably by about 100 %, with hardly any increase of the torsional rigidity. Consequently, the ratio bending rigidity/torsional rigidity will double, so that potential error angles will also double (§ 4.1). This may well be acceptable. However, the mechanical effect of the non-concentric structure of this drive-shaft should be carefully studied. Differences in bending rigidity in different planes should remain small (eq. 4-4: the parameter p should be small).

The design of Fig. 5.3-14 is primarily based on the use of a single-mode optical fiber. The accurate axial positioning of the end-face of this fiber with respect to the code-disk surface within 45 μm necessitates an axial fixation of the tip segment in a bearing. The friction occurring on these axial motion limiting surfaces decreases the fidelity of the tip-rotation. Using a graded-index multimode fiber these constraints can be relaxed, so that the presented bearing configuration can be abandoned.

In this case the transducer can be given enough axial freedom in the dome to avoid friction and the drive-shaft's axial position with respect to the catheter-tube is only determined at the proximal side (Fig. 5.3-17a). However, this may give rise to another problem. Many influences can change the length of the catheter-tube regarding the length of the drive-shaft, so that the actual axial position of the transducer with respect to the acoustic window may change accordingly, as does the distance between fiber-tip and code-disk.

A few of these influences are:

- Assembly conditions versus field conditions (humidity, temperature)
- Sterilization process (ETO may cause catheter-tube shrinkage)
- Geometrical situation during operation (curves may cause differences of length between drive-shaft and catheter-tube)

An extension of the sonolucent window with a few millimetres may solve the acoustic problem, but the gap between the fiber-tip and the code-disk should not exceed 1.5 mm (Fig. 5.3-6), using a graded index multimode fiber, with a core diameter of 62.5 μm , together with a laser engraved nickel on macor code-disk (Fig. H-4).

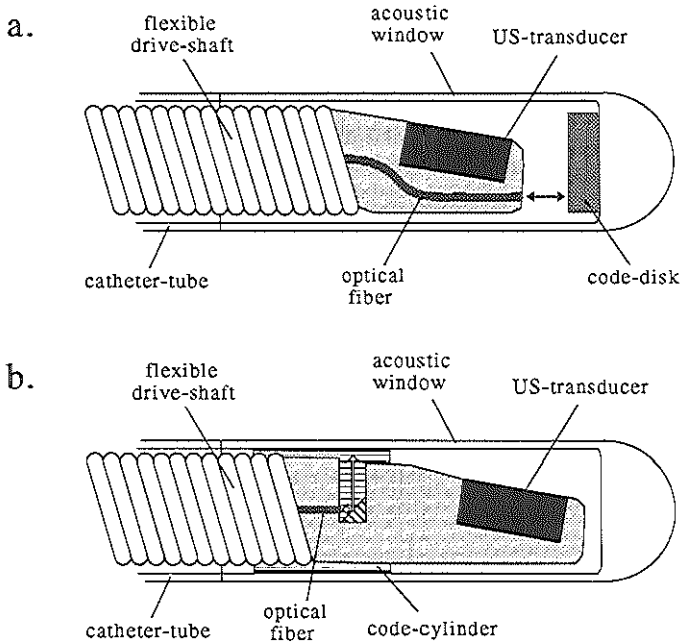


Fig. 5.3-17 Concepts of catheter-tip rotation angle detection: applying a multimode optical fiber, a code-disk and no tip-bearing (a), applying a multimode optical fiber, a 90° deflecting mirror and a code-cylinder (b).

It does not seem possible to forecast the resulting axial shift of the transducer and fiber-tip, with respect to the catheter-tube during operation, within this field of tolerance, so it cannot be corrected for already in the assembly process. If necessary, a final axial position adjustment feature can overcome this problem.

The maximum tolerable distance between fiber-tip and code-disk may be increased by a decrease of resolution of the angle detection system. By applying a smaller number of radial reflective lines, the lines can be made wider, so that they will reflect more light. A limitation is the maximum "visible" spot on the code-disk, which is in the order of the fiber core diameter (Fig. 5.3-5). Increase of the width of the code-lines above this diameter, will not improve the reflection signal any more.

The decrease of resolution of the angle detection system is acceptable, if the rotation angle transmission, performed by the flexible drive-shaft, is not erratic. For the double-layer spiral drive-shafts (Chapter 3) this may be expected, as long as circumstances are not extreme (Chapter 4). A "smoothly", mostly periodically changing error angle can be

registered with much less than 78 code-lines (= 156 defined angular positions). A number of 10 to 20 code lines could well be sufficient.

Another improvement of the system is the increase of contrast between the reflecting lines and the less-reflecting substrate. An interesting option is to find a substrate material, which is transparent for the applied wave-length of the light.

The problem of axial definition of the fiber-tip with respect to the code-disk can also be solved by the application of a code-cylinder (Fig. 5.3-11b). In this case the light should be deflected over 90° to establish communication between the fiber-tip and the reflecting code-lines, that are positioned parallel to the fiber-axis. Change of the axial position of the fiber-tip will not alter the distance to the reflecting lines. Similar to the extension of the acoustic window, the length of this code-cylinder can be chosen, to create sufficient axial tolerance (Fig. 5.3-17b).

A fluid-filling procedure involving catheter evacuation or slow diffusion of gas through the thin-walled dome is too time-consuming and therefore unfit for bed-side filling. Pre-filling however diminishes the product shelf-life drastically, especially after the only sterilization method possible in this case: gamma radiation.

A semi-open system involving a valve structure or semi-permeable barrier opens possibilities for bed-side filling and should therefore be investigated.

Especially when used in tortuous blood-vessels, like coronaries, the angle detection system will show its merits. But in this case the catheter diameter should be not much more than 1 mm (3 French). The prototypes made so far, including an angle detection system, are 1.73 mm OD (5.2 French), which is too big for this application. It is therefore a necessity to choose a technological concept for the angle detection system, which allows for miniaturization to the desired level.

References

1. Hoek M.J. van der, Bruijn D. de, Jongeling Th. J.M., Lancée C.T., Hoff H. ten, Ontwikkeling van een optische hoekencoder voor een roterend ultrasoon transducent, opgenomen in een catheterkop, Ned. tijdschrift voor Fotonica 4: 19-27, 1990.
2. Senior John M., Optical fiber communications, Prentice-Hall International Series in Optoelectronics, Series ed. P.J. Dean, 1985.
3. Jongeling Th.J.M., Vooronderzoek naar de toepassing van een optische hoekencoder in een catheter met roterende kop, Memorandum Technisch Fysische Dienst TNO-TH, Number 832.039, October 25, 1988.
4. Martin R.W., Johnson C.C., Design characteristics for intravascular ultrasonic catheters, Int. J. Cardiac. Imag. 4: 201-216, 1989.
5. Kandoian A.G., DeRosa L.A., eds., Reference data for radio engineers, fifth edition, 1970.
6. Hoff H. ten, Korbijn A., Smit Th.H., Klinkhamer J.F.F., Bom N., Imaging artifacts in mechanically driven ultrasound catheters, Int. J. Cardiac. Imag. 4: 195-199, 1989.

CHAPTER 6 Conclusions and recommendations

Conclusions

Intravascular ultrasound (US) imaging is a new exciting diagnostic technique, developed in order to deal with blood-vessel obstructive disease more adequately. Several complete systems are currently operational, developed as a joint effort by several research and development institutions and many industrial companies, under the supervision of the Erasmus University Rotterdam. Also the production of the total system requires input from many companies and is coordinated by Du-MED B.V. Clinical evaluation is in progress and the preliminary results are promising.

A basic decision in the system design is the choice in favour of mechanical scanning, where an ultrasonic beam, originating from a single ultrasonic transducer, is rotated by mechanical means. The other option consisting of a circular array of small rectangular elements, is able to electronically produce a 360° scan. This system yields a solid state catheter, with no moving parts, but the potential image quality is inferior and because of its complexity one would have to apprehend high development costs.

Several driving mechanisms to rotate the US-beam have been investigated. The need for a highly predictable rotary motion at the catheter-tip, in order to obtain a reliable image, is difficult to achieve. Two practical options have been chosen for further development: flexible drive-shaft rotation transmission through the catheter-tube and direct-drive of the US-beam in the catheter-tip by means of a miniature electro-magnetic motor.

The flexible drive-shaft rotation transmission has the disadvantage of showing a varying performance, depending on the catheter geometry, i.e. the actual configuration of curvatures in the catheter. However, this effect can be minimized.

The performance of the micromotor does not depend on the actual catheter curvatures. Prototype testing, under experimental conditions, has shown the ability of near-uniform rotation (periodic error angle < 10° peak-to-peak) at 3600 rpm.

A flexible drive-shaft with defined specifications (0.8 mm OD, bending rigidity = 1.5 Nmm² and torsional rigidity ≥ 100 Nmm²) can adequately transmit a rotary motion to the catheter-tip, even in case of severe catheter curvature (e.g. coronary use). The term "adequately" refers to the satisfaction of current clinical needs and is mainly quantified in this thesis as the occurrence of a periodic error angle < 20° peak-to-peak.

The key-parameter ruling the performance of a flexible drive-shaft in this catheter application is the ratio bending rigidity/torsional rigidity. It should be minimized to

decrease the sensitivity of the rotation transmission behaviour to disturbing factors, like pre-curvature, the occurrence of slightly different bending rigidities while bending around the two principal axes, and friction.

An optical detection system to constantly monitor the actual rotation angle at the catheter-tip has shown its feasibility, as an isolated system, tested under experimental conditions. Further development, however, has been terminated, because of the complexity of the catheter construction and consequently high costs.

Recommendations related to clinical evaluation

Commercial success of the intravascular US-imaging technique depends on acceptance in every day clinical practice. In order to achieve that, the benefit of this new diagnostic method to the patient and/or the health-care system has to be proved. Only then reimbursement of the costs by health insurance companies can be expected. Therefore it is of vital importance that well-organized clinical investigations are conducted, strictly following protocols, including follow-up studies. A primary target of the manufacturers of intravascular US imaging systems should be the support of this clinical research, supplying sufficient well-functioning catheters, and conducting efficient trouble-shooting when necessary.

The feed-back from clinical evaluation reveals new information on the requirements of the system performance, to optimally serve the physician's wishes and needs. Translation of these wishes into pragmatic technological solutions, having a short "turn-around-time", will enhance clinical acceptance. Important in this process is the setting of adequate priorities and not jeopardizing the catheter production and the progress of clinical evaluation.

Already several improvements have been suggested. An increase of the over-all bending rigidity of the catheter would decrease the risk of kinking during insertion. However, a flexible tip-section is required in order to follow the guide-wire. A varying stiffness decreasing from the proximal side of the catheter towards the tip could be an interesting solution.

Changes have been made to enhance the grey-scale appearance on the screen, for better image appreciation. The integration of the angiographic image into the US-image screen is suggested as a practical feature for better interpretation and combination of the angio- and echo-graphic information.

These equations are numerically solved by an integration method which resembles the central difference method [5]. Of all explicit methods this method has the largest stability region per function evaluation. The method is given by the formulae:

$$\mathbf{k} = (\mathbf{M}^{-1}\mathbf{f})(t_n + \frac{1}{2}h, \mathbf{x}_n + \frac{1}{2}h\dot{\mathbf{x}}_n, \dot{\mathbf{x}}_n)$$

$$\dot{\mathbf{x}}_{n+1} = \dot{\mathbf{x}}_n + h\mathbf{k}$$

$$\mathbf{x}_{n+1} = \mathbf{x}_n + h\dot{\mathbf{x}}_n + \frac{1}{2}h^2\mathbf{k}$$

where h is the stepsize.

References

1. Wittenburg J., Dynamics of systems of rigid bodies, Teubner, Stuttgart, pp. 21-23, 1977.
2. Besseling J.F., Non-linear analysis of structures by the finite element method as a supplement to a linear analysis, Computer Methods in Applied Mechanics and Engineering 3, pp. 173-194, 1974.
3. Werff K. van der, Jonker J.B., Dynamics of flexible mechanics, In: E.J. Haug (ed.), Computer aided analysis and optimization of mechanical system dynamics, Springer-Verlag, Berlin, pp. 381-400, 1984.
4. Meijaard J.P., Direct determination of periodic solutions of the dynamical equations of flexible mechanisms and manipulators, International Journal for Numerical Methods in Engineering 32, pp. 1691-1710, 1991.
5. Meijaard J.P., A comparison of numerical integration methods with a view to fast simulation of mechanical dynamical systems, In: E.J. Haug and R.C. Deyo (eds.), Real time integration methods for mechanical system simulation, Springer-Verlag, Heidelberg, pp. 329-343, 1991.
6. Jonker B., A finite element dynamic analysis of flexible spatial mechanisms and manipulators, PhD. Thesis, Delft University of Technology, Faculty of Mechanical Engineering and Marine Technology, p. 43, 1988.

APPENDIX F Measurement methods for determination of flexible drive-shaft properties

Bending rigidity EI

Small deflections

Normally the bending rigidity of a beam can be determined by measuring the deflection of the beam at the tip v [mm], caused by a known force F [N], applied to the tip of the beam and working perpendicular to the central axis of the beam (Fig. F-1a). The free length of the beam is l [mm].

If the deflection is small, the bending rigidity EI [N/mm²] can then be found by [1]:

$$EI = \frac{Fl^3}{3v} \quad (\text{F-1})$$

If the beam deflects under its own weight (Fig. F-1b), a distributed force q [N/mm] can be defined as:

$$q = \frac{mg}{L} \quad (\text{F-2})$$

where

m/L [kg/mm] = mass per unit length of the beam

g [m/s²] = acceleration due to gravitation = 9.8 m/s²

And from the deflection caused by q , only if it is small, the bending rigidity can be derived by:

$$EI = \frac{ql^4}{8v} \quad (\text{F-3})$$

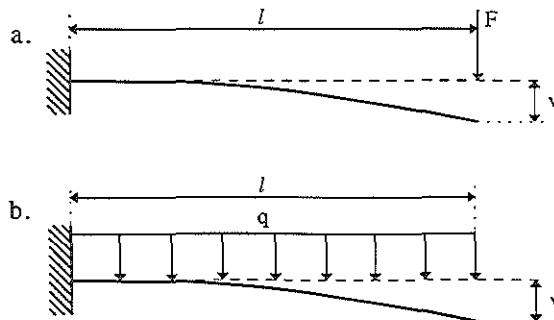


Fig. F-1 Deflection v of the free length l of a beam, caused by a lateral force F at the tip (a) or a distributed (e.g. gravitational) force q (b).

The bending rigidity of the relatively stiff stainless steel capillary drive-shafts has been determined this way.

However, the bending rigidity of a flexible drive-shaft is so low, that large deflections already occur, caused by the distributed gravitational forces. A bending rigidity measuring method as described above is therefore not possible.

Large deflections

In case of large deflections a simple analytical solution does not exist, but a more laborious numerical solution can be obtained [1, pp. 234-239].

A simple estimation method for the bending rigidity of the shaft can be found, by using a description of the geometry as it appears to be, observing a flexible drive-shaft, horizontally fixed in a support, with a relatively long length l of the shaft kept free (Fig. F-2).

The long free length of the shaft will bend strongly under its own weight, until most of the length is hanging close to vertically. The supposedly straight vertical length of the shaft is l_1 .

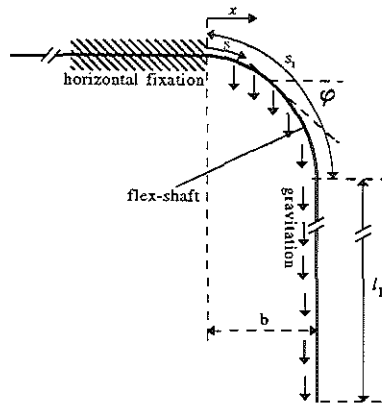


Fig. F-2 Set-up for measuring the bending rigidity of a flexible shaft.

The force F working on the vertical line coinciding with this part of the shaft is then:

$$F = \frac{mgl_1}{L} \quad (\text{F-4})$$

A linear coordinate x is defined horizontally, starting from the fixture and a horizontal distance b can be measured between the fixture and the vertically hanging part of the shaft.

The force F determines most of the bending moment $M(x)$ in the curved part s_1 of the shaft and:

$$\frac{mgl_1}{L}(b-x) < M(x) < \frac{mgl}{L}(b-x) \quad (\text{F-5})$$

we use as an estimation for $M(x)$:

$$M(x) \approx \frac{mgl}{L}(b-x) \quad (\text{F-6})$$

The slope-angle φ is defined with respect to the x -axis. Along the curve the coordinate s is defined and a local radius of curvature ρ . From basic theory we know:

$$M = \frac{EI}{ds} \frac{d\varphi}{ds} \quad (\text{F-7})$$

Considering that $dx = \cos\varphi ds$, we can combine eqs. F-6 and F-7 into the differential equation:

$$\cos\varphi d\varphi = \frac{mgl}{EIL}(b-x)dx \quad (\text{F-8})$$

Integration of eq. F-8 gives an approximation for the bending rigidity:

$$EI_a = \frac{mglb^2}{2L} \quad (\text{F-9})$$

The quantity $q = mg/L$ can be found by weighing a drive-shaft and measuring its length, l is determined in the measuring set-up and the horizontal distance b can be measured. The bending rigidity can be approximated by eq. F-9.

The horizontal distance b has been determined at the point on the shaft, where $s \approx l/4$. This is done to avoid errors in the measurements, caused by slight pre-curvatures in the drive-shafts. Close to the tip, the vertical force in the shaft is too small to stretch the shaft, so that the tip may deviate from the vertical line.

The validity of the approximation method, described above, has been investigated by a comparison with numerical calculations. By extensive iteration, the accuracy of these calculations has been improved up to about 10 significant digits. The comparison is shown in Fig. F-3.

The dimensionless horizontal distance b/l (left scale), for the point on the shaft where $s = l/4$ is put in the figure as a function of the dimensionless quantity ql^3/EI . The bold line shows the relationship according to the finite element calculations, the thin line depicts the approximation model. Knowing b , l and q , the bending rigidity can be determined both ways, i.e. according to the finite element method (EI) and with the use of eq. F-9 (EI_a).

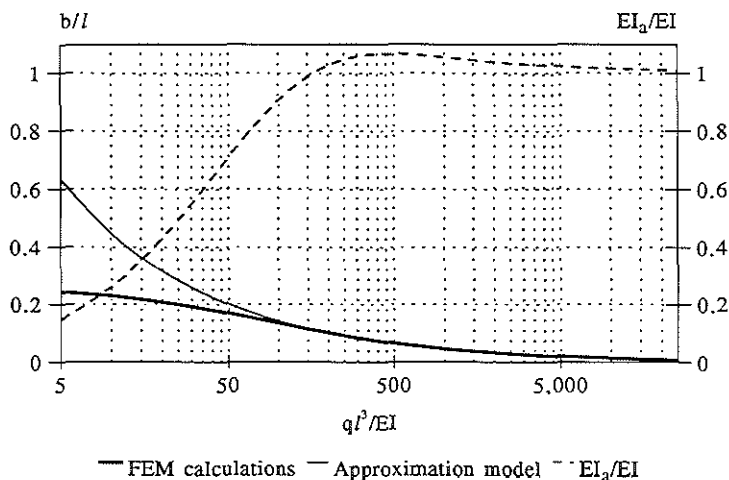


Fig. F-3 Validity of the approximation method for determining the bending rigidity of a flexible shaft.

The ratio EI_a/EI is also given in Fig. F-3 (right scale) as a function of the dimensionless quantity ql^3/EI . It shows that for $ql^3/EI > 120$ the error in the approximation method is $< 6\%$. For $ql^3/EI > 7000$ this error is in the order of 1% .

For the flexible drive-shaft type B we found $ql^3/EI \approx 3500$ and for type C $ql^3/EI \approx 20,000$. The error in the measurements of the bending rigidity, using the approximation method is therefore mostly dependent on the accuracy of the measurement of the distance b . This has been possible within 5% , so that the error in EI_a is about 10% .

Torsional rigidity

A direct measurement of the torsional rigidity of flexible drive-shafts by applying a torque and measuring the torsion angle is difficult, because the main interest exists for the initial torsional rigidity, i.e. for small rotation angles. This requires only little torque ($< 5 \cdot 10^{-3}$ Nmm) for which no accurate measurement equipment is available.

The torsional rigidity can better be determined by measuring the fundamental frequency of the vibration in torsion mode of a vertically hanging piece l [m] of the drive-shaft, with a body with known moment of inertia J [kgmm²] attached to it, where $J \gg J_l$ and J_l is the moment of inertia of the drive-shaft length l , around its central axis (Fig. F-4).

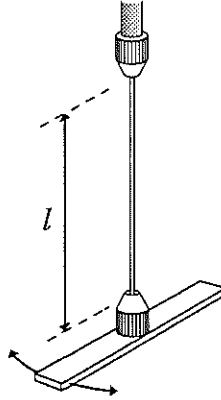


Fig. F-4 Set-up for the measurement of the torsional rigidity.

For a shaft with purely linear elastic deformation behaviour, the torsional rigidity S_t [Nmm^2] is found from the formula [2]:

$$S_t = 4\pi^2 \nu^2 J l \quad (\text{F-10})$$

where

ν [Hz] = fundamental frequency

In case of some energy loss, caused by damping eq. F-10 still is valid within 1 %, as long as:

$$b = \frac{D}{2J} = \nu \ln\left(\frac{A_n}{A_{n+1}}\right) < 0.88 \nu \quad (\text{F-11})$$

where

D = damping constant

A_n and A_{n+1} are two amplitudes of the torsion vibration of succeeding cycles

Friction coefficient

The kinetic friction coefficient between drive-shaft and catheter-tube can be determined using the set-up of Fig. F-5. A thick-walled cylinder contains a part of the catheter-tubing (with inner diameter D) in an accurately centred hole, the combination of which represents a mass m_1 . Perpendicular to the central axis of the cylinder and the catheter-tube a rod is mounted onto the cylinder. The part l' , sticking out of the cylinder and functioning as a

pointer, represents a mass m_2 . The total arm-length of the pointer, measured from the centre of the catheter-tube is $l + D/2$.

A piece of flexible drive-shaft is mounted onto the drive-shaft of a motor, where the latter is extended, accurately fitting, through the lumen of the flex-shaft to stiffen it.

The cylinder with catheter-tube and pointer is shifted onto the drive-shaft, so that the rod points vertically downwards, in line with the point of support.

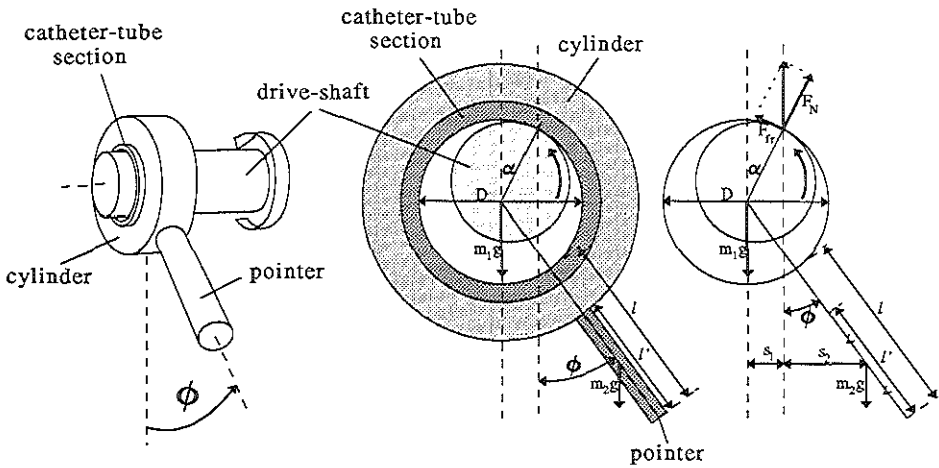


Fig. F-5 Set-up for measurement of kinetic friction coefficient (left). Definition of forces and geometrical quantities (middle and right).

By rotation of the drive-shaft a tangential friction force F_{fr} is created between the drive-shaft and the inner wall of the catheter-tube. The point of support will move counter to the driving direction to a location where the radius of the catheter-tube makes an angle α with the vertical. The pointer will make an angle ϕ with the vertical.

From the geometry of Fig. F-5 and the equilibrium of forces and moments the friction coefficient μ can be derived as:

$$\mu = \tan[\arcsin(\frac{m_2(2l-l'+D)}{D(m_1+m_2)}\sin\phi)] \quad (F-12)$$

This method only works well if the choices of masses and geometry are made with an anticipation to the order of magnitude of the unknown friction coefficient. Otherwise the deflection of the rod is either too small to be read accurately, or the eccentric pointing rod is not able to produce a large enough compensating moment, so that it will start rotating around the shaft.

Determination of the radius of pre-curvature ρ_0

The radius of pre-curvature can be determined from the examination of the drive-shaft geometry, when it is free from bending moments. For a flexible drive-shaft with very low bending rigidity the friction forces, caused by the interaction with a supporting surface, may partly determine the drive-shaft geometry. This problem has been overcome by using a supporting surface of low friction material and by applying little mechanical shocks to it, to make the drive-shaft lose all its elastic energy and thus cancel out all present bending moments.

The xy -coordinates of a certain amount of points of the remaining curve in the (flexible) drive-shaft, with respect to an arbitrary Cartesian coordinate system, can be determined and a computer program finds the best fitting arc of a circle, which determines the radius of pre-curvature.

Determination of $p = (EI_z - EI_y)/(EI_y + EI_z)$

This measurement has only been performed for the slightly rolled stainless steel capillary. The bending rigidities EI_y and EI_z , when bending around the principal axes \bar{y} and \bar{z} , can be determined, using the method described earlier in this appendix. The accuracy of this measurement is not very high (5-10 %), so the accuracy of the determination of p , based on subtraction of two bending rigidities, would be very poor if only based on one measurement of EI_y and EI_z . By taking the average of many measurement results the accuracy of p has been improved to an acceptable level (± 5 %).

References

1. Timoshenko S.P., Gere J.M., Mechanics of materials, Van Nostrand Reinhold Company, New York, Cincinnati, Toronto, London, Melbourne, p. 203, 1973.
2. Hoff H. ten, De ontwikkeling van een stuurbare electrodecatheter voor endocardiale cathetermapping, MSc. Thesis, Technical University Twente, Division Precision Engineering, p. B3.6, 1984.

APPENDIX G Basic theory on optical fibers as dielectric waveguides

An optical fiber is a dielectric waveguide structure to enable light to propagate over long distances with minimum loss of intensity. Nowadays the most important use of these fibers is made in telecommunication.

Step-index optical fiber

The basic structure of an optical fiber is given (Fig. G-1) [1, p. 14, 128].

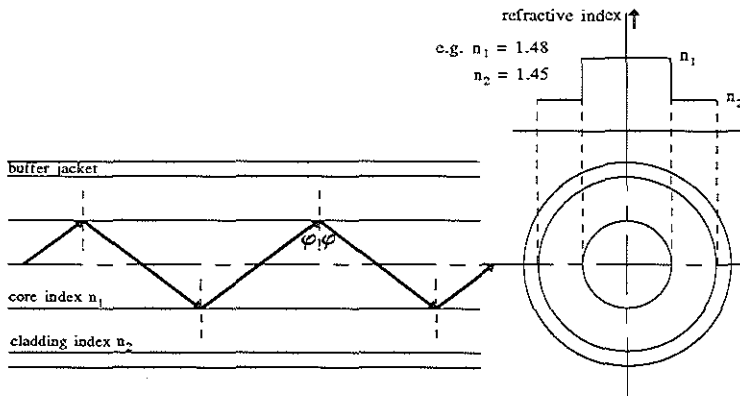


Fig. G-1 Basic guiding structure of a step-index optical fiber.

Core and cladding are made of a transparent dielectric material, typically silica glass, but in such a way that the refractive index of the cladding (n_2) is slightly lower than that of the core (n_1). Such a fiber is known as a step-index fiber.

Light propagating through the core at a sufficiently shallow angle (ϕ (Fig. G-1) is larger than the critical angle ϕ_c) is kept in the core by reflecting totally on the interface between core and cladding.

The angle ϕ_c can be found from Snellius' law of refraction, where the refracted light travels through the cladding, parallel to the fiber-axis.

$$\sin \phi_c = \frac{n_2}{n_1} \quad (\text{G-1})$$

The angle ϕ_c is related to the maximum angle β with respect to the fiber-axis, of a light-ray leaving the fiber or entering the fiber to be guided. The property to describe this, is called the numerical aperture (N.A.). In formula:

$$N.A. = n_0 \sin \beta \quad (G-2)$$

where n_0 is the refractive index of the medium facing the end-surface of the fiber.

If Snellius' law is also applied for this end-surface it can be shown that:

$$\sin \beta = \frac{n_1}{n_0} \cos \phi_c \quad \text{and} \quad (G-3)$$

$$N.A. = \sqrt{n_1^2 - n_2^2} \quad (G-4)$$

The typical small differences between n_1 and n_2 result in values for N.A. ranging from 0.1 to 0.3 (β in air ranges from 5.7° to 17.5° and in water, where $n_0 = 1.33$, β ranges from 4.3° to 13°).

Graded index optical fiber

An other type of optical fiber is the graded index fiber. Instead of a step in the refractive index this fiber has a near parabolic index profile. This way the light is guided through the core by refraction and not by reflection at the core/cladding boundary (Fig. G-2) [1, p. 129] .

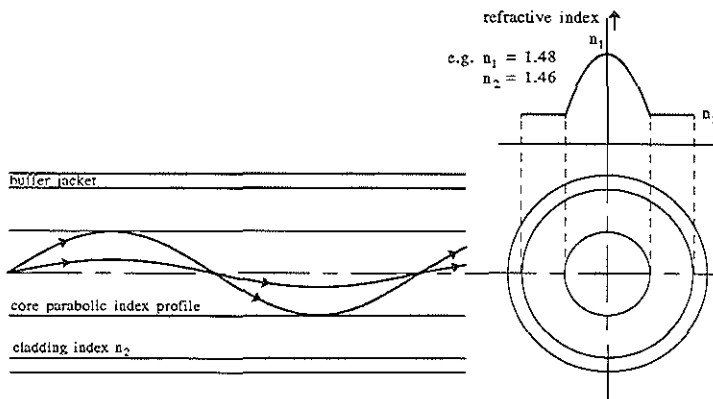


Fig. G-2 Graded index optical fiber, guiding light through the core by refraction.

The numerical aperture of the graded index fiber is dependent on the radial distance from the fiber-axis, decreasing to zero at the core radius. Its intensity profile is Gaussian.

The buffer jacket mostly made of a polymer or metal, serves the purpose of mechanical protection against the occurrence of too small radii of curvature, that may cause breaking of the silica glass fiber.

Single-mode (SM) and multimode (MM) fibers

Not just any electromagnetic wave can propagate through an optical fiber. The solution of Maxwell's equations for a homogeneous cylindrical core dielectric waveguide (the step index fiber) gives all the possible modal fields [2]. These modes are characterized by certain polarization profiles and intensity distributions in the fiber. In general it can be said that the bigger the core the more electric field modes the fiber will accommodate, resulting in a so called multimode optical fiber.

If the core-diameter is small enough ($< 10 \mu\text{m}$, depending on the difference in refractive indices of core and cladding) only one mode will be able to propagate along this fiber, which is called a single-mode fiber. The use of these fibers in long distance communication systems is predicted to grow, because of their extremely low attenuation and the much wider transmission bandwidth than of multimode fibers. More detailed physical fundamentals of single-mode optical fibers can be found in [3].

References

1. Senior J.M., Optical fiber communications, Prentice-Hall international series in Optoelectronics, Dean P.J. (ed.), 1985.
2. Snitzer E., Cylindrical dielectric waveguide modes, J. Opt. Soc. Am., 51, pp. 491-498, 1961.
3. Neumann E.-G., Single-mode fibers, Springer series in optical sciences, Ed. Theodor Tamir, Springer-Verlag, 1988.

APPENDIX H Production methods of code-disks

Electro-forming (Ni-foil code-disk)

The first type of code-disks which has been developed is a thin nickel foil disk (thickness 5 μm), with 78 radial slits, being the reflective material. Mounting this foil onto a thicker disk-shaped substrate of less reflecting material, e.g. poly-imid (PI), gives the complete code-disk assembly (Fig. H-1: top left).

The Ni-foil disk has been produced using the method of electro-forming. In this process nickel is electrically deposited onto a chromium layer (on a glass substrate), which has been given the wanted code-disk pattern, repeated in a matrix, by a photo-chemical method. During the electro-form process the nickel layer grows thicker, but also the slits of the code-disk pattern grow narrower. This way, given a minimum foil thickness, the maximum amount of code-disk lines is limited. Or given the large amount of lines, the foil thickness is limited to a few microns. Practically 78 slits is close to the limit, corresponding with a foil thickness of 5 μm . The nickel foil comes off the chromium layer by a thermal shock.

The smoothest, most reflective side of the foil is the one which was in contact with the chromium and thus should be the reflecting surface in our application. It can clearly be seen (Fig. H-1: bottom left) that the reflecting spokes of the code-disk have a cross-sectional profile with a lower section in the middle: the imprint of the chromium spoke onto which the nickel was deposited. This step is very little (about 1 μm), but the optical effect can be seen (Fig. H-2). The reflection peak has two side-lobes.

The main draw-back of this code-disk assembly is the mounting of the foil onto its substrate. The substrate material should be easy to form into its disk-shape. For prototyping a poly-imid (PI) disk has been used, machined on a lathe.

Bonding the foil on the PI substrate at these dimensions has proven to be difficult. A surplus of adhesive results easily in an unusable assembly, because the adhesive will appear at the wrong side of the foil, protruding through the slits. This will degrade its reflection characteristics. Reducing the amount of adhesive endangers the quality of the bond. The joint has to be water-resistant and possess enough shear-strength to withstand the friction resulting from the axial bearing forces.

Although the reflecting properties of this code-disk are adequate (Fig. H-2), mechanically it has proved to be a troublesome construction. Therefore other production processes have been investigated.

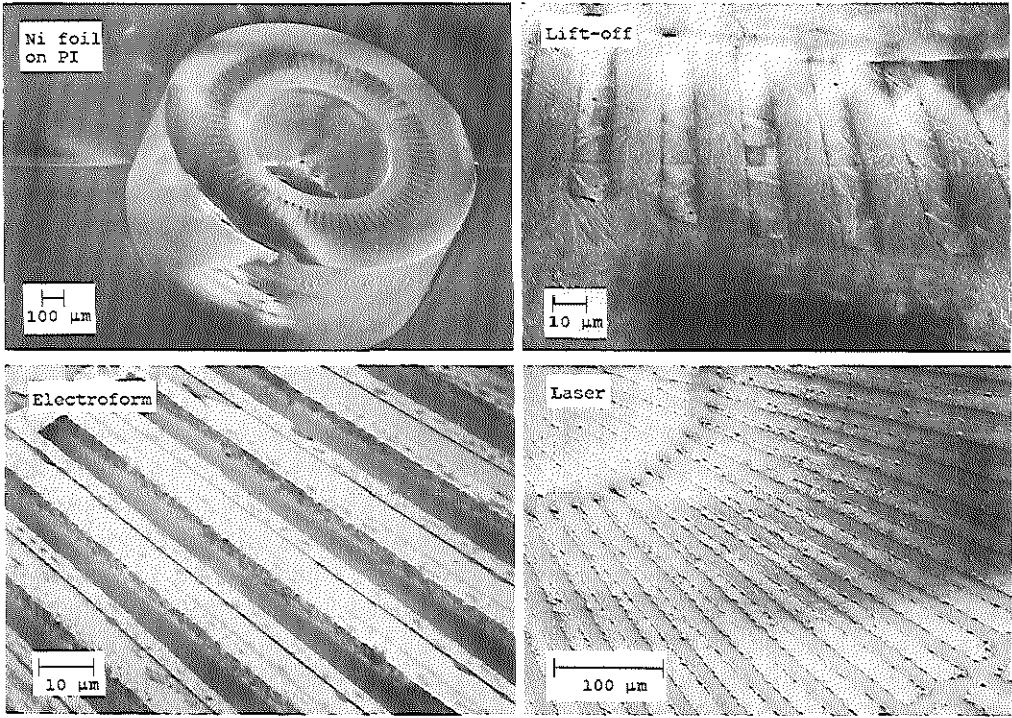


Fig. H-1 Scanning electron microscope pictures of code-disks produced by several methods.

Code-disk assembly of a nickel-foil code-disk, produced by electro-forming, on a PI substrate (top left) and details of:

- an electro-formed nickel-foil code-disk (bottom left)
- a nickel on macor code-disk, produced by the lift-off technique (top right)

Note: scratches also visible under nickel layer

- a nickel on macor code-disk, produced by laser engraving (bottom right).

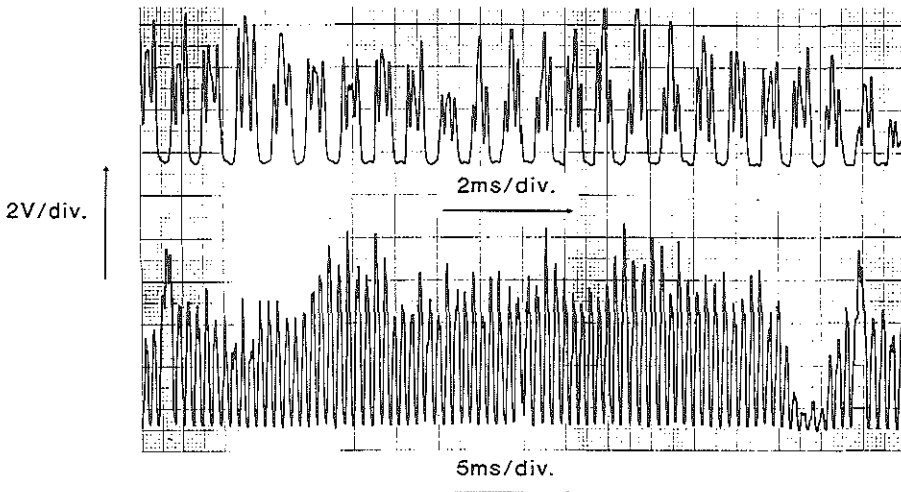


Fig. H-2 Signal response of nickel-foil on PI substrate code-disk assembly.

Photo-chemical lift-off technique (nickel on macor® substrate)

A much better mechanical bond between the reflective layer and the substrate material is achieved by sputtering the metal onto it. The lift-off technique meets that demand.

On a polished macor® substrate, which is a glass-ceramic, a layer of photo-resist has been applied, which is exposed with a pattern mask in between. As a mask the nickel-foil, obtained from the previous method, has been used successfully. The non-exposed photo-resist is washed away by chemicals, after which the nickel layer is sputtered onto the substrate. After the exposed photo-resist is dissolved by other chemicals, the nickel layer in these places can be lifted off the substrate, leaving the desired matrix of code-patterns on the macor. The code-disks can be retrieved from the macor plaque by machining or ultra-sonic drilling.

However, code-disks produced in this way, have not been fully functional. The choice of the substrate material causes one of the problems. The macor surface cannot be made smooth enough because of its granular structure, regardless of extensive mechanical polishing. The remaining micro-scratches (Fig. H-1: top right) cause the reflection from this code-disk to turn into scattering, rendering a fluctuating reflection signal. A mechanical-chemical polishing method has been more successful in creating a smooth surface, but the lift-off technique causes damage to the small detailed pattern of the code-disk (see Fig. 5.3-4). Maybe the composition of the chemicals, used in the lift-off step of the process, needs some fine-tuning.

Photo-chemical etch technique (nickel on silicon substrate)

A silicon wafer has been polished very smoothly, after which a nickel layer is sputtered onto it. A negative photo-resist layer is deposited, followed by exposure with the nickel-foil mask in between the light-source and the substrate. After washing away the exposed photo-resist, an etching bath etches away the nickel layer in these uncovered places. Removing the unexposed photo-resist after this, the matrix of code-patterns is obtained on a silicon substrate. The code-disks still have to be retrieved by cutting and grinding.

The smooth surface of the silicon has nearly the same reflectivity as the nickel layer, so that not enough contrast is obtained. A matching layer, optimized for silicon, applied on top of the whole disk solves the problem only partly: the contrast is improved considerably, but the reflectivity of the nickel is also diminished, causing a lower maximum signal amplitude.

Laser engraved pattern (nickel on macor substrate)

The last and most successful method of code-disk production has been the engraving of the code-pattern by a laser-beam on a nickel layer sputtered onto a macor substrate. The macor has to be chosen from the finest granular quality and by mechanical and chemical polishing it can be made smooth enough to give a good reflective surface once the nickel has been sputtered onto it.

The simplest way of engraving the code-pattern using the available equipment⁽¹⁾ has been to make the laser write straight radial lines, by moving the substrate with an X-Y-support. Rotating the substrate over the desired angle after every engraved line generates the wanted pattern. This process takes much time, but certainly can be automated.

The result has shown to be very satisfactory (Fig. H-1: bottom right). The signal level as well as contrast are sufficient to allow further processing (Fig. H-3).

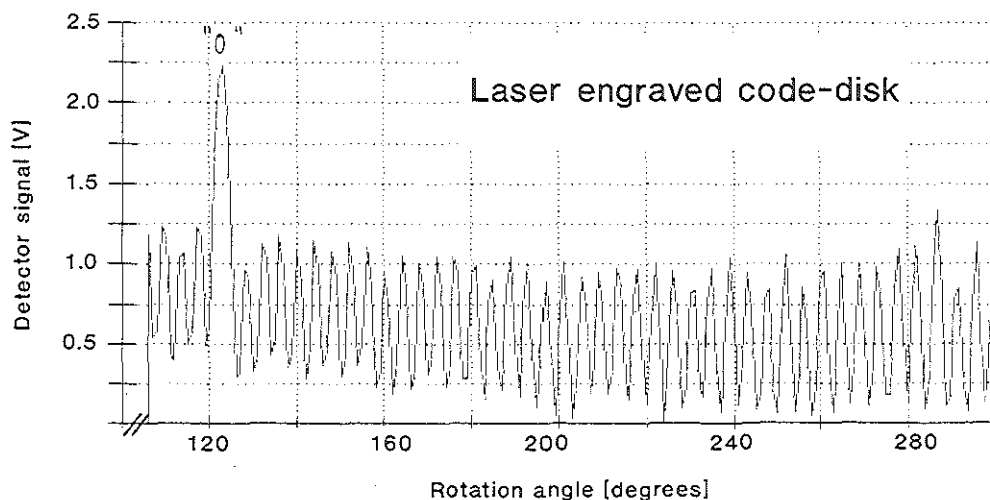


Fig. H-3 Signal response of a nickel on macor code-disk, produced by laser engraving (macor has been polished chemically).

⁽¹⁾A Q-switched Nd-YAg laser has been used with maximum continuous power of 30 W, pulse-length < 40 ns and repetition rate < 4 kHz.

APPENDIX I Calculation of electrical signal transmission lines

The quality of an electrical transmission line in terms of signal loss is determined by the configuration, the materials and dimensions of its conductive and insulating elements. [1] gives all the necessary equations to calculate the signal loss of a variety of transmission lines.

An important consideration is the fact that electrical conductors, especially when they are used for high frequency signal transmission, should have certain minimum dimensions in order to maintain a low electrical resistance.

The "skin effect" describes the tendency of electrical current to travel close to the surface of the conductor, rather than through its inner material. The skin depth δ is the distance below the surface where current density has diminished to 1/e of its value at the surface. For a flat copper conductor it can be found that [1, p. 6-4]:

$$\delta = \sqrt{\frac{R_c}{\pi \mu_c f}} \quad (\text{I-1})$$

where

$R_c = 1.724 \times 10^{-8} \Omega\text{m}$ (resistivity of copper at 20°C)

$\mu_c = 4\pi \times 10^{-7} \text{ Henry/m}$ (permeability of copper)

f = signal frequency in Hz

For $f = 40 \text{ MHz}$, which is the upper limit of the frequency bandwidth of the US-transducer, $\delta = 10 \mu\text{m}$. Nearly all the current is conducted by a layer of several (say at least three) times the skin depth. In our case that is about $30 \mu\text{m}$.

For copper conductors with a round cross-section, either solid or tubular the penetration depth of the currents below the surface of the conductor is given by [1, p. 6-8]:

$$T_1 = \frac{8.89 \times 10^{-2}}{\sqrt{f}} \quad [m] \quad (\text{I-2})$$

where

f is frequency in Hz

For $f = 40 \text{ MHz}$ the penetration depth $T_1 = 14 \mu\text{m}$.

The dc resistance of a copper conductor per unit length can be found by the equation:

$$R_{dc} = \frac{2.195 \times 10^{-8}}{A_{cross}} \quad [\Omega/m] \quad (I-3)$$

where

A_{cross} is the cross-sectional area of the conductor in m^2

It may be clear that in thick conductors not all the material is effectively used for high frequency current transport, so that the ac resistance $R_{ac} \gg R_{dc}$, while for thin conductors with a diameter d in the order of magnitude of the penetration depth $R_{ac} \approx R_{dc}$. Under these conditions R_{ac} changes proportional to $1/d^2$ and is not dependent on the frequency f . If $d \gg T_1$ the cross-sectional area occupied by current transport is about proportional to d/\sqrt{f} , so that R_{ac} is almost proportional to \sqrt{f}/d . The ratio R_{ac}/R_{dc} can be seen as a function of d/\sqrt{f} [1, p. 6-8, Fig. 7]. Consequently $R_{ac}/R_{dc} = 1$ for small d/\sqrt{f} and increases with increasing d/\sqrt{f} to a proportional relation.

The applicability of different configurations of a pair of conductors has been investigated: coaxial, tricoaxial and twisted pair. The important criteria for evaluation of these different alternatives are the outer dimensions and signal loss.

The total signal loss is given by:

$$\text{loss total [dB]} = \text{cable attenuation [dB]} + \text{matching loss [dB]} \quad (I-4)$$

The cable attenuation is given by [1, p. 22-13]:

$$A = \frac{4.34 \times R_t}{Z_0} + 9.12 \times 10^{-8} f F_p \sqrt{\epsilon_r} \quad [\text{dB/m}] \quad (I-5)$$

where

R_t is the two-way ac resistance in Ω/m , to be determined from equation A8-3 and [1, p. 6-8, Fig. 7].

f is frequency in Hz.

F_p is powerfactor of dielectric at frequency f [1, p. 4-28, table 19].

$F_p < 0.0002$ for teflon at frequencies between 10^6 and 10^8 Hz and

$F_p \approx 0.02$ for nylon at frequencies ranging from 60 to 10^8 Hz.

ϵ_r is the relative dielectric constant of the dielectric material.

Z_0 is characteristic impedance in Ω .

The formulas for coax, tricoax and twisted pair are [1, p. 22-21]:

coax and tricoax:

$$Z_0 = \frac{60}{\sqrt{\epsilon_r}} \ln \frac{D}{d} \quad (\text{I-6})$$

twisted pair:

$$Z_0 = \frac{60}{\sqrt{\epsilon_r}} \cosh^{-1} \left(\frac{2D^2}{d^2} - 1 \right) \quad (\text{I-7})$$

where

d and D are dimensions as defined in Fig. I-1.

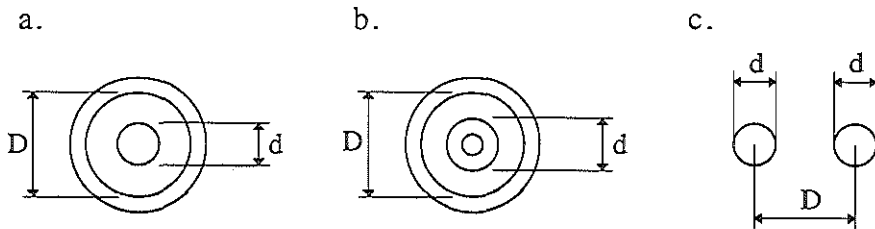


Fig. I-1 Definition of dimensional quantities for a coax (a), tricoax (b) and twisted pair (c).

The matching loss can be found from the equation [1, p. 22-12]:

$$\text{matching loss [dB]} = 10 \log \frac{(S+1)^2}{4S} \quad (\text{I-8})$$

where

S is standing-wave ratio of mismatched impedance referred to Z_0 and is defined as [1, p. 22-7]:

$$S \approx \frac{1 + x^2}{r} \quad (\text{I-9})$$

x and r can be found from the complex impedance:

$$\frac{Z}{Z_0} = r + xj \quad (\text{I-10})$$

where

Z is the complex impedance of the transducer.

Z can be derived from measurements: at 40 MHz the transducer impedance is 18Ω with a phase-angle of -80° .

The complex transducer impedance becomes $Z = 3.13 - 17.76j$.

The optical fiber which should be incorporated in the drive-shaft has a diameter of $135 \mu\text{m}$. As mentioned before, the maximum diameter of the drive-shaft should be less than 0.9 mm to enable free rotation in a 5.2 French catheter. Furthermore the whole shaft assembly should be flexible but also have a high torsional rigidity. This latter function can, if necessary, be fulfilled by a double-wound spiral, with an outer diameter of 0.9 mm and a maximum inner diameter of 0.7 mm. The conductor configurations mentioned above can be combined with these functional and mechanical constraints into the following concepts (Fig. I-2).

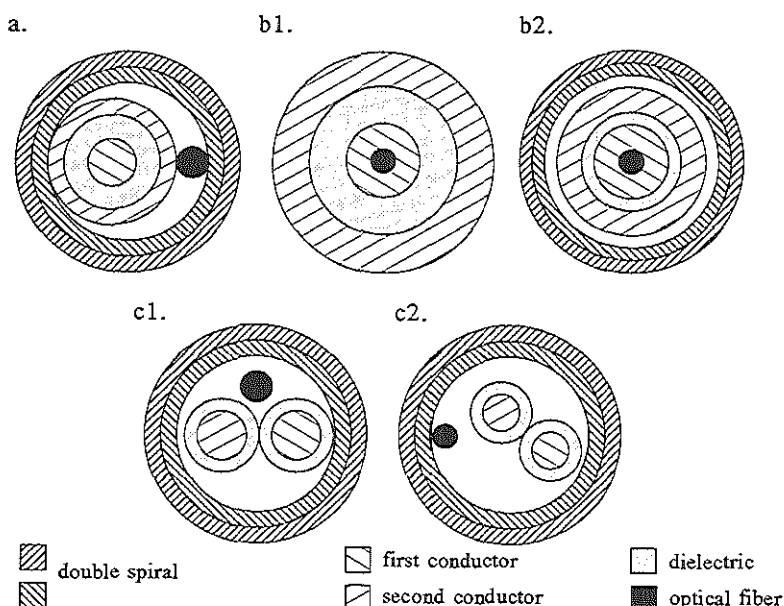


Fig. I-2 Concepts of the drive-shaft assembly containing an optical fiber and two conductors, with a flexible but torsionally rigid structure: coax and fiber in double-wound spiral (a), tricoax (b1), tricoax in double-wound spiral (b2), twisted pair in double-wound spiral with twisted fiber (c1), twisted pair in double-wound spiral with straight fiber (c2).

The maximum dimensions of the conductors in these five cases can be derived.

The total signal loss of these transmission lines has been calculated as a function of the design parameter D/d , for two values of the thickness T of the tubular conductors ($T = 20 \mu\text{m}$ and $T = 50 \mu\text{m}$), and for two values of the relative dielectric constant ϵ_r (for teflon: $\epsilon_r \approx 2$ and for nylon 11: $\epsilon_r \approx 3$). It appears that raising the wall thickness T from $20 \mu\text{m}$ to $50 \mu\text{m}$, the loss increases only with less than 0.1 dB. The same difference can be found while decreasing the size of the tricoax from $900 \mu\text{m}$ OD to $700 \mu\text{m}$ OD and further down to the coax size of $565 \mu\text{m}$ OD. Also decreasing the diameter of the twisted pair from $700 \mu\text{m}$ to $565 \mu\text{m}$ increases the loss with less than 0.1 dB. Using a different dielectric material changes the total signal loss more significantly as can be seen (Fig. I-3). These curves show a clear minimum signal loss at a certain value of the design parameter D/d , which characterizes the optimal design (Table I-1).

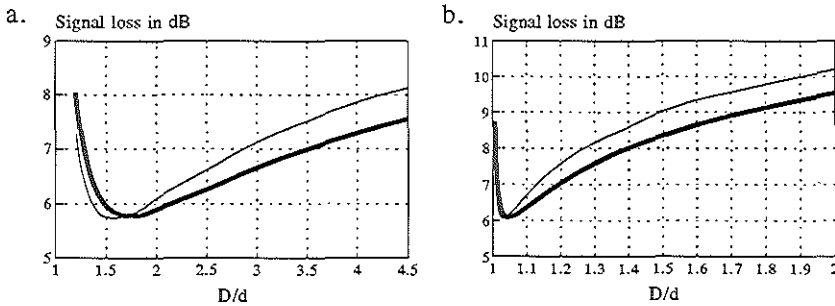


Fig. I-3 Total signal loss as a function of the design parameter D/d for coax and tricoax (a) and twisted pair (b), — $\epsilon_r = 2$, --- $\epsilon_r = 3$ (cable length is 1 m).

The conclusion may be that all three types of transmission lines are suitable for our application, provided that their construction is optimal (the optimal value of D/d is used). The twisted pair seems to be the most critical in this matter. It is not easy to coat a conductor with a 4 or $7 \mu\text{m}$ dielectric layer, but if an increase of 0.5 dB above the minimum signal loss is acceptable, the thickness of the dielectric layer may vary between 3 and $23 \mu\text{m}$, which can be derived from Fig. I-3b.

All the calculated values have been derived from theoretical analysis of copper conductors with a round cross-section, either solid or tubular. They are assumed to be representative also of multi filament helical conductors, that are more suitable for our application because of higher flexibility. The calculated values are intended to be used as a guidance for the design of the drive-shaft assembly. In practice one has to compromise between available wire sizes and different properties of materials.

Table I-1 Minimum total signal loss of transmission lines incorporated in a 0.9 mm OD flexible drive-shaft (conducting material is copper).

Transmission line	OD [μm]	T [μm]	Optimal D/d		Insulation thickness [μm]		Min. tot. signal loss [dB]	
			$\epsilon_r=2$	$\epsilon_r=3$	$\epsilon_r=2$	$\epsilon_r=3$	$\epsilon_r=2$	$\epsilon_r=3$
Coax	565	20	1.6	1.8	100	120	6.0	6.0
		50	1.6	1.8	90	100	6.0	6.1
Tricoax	700	20	1.6	1.8	120	150	5.8	5.9
		50	1.6	1.8	110	130	5.9	5.9
	900	20	1.6	1.8	160	190	5.7	5.8
		50	1.6	1.8	150	180	5.8	5.8
Twisted pair	565	--	1.03	1.05	4	7	6.2	6.3
	700	--	1.03	1.04	5	7	6.1	6.1

Reference

1. Kandoian A.G., DeRosa L.A. e.a. (eds), Reference data for radio engineers, fifth edition, ITT, Howard W. Sams & Co., Inc., Indianapolis-Kansas City-New York, 1970.

Summary

In this thesis, the technological background of intravascular ultrasound (US) imaging is described, with the emphasis on mechanically scanning systems.

Chapter 1

Intravascular US imaging systems have been developed in the past few years, to support the clinical treatment of obstructive vascular disease. Currently many therapeutic intervention methods are developed, mostly based on catheter-technology. The balloon-dilation (Dotter) technique is well-accepted, but also laser-ablation and some mechanical methods, using rotating cutters or drills, are applied clinically, however, on small scale. The classical X-ray angiography does not yield the detailed diagnostic information, needed for these more refined therapeutic methods.

Intravascular ultrasound imaging gives the possibility to obtain an echographic cross-sectional image of a blood-vessel at the location of the catheter-tip. It reveals not only the inner contour of the vessel, but also shows structures under the surface, so that the obstructive atherosclerotic tissue can often be distinguished from original vessel-wall structures. Also some distinction can be made between the different materials, present in a complex morphology of a severe stenosis.

This information can help the physician to choose the most adequate intervention method and also provides a better picture of its results. Furthermore, when integrated with an interventional technique in one catheter, intravascular US imaging can help to guide the catheter-tip and to maintain its position in the center of the lumen in order to avoid vessel-wall perforation.

Chapter 2

Ultrasound can be generated by applying a voltage pulse over a thin slice of piezo-electric material. The effect will be a mechanical vibration of the transducer surfaces with a frequency determined by the fundamental frequency, and a length of the pulse-train, dependent on the damping characteristics of the transducer. The acoustic beam-shape is determined by the frequency and the shape and size of the transducer surface.

An emitted acoustic pulse will partially reflect on tissue boundaries, where a (small) change of acoustic impedance occurs. Small irregularities in the biological tissue, with sizes smaller than the acoustic wave-length, will scatter the sound waves. The reflected or scattered sound waves will partially be received on the same transducer, resulting in the opposite effect: the mechanical vibration is transformed into an electrical signal, which will

be registered. The measured time elapsed since the emission of the acoustic pulse and knowledge about the speed of sound in the present medium, enable the determination of the distance between the reflecting structure and the transducer. Together with the intensity of the echo-signal an image-line can be reconstructed, which coincides with the acoustic axis, perpendicular to the surface of the transducer.

A two-dimensional image can be created by translation or rotation of the transducer, while generating image lines as described before (mechanical scanning).

Another method for two-dimensional imaging is the electronical scanning. Many transducers can be positioned in-line (array) and subgroups can be activated from one side of the array to the other. If the elements of an array are activated with a controlled relative phase-shift the resulting ultrasonic beam can be focused and swept over a certain sector (phased array).

For the intravascular application both methods can be used to make a two-dimensional echo-scan of the surrounding of a catheter-tip. A circular array of ultrasonic elements can be applied to the outer surface of the catheter for generation of an electronical scan. Also one transducer positioned near the center of the catheter, with its acoustic axis perpendicular to the center-line of the catheter, can be rotated, in order to generate a mechanical scan. If the acoustic axis of the element is chosen in-line with the center-line of the catheter, a reflecting mirror under 45° with the acoustic axis will deflect the beam to a perpendicular direction. In this case the mirror can be rotated. Furthermore it is possible to combine the transducer with a mirror into one module which can be driven as a unit.

Considering the currently available piezo-electric materials, it should be assumed that for small catheter diameters (< 1.5 mm), the potential image quality of the mechanically scanning system is superior. Furthermore, because of hygienic reasons the catheters should be for one-time-use only, so the price of a catheter becomes an important issue. Also in this matter the mechanically scanning system offers better perspectives. Consequently this system is chosen for further development.

The choice of the acoustic frequency is given by a compromise between image resolution and penetration depth. At high frequencies the resolution increases, but the absorption in biological tissue will increase too. For the application of intravascular US imaging, especially the coronary arteries and the femoral arteries are good candidates. A depth of view of 10 mm is sufficient in these cases. At an acoustic frequency of 30 MHz this penetration depth can be reached and also an acceptable image resolution of a few tenths of a millimetre can be achieved.

In echography the imaged objects are often moving. This is also the case in intravascular echography. The coronary arteries move together with the heart-muscle and other arteries pulsate in accordance with the heart-rate. In order to avoid motion artifacts in the images and to enable dynamic analyses, preference is given to "real-time" imaging techniques. For intravascular ultrasound imaging a practical frame-rate of 16 images per second can be chosen, which means a catheter-tip rotation speed of 1000 rpm.

Chapter 3

The most important problem to solve in the development of a mechanically scanning ultrasound imaging catheter is finding an adequate driving mechanism for either the transducer, the mirror, or the combination module.

The ultrasonic image is at first built-up in a polar fashion; every radial image-line corresponds to one ultrasonic emission pulse and the angular position of the image-lines on the screen should coincide with the actual rotation angle of the ultrasonic beam in the catheter-tip. This is difficult to accomplish. If no angle-detection system is built into the catheter-tip, the rotational behaviour of the ultrasonic beam should be well predictable. The most obvious choice is to strive for uniform catheter-tip rotation. Deviations from uniform rotation, which cannot be taken into account while producing the ultrasonic image on the screen, may result in wrong interpretation of images. The image artifacts depend on the behaviour of the tip-rotation error angle (= actual tip-rotation angle minus expected angle).

A constant rotation error angle influences the orientation of the whole image on the screen, but does not cause any image distortion. The reference to the patients anatomy may be lost this way. A stochastic error causes two succeeding frames not to coincide, so that the real-time aspect becomes restless or even blurred to the eye. Deceptive in terms of misinterpretation of the images is the occurrence of a periodic error angle, with the same frequency as the driving rotation or one of its higher harmonics. The image on the screen is nicely stationary, but sectors of the image are expanded or compressed. This can influence the results of quantitative analysis. The rate of stenosis of a vessel can be over- or under-estimated by tens of percents. From simulation it appears that this type of image distortion is acceptably small, if the peak-to-peak value of the periodic error angle is smaller than 20°.

Several micro-mechanical methods to rotate the ultrasonic beam have been investigated. The most important criterion in the evaluation is the feasibility of a predictable tip-rotation. Two methods have been chosen.

As a more pragmatic approach the application of a flexible drive-shaft has been investigated, based on the principle of (at least) two counter-wound layers of helical filaments, with maximum interference (no clearance between them). This shaft runs through the whole catheter-tube and transmits the rotation from a proximal driving motor, outside the patient's body, via the tortuous catheter-tube, to the distal tip. The finite torsional rigidity of such a long thin shaft causes a deviation from a one-to-one transmission. The torsional rigidity of the described shaft, however, is relatively high with respect to its low bending rigidity, which is necessary to maintain the flexibility of the catheter as a whole. We succeeded in producing these drive-shafts with the desired small diameter (about 0.8 mm) and angular fidelity of the rotation transmission.

As a future alternative we started the development of an electro-magnetic micro-motor. This resulted already in well-functioning prototypes, with a diameter of 1 mm and a length of approximately 2 mm. The motor can drive an acoustic mirror in the catheter-tip. Also in this development it appeared that the required uniform rotation makes high demands upon the construction of the motor.

Chapter 4

Apart from a pragmatic approach to solve the development problems of the flexible drive-shaft, a theoretical study to analyse the rotation transmission, using this shaft, has been conducted.

Analytical models, based on classical mechanics, describe the effects of influences, which disturb the uniformity of the rotation transmission. The three most important influences are: pre-curvature (a drive-shaft, free of load, is not completely straight), unequal bending rigidity in different planes and friction. The first two cause the misleading periodic error angle, with a repetition frequency of respectively one time and two times the rotation frequency. Friction mainly causes a constant rotation error angle (drag). For all three influences it is shown that the resulting error angle decreases with decreasing ratio bending rigidity/torsional rigidity, so this should be an important design parameter in the construction of flexible drive-shafts for this application.

The analytical modelling, which only describes simple catheter geometries, is tested against numerical calculations, based on the finite element method. The results show a high degree of similarity.

Furthermore experimental results have been obtained, using a dedicated test set-up in which the tip-rotation angle can be monitored contactless with respect to the driving rotation. For drive-shafts with purely linear elastic deformation behaviour the experimental results also confirm the analytical modelling.

Chapter 5

Under certain conditions, the angular fidelity of a flexible drive-shaft rotation transmission may not be sufficient. This may be the case for extreme curvatures, further miniaturization or integration with an interventional technique. If the required power for the intervention method should (partially) be delivered by the same rotating drive-shaft, which may be the case for a "drilling" action, this mechanical load will cause torsion of the shaft and will interfere with the uniform rotation transmission to the US-transducer.

The tip-rotation angle can be monitored continuously, so that image-lines can be generated and displayed at constant angle increments.

It should be mentioned that the research on an angle detection system had started before the development of the double-layer spiral drive-shaft technology and the theoretical modelling of its behaviour. It was assumed that a well functioning angle detection system would alleviate the high demands, made upon the uniformity of the tip-rotation.

An optical angle detection system has been developed, involving an optical fiber, incorporated in the flexible drive-shaft, which communicates with a stationary code-disk in the tip of the catheter, with 78 radial reflecting code-lines. At these small catheter-tip dimensions the width of a code-line is only 15 μm . It appeared to be difficult to produce a code-disk, with a diameter of 1.2 mm, having appropriate reflection characteristics and a well-defined undamaged code-pattern. The best option found was a nickel layer, sputtered onto a macor[®] (glass-ceramic) substrate. The code-pattern was applied by laser-engraving.

It was assumed that a high angular resolution, implying a large number of thin code-lines, would require the application of a single-mode optical fiber, with a small core diameter (about 7 μm). However, this appeared to be based on a misconception. It needlessly aggravated the demands made upon construction tolerances. A multimode optical fiber, with a core diameter of 50-100 μm , illuminates a large number of reflecting lines. Nevertheless the signal shows sufficient modulation, because only reflections from code-lines very near to the optical axis manage to be recaptured by the fiber and consequently be detected.

None of the prototypes, based on the application of single-mode fiber technology was fully functional. However, by evaluation of subsystems, especially applying a multimode fiber, the feasibility of this optical angle detection technology has been demonstrated.

Samenvatting

Dit proefschrift beschrijft de technologische achtergronden van m.n. mechanisch scannende intravasculaire echo-imaging systemen (IVUS = intravascular ultrasound).

Hoofdstuk 1

IVUS-systemen zijn in de afgelopen jaren ontwikkeld, ter ondersteuning van de bestrijding van atherosclerotisch vaatlijden. Meerdere methoden, gebaseerd op catheter-technologie, zijn en worden ontwikkeld om vaatvernauwingen op te heffen. Bekend is de ballon-dilatatie (Dotter), maar ook laser-ablatie en enige mechanische methoden met draaiende mesjes, boortjes en freesjes worden reeds op kleine schaal klinisch toegepast. De klassieke Röntgen-angiografie bleek niet de gedetailleerde diagnostische informatie te kunnen bieden, die voor deze meer verfijnde therapeutische methoden nodig is.

Intravasculaire echo-imaging biedt de mogelijkheid om ter plaatste van de catheter-tip in een bloedvat een echografische doorsnede van dat vat zichtbaar te maken. Het toont niet alleen de binnen-contour van het vat, maar ook dieper gelegen structuren, zodat vaak het atherosclerotische vernauwende weefsel te onderscheiden is van de oorspronkelijke vaatwand-structuren. Zelfs kan enig onderscheid gemaakt worden tussen de aanwezige materialen, die deel uitmaken van de veelal complexe morfologie van een ernstige stenose.

Deze informatie kan de medicus helpen bij het kiezen van de juiste interventie-methode en geeft ook een beter beeld van het resultaat ervan. Ook kan intravasculaire echo-imaging, wanneer het in één catheter met een desobstructie-techniek geïntegreerd is, de positie van de catheter-tip in het centrum van het bloedvat waarborgen, zodat perforatie van de vaatwand wordt vermeden.

Hoofdstuk 2

Ultrageluid wordt opgewekt door een spanningspuls aan te bieden over een dun plakje piëzo-materiaal, waardoor dit in trilling wordt gebracht. De frequentie en lengte van de akoestische pulstrein zijn afhankelijk van respectievelijk de eigenfrequentie en de dempingskarakteristiek van de transducent. De akoestische bundelvorm wordt bepaald door de frequentie en de vorm en afmetingen van het transducent-oppervlak.

Een uitgezonden akoestische pulstrein zal gedeeltelijk reflecteren tegen weefsel-overgangen, waar een (kleine) akoestische impedantie-sprong bestaat. Ook kunnen onregelmatigheden in het weefsel, met afmetingen kleiner dan de golflengte, het geluid omnidirectioneel verstrooien. Het teruggeworpen geluid wordt door de inmiddels uitgedempte transducent opgevangen en resulteert in een omgekeerd effect: de trilling

wordt omgezet in een elektrisch signaal, dat wordt geregistreerd. De verstreken tijd sinds het genereren van de zendpuls en kennis van de geluidssnelheid in het onderhavige medium, maken het mogelijk de afstand van de reflecterende structuur tot de transducent te bepalen. Samen met de intensiteit van de echo kan nu één beeldlijn worden gemaakt, samenvallend met de as van de transducent, loodrecht op het transducent-oppervlak.

Een twee-dimensionaal beeld kan worden opgebouwd door de transducent te transleren of te roteren, terwijl op bovenstaande wijze beeldlijnen worden gegenereerd (mechanische scan). Ook kunnen vele transducenten op een rij worden geplaatst (linear array), die in groepjes van de ene kant naar de andere kant van het array worden aangestuurd (elektronische scan). Als de elementen, geplaatst op één lijn met een bepaald onderling faseverschil worden aangestuurd, kan de resulterende bundel worden gefocusseerd en van richting worden veranderd. Met een dergelijk array kan dus een sector-scan gemaakt worden (linear phased array).

Voor de intravasculaire toepassing bestaan ook deze mogelijkheden om een twee-dimensionale echo-scan van de omgeving van een catheter-tip te maken. Het buitenoppervlak van de catheter, met ronde doorsnede, kan worden belegd met een circulair array van piëzo-elementjes, voor het maken van een elektronische scan. Ook kan een enkele transducent, geplaatst dichtbij het hart van de catheter, met de akoestische as (ongeveer) loodrecht op de catheter-as, worden geroteerd (mechanische scan). Als de akoestische as in-lijn met de catheter-as wordt geplaatst, kan een akoestisch spiegeltje onder 45° , dat de geluidsbundel loodrecht op de catheter-as afbuigt, worden aangedreven. Verder is het mogelijk in deze configuratie transducent en spiegeltje in één module op te nemen en samen te roteren.

Met de huidige beschikbare piëzo-actieve materialen moet worden aangenomen dat voor catheters met een kleine diameter ($< 1,5$ mm), de potentiële beeldkwaliteit voor het mechanisch scannende systeem hoger ligt.

Om hygiënische redenen heeft het de voorkeur de catheters slechts éénmalig te gebruiken, zodat de prijs zo laag mogelijk moet blijven. Ook hier biedt de mechanisch scannende catheter betere perspectieven. Dit systeem wordt dus gekozen.

De keuze van de akoestische frequentie volgt uit een compromis tussen resolutie en indringdiepte. Bij hogere frequentie neemt de resolutie toe, maar de verzwakking in biologisch weefsel neemt ook toe. Voor de toepassing van intravasculaire echo-imaging wordt vooral gedacht aan de kransslagaders en beenvaten. Een afbeeldingsdiepte van 10 mm is dan voldoende. Bij een akoestische frequentie van 30 MHz is dit mogelijk en wordt ook een acceptabele resolutie van enige tienden van millimeters bereikt.

In de echografie maakt men vaak opnamen van bewegende structuren. Dit zal ook het geval zijn bij intravasculaire echo. De kransslagaders bewegen met het hart mee en andere slagaders pulseren met de hartfrequentie. Om bewegingsartefacten te voorkomen en t.b.v. dynamische analyses, wordt vaak de voorkeur gegeven aan "real-time" afbeeldingstechnieken. Praktisch kan bij intravasculaire echografie een beeldherhalingsfrequentie gekozen worden van 16 beelden per seconde, hetgeen overeenkomt met een catheter-tip rotatie van 1000 omwentelingen per minuut.

Behalve kennis van akoestiek, beeld-genererende en -verwerkende technieken moeten ook catheter-technologie en micro-mechanica worden toegepast. Voor de catheter-technologie is het raadzaam zoveel mogelijk aan te sluiten bij de bestaande kennis en praktijk, aangaande bloed-compatibele materialen, veiligheidsvoorschriften, schoonmaak- en sterilisatie-procedures en klinische toepassingsmethoden.

Hoofdstuk 3

Het grootste probleem van het ontwikkelen van een mechanisch scannende echo-imaging catheter is het vinden van een adequate aandrijftechniek voor òf de transducent, òf het spiegeltje, òf een combinatie-module.

Het echo-beeld wordt in eerste instantie polair opgebouwd: elke radiale beeldlijn correspondeert met één zendpuls en de hoekpositie van de beeldlijnen moet overeenkomen met de rotatie-hoek van de ultrageluidsbundel in de catheter-tip. Dit laatste is niet eenvoudig. Als geen hoek-detectie in de catheter-tip wordt ingebouwd, moet het rotatie-gedrag van de geluidsbundel zo voorspelbaar mogelijk zijn. De meest voor de hand liggende keuze is het nastreven van een eenparige rotatie. Afwijking hiervan, waarmee bij de beeldopbouw dus geen rekening gehouden kan worden, kan leiden tot slecht interpreteerbare beelden. De beeldfouten zijn afhankelijk van het gedrag van de hoekfout (= werkelijke tip-rotatiehoek minus verwachte hoek).

Een constante hoekfout beïnvloedt de oriëntatie van het gehele beeld, maar veroorzaakt geen vervorming. De referentie tot de anatomie van de patiënt kan hierdoor verloren gaan. Een stochastische fout veroorzaakt het niet samenvallen van twee opeenvolgende beelden, zodat de real-time afbeelding onrustig en onscherp wordt. Misleidend t.a.v. de interpretatie van de beelden is het optreden van een periodieke hoekfout met dezelfde periodiciteit als de aandrijffrequentie, of één van zijn hogere harmonischen. Het beeld staat mooi stil maar beeldsectoren zijn geëxpandeerd of gecomprimeerd t.o.v. een waarheidsgetrouwe afbeelding. Dit kan ook de resultaten van kwantitatieve analyses beïnvloeden. De mate van vernauwing van een vat kan met tientallen procenten worden over- of onderschat. Uit simulatie blijkt dat deze beeldvervorming acceptabel blijft als de top-top-waarde van de periodieke fout kleiner is dan ca. 20°.

Verschillende micro-mechanische mogelijkheden om de geluidsbundel te roteren in de tip van een catheter zijn beschouwd, met als voornaamste criterium de haalbaarheid van een voorspelbare rotatie. Twee methoden zijn gekozen.

Voor de kortere termijn is de voor de hand liggende toepassing van een flexibele aandrijf-as uitgewerkt, gebaseerd op het principe waarbij (minstens) twee tegengesteld gewikkelde spiraallagen spelingsloos (of liever met enige voorspanning) op elkaar liggen. Deze as loopt door de hele catheter-buis en verzorgt de overbrenging van de rotatie van een motor, buiten het lichaam van de patiënt, via de bochtige catheter-buis, naar de tip. De eindige torsiestijfheid van zo'n lange dunne as veroorzaakt een afwijking van een één-op-één overbrenging. De torsiestijfheid van de beschreven as is echter relatief hoog t.o.v. een lage buigstijfheid, die nodig is om de flexibiliteit van de catheter als geheel te waarborgen. Het is gelukt dergelijke assen te vervaardigen, met de gewenste kleine diameter (ca. 0.8 mm) en hoekgetrouwheid van de rotatie-overbrenging.

Als toekomstig alternatief is de ontwikkeling van een elektro-magnetische micro-motor gestart en heeft geresulteerd in werkende prototypes met een diameter van 1 mm en een lengte van ruim 2 mm. Hiermee kan een akoestisch spiegeltje in de catheter-tip worden aangedreven. Ook bij deze ontwikkeling bleek de eis van eenparige rotatie hoge eisen te stellen aan de motorconstructie.

Hoofdstuk 4

Behalve een pragmatische aanpak om ontwikkelingsproblemen van de flexibele aandrijf-as op te lossen, is ook een theoretische studie verricht om de rotatie-overbrenging m.b.v. een flexibele as te analyseren. Analytische modellen, beschrijven het effect van factoren die de eenparigheid van de rotatie-overbrenging verstoren. De drie belangrijkste oorzaken zijn: voorkromming (een as is in onbelaste toestand niet zuiver recht), verschil in buigstijfheid in beide hoofdrichtingen en wrijving. De eerste twee veroorzaken de gevreesde periodieke hoekfout met een herhalingsfrequentie die respectievelijk 1 x en 2 x de rotatie-frequentie is. Wrijving veroorzaakt voornamelijk een constante hoekfout.

Voor alle drie factoren geldt dat de resulterende hoekfout afneemt bij afnemende verhouding buigstijfheid/torsiestijfheid, zodat dit een belangrijke parameter moet zijn bij het ontwerp en de constructie van flexibele assen voor deze toepassing.

De analytische modellering, die overigens alleen eenvoudige catheter-geometrieën kan beschrijven, is getoetst aan numerieke berekeningen, uitgevoerd met een eindige elementen model. De resultaten komen goed overeen. Dit bevestigt de waarde van het analytische model, maar verhoogt ook het vertrouwen in het eindige elementen model, dat complexere geometrieën en combinaties van invloeden kan simuleren. Dit laatste is echter niet uitgevoerd.

Ook praktische meetresultaten zijn verkregen met een speciaal ontwikkelde meetopstelling, waarin de tip-rotatie van de as contactloos wordt gevolgd en gerelateerd aan de aandrijf-rotatie. Voor zuiver lineair elastisch vervormende assen bleken ook de meetresultaten de analytische modellering te ondersteunen.

Hoofdstuk 5

Onder bepaalde omstandigheden zal een flexibele as-aandrijving niet voldoende hoekgetrouw kunnen zijn. Dit kan het geval zijn bij gebruik onder extreem gebogen omstandigheden, verdere miniaturisatie of integratie met een desobstructie-techniek, waarbij (een gedeelte van) het benodigde vermogen voor rekanalisatie door de draaiende as geleverd moet worden. De as verzorgt in dit laatste geval zowel de echo-scan beweging als de overdracht van rotatievermogen naar de b.v. borende catheter-tip. Deze mechanische belasting aan de tip van de as zal torsie veroorzaken.

De rotatie-hoek van de tip kan continu worden gemeten, zodat beeldlijnen met constant hoekincrement kunnen worden gegenereerd en afgebeeld.

Het moet worden opgemerkt dat de ontwikkeling van een hoekdetectie-systeem gestart is, voordat de dubbele spiraal-as-techniek en -theorie waren ontwikkeld, met de gedachte dat een goede hoekdetectie de eisen, te stellen aan de eenparigheid van de tip-rotatie, aanzienlijk zou verlichten.

Een optische hoekdetectie is ontwikkeld, waarbij een glasfiber in een flexibele as wordt opgenomen en deze communiceert met een stilstaande codeschijf in de tip met 78 radiale reflectieve spaken. Bij deze kleine catheter-tip afmetingen zijn de spaken 15 μm breed. Het kostte grote moeite een codeschijfje, met een diameter van 1,2 mm te vervaardigen, met de juiste reflectieve eigenschappen en een onbeschadigd spaken-patroon. Laser-graveren in een reflectieve nikkellaag, gesputterd op een macor substraat, bleek het beste te voldoen.

De gedachte dat voor een hoge hoekresolutie en dus een kleine spaakbreedte een "single-mode" glasfiber met een lichtgeleidende kern van ca. 7 μm zou moeten worden gebruikt, bleek onjuist en heeft de eisen aan de toleranties van de tip-constructie onnodig verzwaard. Een "multi-mode" fiber, met een kern van 50-100 μm , verlicht vele spaken tegelijk. Toch laat het reflectie-sigitaal, bij relatieve beweging van de fiber t.o.v. de spaken, voldoende modulatie-diepte zien, omdat alleen de reflecties van enige spaken dichtbij de optische as door de fiber kunnen worden ingevangen om te worden gedetecteerd.

Geen van de gebouwde catheter-prototypen, gebaseerd op toepassing van een single-mode glasfiber is volledig functioneel gebleken. Toch kon m.b.v. metingen aan subsystemen, en met name bij toepassing van de multimode fiber, de technologische haalbaarheid van een dergelijk systeem worden aangetoond.

Acknowledgements

Because of the extent of this project it is impossible to acknowledge all the work performed by institutions, companies and individuals, which has made this venture a success. Although grateful for all the other contributions, that will remain unmentioned, I want to express my special gratitude to:

Klaas Bom, under who's guidance my first years of working at the Thoraxcentre turned into an exciting job, full of challenge and opportunities. During the often lonely occupation of working on this thesis his encouragements have been a great help. Therefore I am very proud that he is now acting as my promotor.

My colleagues of Experimental Echocardiography:

Charles Lancée, for the pleasant way we worked together, complementing each other in managing this project and the patience in explaining to me all I ever needed to know about acoustics (and more). Furthermore, I am especially grateful for his constructive comments on some chapters of this thesis.

Pieter Brommersma, who meanwhile has left our group, for the stimulating discussions on mechanical issues and certainly for the joy of hiking together in the Ardennes.

Frits Mastik, for his essential knowledge and skill on computer applications, especially when the simple user is (constantly) in trouble with his machine.

Elma Gussenhoven, for her comments on and contributions to Chapter 1.

Nico de Jong, Hans Rijsterborgh, Jan Honkoop, Frans van Egmond, Li Wenguang and Kie Djoa, for their good-fellowship in contributing their skills to the solution of what ever problem arises.

Corrie Eefting and Yvonne van den Steen, for their secretarial work and organizing efforts, but also for the ever lasting friendly answers to the numerous interrupting questions and requests I came forward with, during my work on this thesis.

Delft University of Technology, The Netherlands:

Prof. dr. ir. P. Meijers, prof. dr. ir. J.F. Besseling en dr. ir. J.P. Meijaard of the Laboratory for Engineering Mechanics, Faculty of Mechanical Engineering and Marine Technology. Their willingness to help me gain understanding of the behaviour of a flexible drive-shaft in a curved tube (Chapter 4), was most obliging. In fact, Jaap Meijaard specially composed a finite element model, dedicated to my problem (Appendix E), with which I could simulate the flex-shaft behaviour (§ 4.2). Also for the adequate formulation of the analytical models (Appendices B, C and D) their support was indispensable.

Prof. dr. ir. H.F. van Beek and his staff of the Laboratory for Precision Engineering, Faculty of Mechanical Engineering and Marine Technology, for their contribution to the search for alternative catheter-tip driving mechanisms (Chapter 3) and the valuable suggestions for improvement of the final version of this thesis.

Gerard Faber and Gerrit van Dijk of the Laboratory of Acoustic Transducers, Group of Acoustics and Seismics of the Faculty of Applied Physics, for all their effort put into the development of the ultrasonic transducers with mostly extreme specifications, demanded by our application. But I am also most grateful for their willingness to investigate and advise on every issue related to their competence, and their persisting attitude in finding solutions.

Institutions and industries:

Du-MED B.V., Rotterdam, The Netherlands:

For our fruitful co-operation, based on mutual interest, but exceeding all that, a warmhearted supportive attitude towards my work for this Ph.D. thesis.

Productcentre TNO, Delft, The Netherlands:

For the close and harmonious co-operation in the development of the angle detection system (§ 5.3), where the Productcentre contributed to the design and did all the prototyping.

TNO-TPD, Delft, The Netherlands:

For contributing their knowledge on fiber optics, as was used in the angle detection system (§ 5.3).

Coenecoop B.V., Waddinxveen, The Netherlands:

Especially to Mar van der Hoek, for contributing his rich and practical knowledge on (fiber) optics to the prototyping of catheters with an angle detection system (§ 5.3), in close co-operation with the Productcentre TNO. He also helped to develop the measurement set-up for monitoring flex-shaft rotation transmission characteristics (§ 4.3), which is also meant for characterization of the electro-magnetic micro-motors (§ 3.2.2). Furthermore, I am very grateful for his willingness to review Chapter 5 of this thesis and for all the suggestions to improve it.

USCI, Billerica, MA, USA:

Especially to Lex Jansen, for the more than friendly welcome I received, when going to the US several times to investigate production methods for double-layer helically wound flexible drive-shafts. Only because of his time, effort and ideas and the support of the whole company, these few visits of two or three weeks have been so successful. Also thanks to Lex and Mary-Kay, and Ken Levin and his wife, I could avoid hotel-rooms as much as possible, so that apart from the fruitful work I cherish delightful memories of these visits.

Students:

Arie Korbijn, for his work within the framework of his MSc. thesis, investigating alternative driving mechanisms for catheter-tip rotation. Part of § 3.2 is based on his work.

Tom Mossop, who assisted me with the last experiments (§ 4.3 and Appendix F) in studying the flex-shaft behaviour in a curved catheter-tube, which showed a high degree of similarity to the results of the analytical as well as the numerical models.

Koen Michels, for his work within the framework of his MSc. thesis, investigating polymer materials on their suitability for application as an acoustic window and studying the system specifications related to clinical use, such as cleaning and sterilization methods for the catheters and ergonomic aspects of the bed-side application.

Theo Smit, for his pioneerswork on dynamic measurements of flexible drive-shaft rotation transmission characteristics (§ 4.3) and the development of a functional model of an ultrasonic probe for urological use, as a final task for his MSc. degree. The latter is not described in this thesis; it was a separate spin-off activity.

Acknowledgements

René Jansen, John Maasdam (BSc. thesis), Erik Geluk (BSc. thesis), for their work in the field of catheter technology, micro-valves and bonding techniques, especially with respect to the patient safety of the catheter.

And I am extremely indebted to my Dinah, for all the work she did with me (mainly on Sundays) to finish this thesis, but I am even more grateful for all the evenings she had to spend without me. Instead of complaints I got diner served with a smile at the strangest hours. If nothing else, I shall certainly miss that.

Curriculum Vitae

Harm ten Hoff werd geboren op 28 november 1958 te Borger. Hij volgde het lager onderwijs in Borger en bezocht daarna tussen 1971 en 1977 de Gemeentelijke Scholengemeenschap te Emmen. Met het hier behaalde Atheneum-B diploma werd hij in 1977 toegelaten tot de Universiteit Twente (toen Technische Hogeschool Twente) in Enschede, waar hij Werktuigbouwkunde studeerde. Hij studeerde in 1985 af bij de vakgroep Fijnmechanische Techniek (afstudeerdocent Prof. dr. ir. L.H.J.F. Beckmann), op de ontwikkeling van een stuurbare elektrode-catheter voor endocardiale cathetermapping. Zijn voorkeur om de vergaarde technologische kennis toe te gaan passen in het medische veld, bracht hem ertoe post-doctoraal nog een aantal medische en medisch- technologische vakken te volgen aan de Universiteit Twente. Dit combineerde hij tot begin 1986 met een part-time aanstelling als wetenschappelijk medewerker bij het Coördinatiecentrum Bio-Medische Technologie (CCBMT). Hier ontwikkelde hij een twee-straal laser-Doppler anemometer, voor hemo-rheologische research in het kader van het onderzoek naar ontstaanshypothese van atherosclerose. Dit werk werd daarna tot eind 1987 voortgezet als full-time medewerker bij het Academisch Ziekenhuis Utrecht, zij het gedetacheerd in Twente.

Begin 1988 kwam hij naar de Erasmus Universiteit Rotterdam, waar hij bij de afdeling Experimentele Echocardiografie, onder leiding van Prof. dr. ir. N. Bom, een centrale functie bekleedde in het ambitieuze en inmiddels succesvolle project van de ontwikkeling van een intravasculair echo-imaging systeem. Met name de catheter-technologie en mechanica behoorden tot zijn inbreng. In de eerste jaren bestonden zijn werkzaamheden grotendeels uit project-management. Toen begin 1991 vele activiteiten rond de ontwikkeling door het startende bedrijf Du-MED B.V. werden overgenomen, besloot hij het werk als promotie-onderzoek voort te zetten.

Publications of the author

N. Bom, H. ten Hoff, C.T. Lancée, W.J. Gussenhoven, J.G. Bosch, Early and recent intraluminal ultrasound devices, *Int. J. Cardiac Imag.* 4: 79-88, 1989.

J.R.T.C. Roelandt, P.W. Serruys, N. Bom, W.G. Gussenhoven, C.T. Lancée, H. ten Hoff, Intravascular real-time, two-dimensional echocardiography, *Int. J. Cardiac Imag.* 4: 63-67, 1989.

N. Bom, H. ten Hoff, C.T. Lancée, W.J. Gussenhoven, Intra-arterial ultrasonic imaging, *Ultrasound Bulletin*, 1989.

H. ten Hoff, A. Korbijn, Th.H. Smit, J.F.F. Klinkhamer, N. Bom, Imaging artifacts in mechanically driven ultrasound catheters, *Int. J. Cardiac Imag.* 4: 195-199, 1989.

N. Bom, H. ten Hoff, C.T. Lancée, W.J. Gussenhoven, P.W. Serruys, C.J. Slager, J. Roelandt, Early and present examples of intraluminal ultrasonic echography, *Proceedings of the conference on Catheter-based Sensing and Imaging Technology, SPIE 1068*: 146-150, 1989.

J. Roelandt, P.W. Serruys, W.J. Gussenhoven, C.T. Lancée, N. Bom, H. ten Hoff, Intraluminal ultrasound: Clinical perspectives. *Thoraxcentre J.* 1: 20-30, 1989.

M.J. van der Hoek, D. de Bruijn, Th.J.M. Jongeling, C.T. Lancée, H. ten Hoff, Ontwikkeling van een optische hoekencoder voor een roterend ultrasoon transducent, opgenomen in een catheterkop, *Nederlands Tijdschrift voor Fotonica* 16 No. 4: 19-27, 1990.

M.G.M. de Kroon, H. ten Hoff, W.J. Gussenhoven, N. Bom, Intravasculaire ultrasone afbeeldingstechniek, *Nederlands Akoestisch Genootschap, Journaal* No. 105: 35-42, 1990.

N. Bom, H. ten Hoff, W.J. Gussenhoven, J.H.C. Reiber, M.G.M. de Kroon, C.T. Lancée, J. Roelandt, Quantification of arterial obstructions with intra-arterial echography: Technical problems, *Proceedings 7th Congress on Echocardiography, Rome (Italy)*, A. Dagianti, H. Feigenbaum (eds.), 1990.

H. ten Hoff, N. Bom, Reduction of image distortion in mechanically scanned intravascular echography: high fidelity drive-shaft design and miniature angle detection system, *Proceedings of the 4th International Symposium on Biomedical Engineering, Peñíscola (Spain)*, 1991.

N. Bom, W.J. Gussenhoven, C.T. Lancée, C.J. Slager, P.W. Serruys, H. ten Hoff, J.R.T.C. Roelandt, Intra-arterial ultrasonic imaging, In: *Ultrasound in Coronary Artery Disease*, S. Illiceto et al. (eds.), Kluwer Academic Publishers, The Netherlands, pp. 277-284, 1991.

N. Bom, C.T. Lancée, E.J. Gussenhoven, W. Li, H. ten Hoff, Basic principles of intravascular ultrasound imaging, In: *Intravascular Ultrasound Imaging*, J.M. Tobis, P.G. Yock (eds), Churchill Livingstone Inc., New York, pp. 7-15, 1992.

N. Bom, C.T. Lancée, H. Rijsterborgh, H. ten Hoff, J.R.T.C. Roelandt, From idea to clinical application, In: *Intravascular Ultrasound 1993*, J.R.T.C. Roelandt, N. Bom, E.J. Gussenhoven, eds., Kluwer Academic Publishers, Dordrecht, 1993, (in press).

